Engineering influenza HA nanoparticles to better understand their immune responses and improve vaccine design

Anne Dosey

A dissertation

submitted in partial fulfillment of the

Requirements for the degree of

Doctor of Philosophy

University of Washington

2023

Reading Committee:

Neil P. King, Chair

Kelly K. Lee

Jesse Bloom

Program Authorized to Offer Degree:

Biochemistry

University of Washington

Abstract

Engineering influenza HA nanoparticles to better understand their immune responses and improve vaccine design

Annie Dosey

Chair of the Supervisory Committee:

Neil P. King

Department of Biochemistry

Protein nanoparticle-based vaccines are a promising platform, shown to be efficacious in preventing disease against a variety of pathogens. Building on their success, increasing our understanding of how nanoparticle vaccines elicit immune responses will aid both in our general understanding of immunology and also in designing improved vaccines. This work centers on influenza hemagglutinin (HA) nanoparticle vaccine design. It starts with the design of HA ‘trihead’ nanoparticle vaccines, that incorporate several layers of immune refocusing to increase breadth and potency in responses elicited against the HA head. Trihead design was then adapted onto several strains of HA, with the ultimate goal of creating a new platform for seasonal influenza vaccines. Lastly, the interaction of antibodies and HA ectodomain nanoparticles was explored as a means to elucidate mechanisms of their immunogenicity.

Table of Contents

List of Figures and Tables

Acknowledgements

I want to thank Neil P. King for taking me into his lab, for teaching me so much about protein interactions and staring at pymol sessions, for fostering rigor in my science and for navigating successful collaborations, for always brainstorming with me and being endlessly excited about the work going on his lab, for getting through pandemic times together under the lunch tree and sharing so many life-lesson anecdotes, and for having his door open.

I want to thank my committee, Kelly K. Lee, Jesse Bloom, David Veesler, and Frank DiMaio, who have all been collaborators and mentors to me throughout this work. I want to thank Masaru Kanekiyo for all of his wisdom and guidance and for being an outstanding collaborator. I want to thank the following people who contributed to this work: Seyhan Boyoglu-Barnum and Hubza Syeda performed all neutralization assays, John C. Kraft, Minh N. Pham, Elizabeth Soberg, Catherine Triechel, and Labcorp performed all animal immunizations and bleeds, Mason Saunders performed the HDX mass spectrometry (MS), Michael Watson carried out the glycan occupancy using MS, as well as those who designed nanoparticles used in this work: Jacob Bale, George Ueda, Jorge Fallas, Isaac Lutz, Shunzi Wang, Robert de Haas, and Cara Chao. I also want to thank Justin Kollman for motivating me to pursue my PhD.

I want to thank everyone in the King lab for making it a great environment to work in everyday. Everyone in the lab comes from unique backgrounds and has a unique set of expertise, and I have learned so much from so many people. I'd like to thank Daniel Ellis, who designed the initial NC99 trihead and whose work on influenza laid a lot of groundwork for my PhD. I'd also like to thank Quinton Dowling, John C. Kraft, and Karla Luise-Herpoldt for their leadership and mentorship. Also thank you to Chloe for sitting across from me and keeping me sane.

I want to thank my parents, mom, dad, and Margery, for showing me the beauty of loving what you do and always supporting my education and career.

Lastly, thank you to Eric for always thinking through experiments with me and for supporting me everyday of my PhD.

Introduction

Influenza viruses currently persist as a major public health threat due to their high evolutionary rate that gives rise to frequent antigenic drift amongst circulating strains (Carrat and Flahault 2007; Bedford et al. 2014). This strain divergence is due in large part to diversity in the surface glycoprotein hemagglutinin (HA) as a result of immune pressure (Koel et al. 2013; Rejmanek et al. 2015). Despite its variation amongst strains, HA characterization has revealed two functionally conserved antigenic sites: the receptor binding site (RBS) in the head domain, which mediates host cell entry by binding to sialic acid on host glycoproteins, and a conserved antigenic region in the HA stem that is involved in host membrane fusion (Wu and Wilson 2017). The identification of several bNAbs against these sites has made them central targets in vaccine design efforts (Ekiert et al. 2012; Whittle et al. 2011; P. S. Lee et al. 2012; Krause et al. 2011; Dreyfus et al. 2012; Kallewaard et al. 2016; Li et al. 2022; McCarthy et al. 2018). The HA head is immunodominant and antibodies that bind near the RBS typically exhibit potent neutralization by blocking receptor binding (Altman et al. 2015; Wu and Wilson 2017; Angeletti et al. 2017). However, high levels of antigenic variation in the head domain allow influenza viruses to evade head-directed immunity through antigenic drift (Altman, Angeletti, and Yewdell 2018). Thus, broadly neutralizing antibodies (bNAbs) targeting the conserved RBS itself are rarely elicited by infection or vaccination, and response breadth is often limited by frequent residue mutations in the RBS periphery (Zost et al. 2019). By contrast, antibodies targeting the stem epitope tend to react more broadly to HAs from different influenza viruses, but these antibodies are not always neutralizing and they are difficult to elicit due to the subdominance of the stem. Recently, broadly protective antibodies against additional antigenic sites on HA have been discovered, including the stem anchor epitope (Guthmiller et al. 2022) and the trimer interface in the head domain (Watanabe et al. 2019; Bangaru et al. 2019; J. Lee et al. 2016). The broad binding of trimer interface-directed antibodies against divergent HA subtypes makes this site an intriguing vaccine target. Although they lack neutralizing activity, initial reports indicate that trimer interface-directed antibodies can be protective in animal models (Watanabe et al. 2019; Bangaru et al. 2019).

In addition to antigenic drift, influenza viruses use glycosylation of their surface proteins as a mechanism of immune evasion. Analysis of HA sequences obtained over the past century has revealed that the HA head has acquired more glycans over time, and this has been shown to both prevent antibody binding and to lower the number of mutations required for immune evasion (Kobayashi and Suzuki 2012; Wei et al. 2010). These observations have inspired the use of glycan engineering in vaccine design as a means to direct immune responses to target epitopes. Previous studies have generated hyperglycosylated immunogens by introducing new N-linked glycosylation motifs in the immunodominant head domain, resulting in the diversion of antibody responses onto conserved, subdominant epitopes in either the stem domain (Eggink, Goff, and Palese 2014) or the trimer interface (Bajic et al. 2019). A reduction in non-neutralizing trimer interface responses was seen in a separate study that combined hyperglycosylation and disulfide bond engineering in full-length HA ectodomains, but this did not increase the elicitation of broadly-reactive RBS-directed antibodies (Thornlow et al. 2021).

Four divergent subtypes of influenza that have been circulating in humans seasonally over the past century, namely H1N1, H3N2, B-Victoria, and B-Yamagata (Petrova and Russell 2018; Bedford et al. 2015). The current inactivated vaccine consists of these seasonal subtypes, however the exact strains of each of these are changed frequently to match those currently in circulation. In adults, these vaccines have been shown to elicit new antibodies that are strain-specific, and they also elicit a somewhat higher fraction of recall responses that are cross-reactive but found to be non-neutralizing (J. Lee et al. 2016). Another complicating factor is that these vaccines are currently produced in chicken eggs, rendering them vulnerable to irrelevant egg-adapted mutations (Raymond et al. 2016). Moreover, the process of virus inactivation by treatment with formaldehyde or detergents often disrupts antigen protein structure, removing neutralizing epitopes from being presented in this vaccine (Sabbaghi et al. 2019). Given these shortcomings of the current seasonal vaccine, it is only anywhere between 10-60% effective in any given year (Flannery et al. 2020), solidifying the need for an improved vaccine.

Subunit vaccines provide an alternative to inactivated vaccines, as they have very good safety profiles and are able to present structurally defined antigens for targeted immunogenicity (Plotkin 2014). While subunit vaccines can suffer from weak potency, the use of adjuvants as well as the presentation of antigen on nanoparticles to present them in a multivalent array has shown to result in increased potency of the resulting immune response (López-Sagaseta et al. 2016; Bachmann and Jennings 2010). The genetic fusion of viral antigens onto naturally occurring protein nanoparticles has shown dramatic improvements in immunogenicity. The first example of this was the display of a high-affinity HIV antigen on lumazine synthase to create the ‘eOD-60mer’, which outperformed a stabilized HIV trimer to increase proliferation of target broadly-neutralizing VRC01 precursors (Jardine et al. 2015). Another example was an improved influenza vaccine candidate composed of HA on the 24mer ferritin nanoparticle, which elicited significantly higher HAI and neutralization titers than the inactivated trivalent influenza vaccine (Kanekiyo et al. 2013). In addition to naturally occurring scaffolds, *de novo* computational protein design has led to the creation of new protein nanoparticles to be used as vaccine platforms (Bale et al. 2016; Ueda et al. 2020). The multivalent display of both the stabilized respiratory syncytial virus (RSV) protein F on the nanoparticle I53-50 (Marcandalli et al. 2019), as well as HA on the I53_dn5 nanoparticle (Boyoglu-Barnum et al. 2021), have shown superior, neutralizing immune responses compared to the RSV-F trimer or the inactivated quadrivalent influenza vaccine (QIV), respectively, in both mouse and non-human primate (NHP) models. In response to the SARS-CoV-2 pandemic, the spike RBD presented on I53-50 was also shown to elicit dramatically higher neutralizing responses as compared to the stabilized spike trimer (Walls et al. 2020). Given these results of dramatically improved immunogenicity for several different pathogens, protein nanoparticle vaccines have been established as a highly efficacious vaccine platform.

An additional benefit of these newly designed protein nanoparticles over naturally occurring ones is that they are composed of two components that are expressed and purified separately, and only assemble into nanoparticles upon *in vitro* mixing (Bale et al. 2016; Ueda et al. 2020). This provides a high degree of control over combining any mixture of antigens fused to the

same nanoparticle component before nanoparticle assembly, allowing for the co-display of different antigens at defined ratios. This type of ‘mosaic’ nanoparticle when used to co-display multiple strains of influenza HA, both as trimer ectodomains (Boyoglu-Barnum et al. 2021) and as monomeric RBDs (Kanekiyo et al. 2019), has shown to elicit increased breadth in the elicited immune response as compared to the same strains presented on homotypic nanoparticles. The hypothesis behind this increase in breadth from a mosaic nanoparticle is that more broadly reactive B cells will be able to bind to a greater number of divergent co-displayed antigens, leading to a greater number of B-cell receptors (BCR) clustering together on these cells, giving them an activation boost over strain-specific B cells (Kanekiyo et al. 2019). Mosaic sarbecovirus RBD nanoparticles have also elicited high amounts of neutralization breadth in multiple studies (Cohen et al. 2022, 2021; Walls et al. 2021). In one of these studies, a mosaic of eight different RBD strains was compared to two mosaics, each with four different strains (Cohen et al. 2021). The 8-valent mosaic was found to elicit higher vaccine-mismatched ELISA and neutralization titers than either of the 4-valent mosaics, indicative that increasing diversity of co-displayed antigens stimulates increasing breadth in the elicited immune response. Beyond these studies, greater exploration into both the number and extent of diversity amongst co-displayed antigens will be needed to understand how to design vaccines that yield optimal immune response breadth. Additionally, to date, all reports of mosaic nanoparticle immunogens have tested co-display of antigens with wild-type sequences from various virus isolates; the use of synthetic or designed antigenic variation in mosaic nanoparticles remains unexplored.

In addition to nanoparticle display, protein subunit vaccines have improved dramatically since the development of neutralization-sensitive and structure-guided design approaches. The power of this approach was first demonstrated by the stabilization of neutralizing epitopes on RSV-F (McLellan et al. 2013). This study was inspired by another study done in the previous year, where the prefusion conformation of RSV-F was stabilized by two engineered disulfide bonds based on its crystal structure (Magro et al. 2012). They showed using negative-stain electron microscopy (nsEM) that this construct was in the prefusion state, compared to the soluble, unstabilized RSV-F, which formed only the more elongated postfusion conformation. Importantly, depletion of a human Ig preparation with the prefusion-stabilized construct resulted in no remaining microneutralization activity, whereas depletion with the postfusion construct resulted in potent microneutralization activity still remaining. Further motivation for the prefusion stabilization of RSV-F came from the discovery of new anti-RSV-F mAbs, such as D25 (Spits and Beaumont 2013), with greater neutralizing activity that targeted site 0, an epitope at the apex of RSV-F that is only present in the prefusion conformation. These studies lead to the stabilization of the prefusion F state by the introduction of a disulfide bond (‘DS’) and two hydrophobic, cavity-filling mutations (‘Cav1’) together to create DS-Cav1 (McLellan et al. 2013). They demonstrated that immunization with DS-Cav1 showed significantly higher neutralization titers as compared to postfusion RSV-F in both mice and NHPs. This study outlined the basis for neutralization- and structure-guided vaccine design, wherein the identification of neutralizing epitopes is used as a blueprint for designing vaccines that optimally stabilize and present those epitopes, while simultaneously destabilizing undesired or non-neutralizing epitopes that may compete for immunogenicity.

Learning from the stabilization of RSV-F, the McLellan group was able to adapt this strategy onto another type I viral fusion protein, coronavirus spike (S) protein. They were able to stabilize prefusion S by introducing two proline mutations (2P) within a loop at the apex of the protein in the prefusion conformation that undergoes a large conformational change to form the postfusion structure (Pallesen et al. 2017). This was also inspired by previous work done to stabilize HIV envelope in its trimeric form by the introduction of a proline mutation in addition to a disulfide bond to create SOSIP trimers with increased immunogenicity (Sanders et al. 2002). The S-2P stabilization of MERS-CoV resulted in higher neutralizing titers elicited in mice than wild-type (WT) S, as well as structure determination of a neutralizing antibody against the S2 stalk domain of the spike, a site more highly conserved than the RBD (Pallesen et al. 2017). Importantly, these mutations were able to be applied to the SARS-CoV-2 S protein when it caused a worldwide pandemic in 2019, and its formulation into two mRNA vaccines were the first licensed vaccines after only one year of development (Baden et al. 2021; Polack et al. 2020). Taken together, these studies underscore the efficacy of stabilizing antigens that present neutralizing epitopes and also demonstrate the importance of antigen design portability, both amongst varying strains and even amongst completely different pathogens.

Here, I aimed to combine all of the current knowledge on nanoparticle immunogens and antigen engineering to further understand and improve influenza vaccines. I expanded the designed trimeric HA RBD antigens we call ‘triheads’ that stabilize neutralizing head epitopes while diminishing non-neutralizing ones. I report on combinations of immune refocusing within the trihead platform, including co-display, hyperglycosylation, and hypervariable sequences. I also show that the design of triheads can be adapted to several strains of H1s, as well as H3 and type B strains. Finally, I will turn the focus onto full-length HA ectodomains in efforts to understand how HA mosaic nanoparticles elicit superior, broadly-reactive stem responses.

Chapter 1. Combinatorial immune refocusing within the influenza hemagglutinin head elicits cross-neutralizing responses

1.1 Results

1.1.1 Design and Immunogenicity of Hyperglycosylated Trihead Nanoparticle Immunogens

In the accompanying manuscript we describe the design of a “trihead” antigen in which the head domain of H1 A/New Caledonia/20/1999 (NC99) was stabilized in a native-like trimeric state via hydrophobic mutations at the trimer interface and a rigid fusion to the trimeric component of the I53_dn5 nanoparticle (Ellis et al., n.d.). We also show that this stabilized immunogen, which we refer to here as TH-NC99 (**Figure 1.1A**), elicits potent neutralization and HAI activity in immunized mice. To focus the immune responses elicited by this immunogen to the conserved RBS, three and five additional N-linked glycans were engineered into epitopes distant from the RBS to create the hyperglycosylated NC99 triheads TH-NC99-7gly and TH-NC99-9gly, respectively (**Figure 1.1A**). The new glycans were designed using the Rosetta modeling suite, both to guide sequon design and model glycan structure (Adolf-Bryfogle et al. 2021; Leman et al. 2020). TH-NC99 constructs with individual glycan additions were first evaluated for their secretion from HEK293F cells (data not shown) and those that maintained expression were then combined. We also generated “monohead” antigens lacking the trimer interface-stabilizing mutations and rigidifying disulfide bond, which form monomers with exposed trimer interfaces (Ellis et al., n.d.), bearing the four wild-type (MH-NC99) and five additional (MH-NC99-9gly) N-linked glycans. Amino acid sequences for all novel proteins used in this study can be found in **Table S1.1**. The monohead and trihead antigens were secreted from HEK293F cells as genetic fusions to the I53_dn5B trimer and purified via immobilized metal affinity chromatography (IMAC) and size exclusion chromatography (SEC) (**Figure S1.1A**). SDS-PAGE revealed reduced migration for the hyperglycosylated monohead and trihead subunits compared to their wild-type counterparts (**Figures 1.1B** and **S1.1B**). Treatment of the trimeric components with PNGaseF resulted in a large decrease in apparent molecular weight by SDS-PAGE and uniform migration of all constructs. Biolayer interferometry (BLI) using the anti-RBS bNAb C05 (Ekiert et al. 2012) showed similar binding profiles for all five components, indicating that the hyperglycosylated antigens maintain RBS antigenicity (**Figure 1.1C**). By contrast, BLI using the anti-trimer interface mAb FluA-20 (Bangaru et al. 2019) showed high binding to monohead components but minimal binding to all trihead components, confirming stable closure of the trimer interface in the trihead antigens. Lastly, BLI using the anti-lateral patch mAb 6649 (Raymond et al. 2018) showed nearly full binding to TH-NC99-7gly but greatly diminished binding to TH-NC99-9gly, likely due to the additional glycan at position 167 in TH-NC99-9gly that is in the center of the 6649 epitope. MH-NC99-9gly showed moderate 6649 binding, possibly due to less consistent glycosylation at that position than in TH-NC99-9gly.

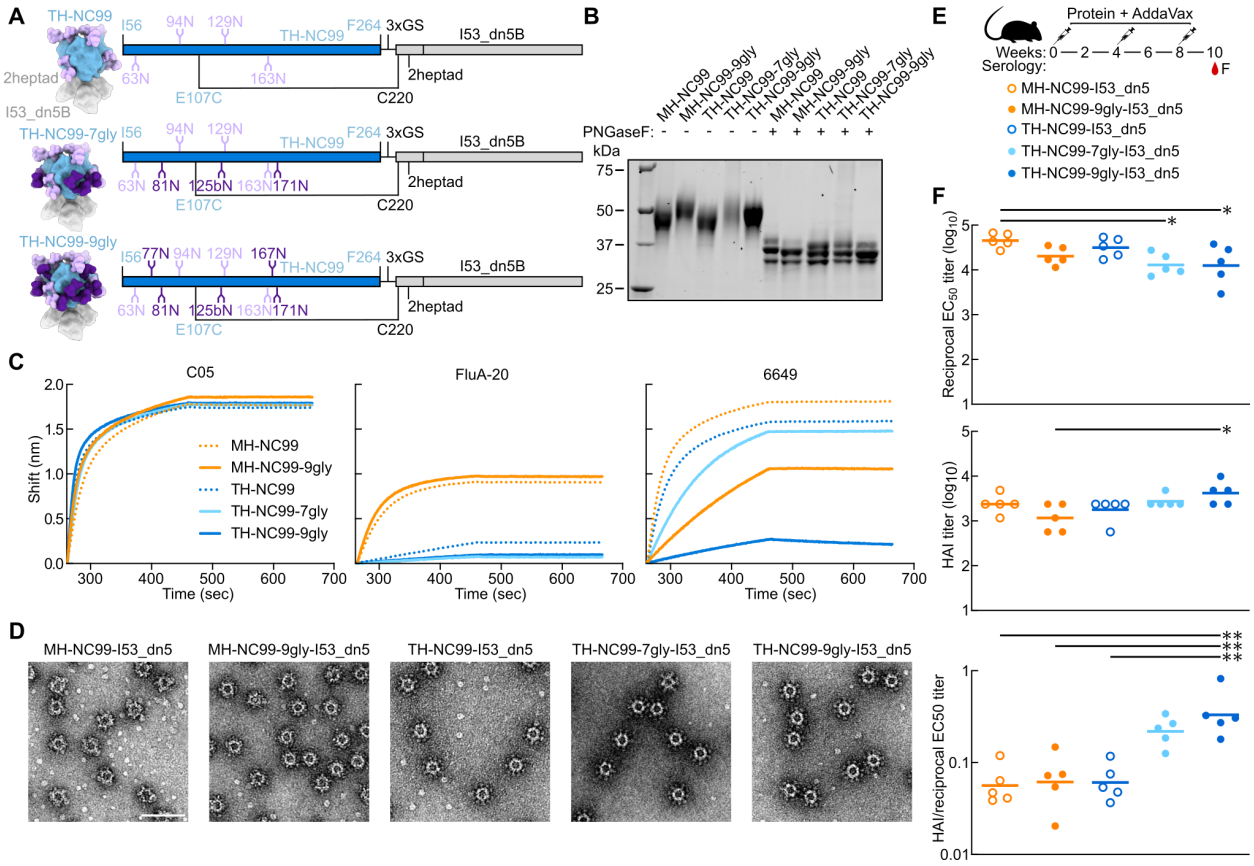

Figure 1.1 Design and Immunogenicity of Hyperglycosylated NC99 Trihead Nanoparticle Immunogens

(A) Model structures and gene diagrams for wild-type and hyperglycosylated NC99 triheads with wild-type glycans in light purple and glycan knock-ins in dark purple. NC99 HA numbering is in blue and trihead model numbering is in black.

(B) Reducing SDS-PAGE of wild-type and hyperglycosylated NC99 monoheads and triheads without and with PNGaseF digestion.

(C) BLI of wild-type and hyperglycosylated NC99 monoheads and triheads against C05, FluA-20, and 6649.

(D) nsEM micrographs of hyperglycosylated NC99 monohead and trihead I53_dn5 nanoparticles. Scale bar = 100 nm.

(E) Schematic illustrating mouse study timeline, immunizations, and serology timepoint.

(F) Week 10 NC99-foldon trimer ELISA titers plotted as the reciprocal EC_{50} titer, hemagglutination inhibition (HAI) titers, and the ratio of HAI/reciprocal EC_{50} titers of hyperglycosylated NC99 monohead and trihead nanoparticles in BALB/c mice. Statistical significance was determined using one-way ANOVA with Tukey's multiple comparisons test; ∗p < 0.05; ∗∗p < 0.01.

To quantify glycan occupancy at each site, all trihead components were analyzed using peptide mass spectrometry (Struwe et al. 2017; Stavenhagen et al. 2013). Glycan occupancy in TH-NC99 was high across all sites with the exception of N163, which was only about half occupied (45.1%; **Table S1.2**). The wild-type sites in TH-NC99-7gly showed similar occupancy, including half occupancy at N163 (44.3%). The engineered glycosylation sites in TH-NC99-7gly had high occupancy at N125b, about half occupancy at N81 (46.2%), and low occupancy at

N171 (20.1%). The additional site at N125b was not observed as an isolated glycopeptide and could only be indirectly quantified by the peptide spanning the additional glycan site at N129. For TH-NC99-9gly, the additional N77 glycosylation site was only observed in a glycopeptide that also comprised N81 and showed either single (63%) or double (37%) occupancy. The last two sites in TH-NC99-9gly were only observed on a long glycopeptide containing three sequons. Based on the occupancy levels measured, it is likely that N167 is highly occupied (>90%) while N171 is less than 15% occupied, as this would be consistent with the occupancy levels observed for these sites in TH-NC99-7gly.

The monohead and trihead components were then combined with purified I53_dn5A pentamer *in vitro* at a 1:1 molar ratio to form icosahedral I53_dn5 nanoparticles displaying either 60 monohead monomers or 20 trihead trimers. Purification by SEC (**Figure S1.1C**) yielded pure, monodisperse preparations of nanoparticles according to SDS-PAGE, nsEM, and dynamic light scattering (DLS) (**Figures 1.1D, S1.1D, and S1.1E**). Efficient assembly was observed for all trihead nanoparticles, as little residual component was observed during SEC purification (**Figure S1.1C**; peak at ~17 mL). By contrast, substantial residual component was observed during SEC of the monohead nanoparticle assemblies, indicating less efficient assembly.

We evaluated the hyperglycosylated trihead nanoparticle immunogens in an initial immunogenicity study in mice. BALB/c mice were immunized with 1.5 μg of nanoparticle immunogen formulated with AddaVax at weeks 0, 4, and 8 **(Figure 1.1E)**. Strain-matched NC99 binding titers from serum collected at week 10 showed reduced binding in all hyperglycosylated groups compared to their wild-type counterparts **(Figure 1.1F)**. Conversely, NC99 hemagglutination inhibition (HAI) titers were highest in the TH-NC99-9gly group and lowest in the MH-NC99-9gly group. Plotting the ratio of HAI/binding titers revealed a trend towards a stepwise increase with increasing glycosylation in the trihead groups, suggesting a higher proportion of on-target receptor-blocking antibodies. Only the MH-NC99-9gly sera competed with FluA-20 binding in competition ELISAs, yet these sera showed the least amount of competition with C05 **(Figure S1.1F-S1.1G)**. These results suggest that hyperglycosylation refocused vaccine-elicited antibodies onto receptor-blocking epitopes in the case of the trihead immunogens, and onto the trimer interface in the case of the monohead immunogens.

1.1.2 Design of Hyperglycosylated Trihead Antigens from Additional H1 HAs

We and others have recently reported that mosaic nanoparticle immunogens, which co-display multiple antigenic variants on the same nanoparticle surface, can induce broadly protective responses against related viruses by eliciting antibodies that target conserved epitopes (Kanekiyo et al. 2019; Boyoglu-Barnum et al. 2021; Cohen et al. 2021; Walls et al. 2021; Sliepen et al. 2022; Cohen et al. 2022; Brinkkemper et al. 2022). To enable mosaic trihead display as a potential route to enhancing breadth amongst H1 strains, we adapted the NC99 trihead design strategy to three other divergent H1s: A/South Carolina/1/1918 (TH-SC18), A/Puerto Rico/8/1934 (TH-PR34), and A/Michigan/45/2015 (TH-MI15). NC99 and PR34 are both seasonal H1 strains, while SC18 and MI15 are pandemic H1 strains. We again made corresponding monoheads for comparison. These antigens were all connected to the I53_dn5B trimer using one heptad repeat of the GCN4-based coiled-coil, as this linker length was found to

yield optimal cross-reactive antibody responses in mice (Ellis et al., n.d.). The same disulfide bond in TH-NC99 between the base of the trihead and the coiled-coil linker was used, as well as similar stabilizing mutations at the trimer interface, although the amino acids used at positions 203 and 205 differed among strains (**Figure 1.2A** and **Table S1.1**). The final designs for TH-PR34 and the monohead and trihead variants of SC18 included one glycan knock-in each, at positions 63 and 125b, respectively, which dramatically enhanced expression and stability. Additionally, P26S and V84E in TH-PR34, as well as A198E in both TH-SC18 and TH-MI15, were key expression-enhancing mutations.

All four triheads maintained binding to RBS-directed antibodies, with minimal FluA-20 binding by BLI, indicating trihead closure (**Figures 1.2B and S1.2A**). By contrast, monohead versions of each strain all showed high binding to both RBS antibodies and FluA-20. The trihead and monohead components were purified using SEC (**Figures S1.2B and S1.2C**) prior to *in vitro* assembly into I53_dn5 nanoparticles. We prepared a cocktail of nanoparticles by mixing together the four individually assembled trihead nanoparticles, as well as mosaic nanoparticles in which the four trihead components were mixed together prior to addition of I53_dn5A pentamer (**Figure 1.2C**). All nanoparticles were then purified using SEC and their purity and monodispersity were verified by SDS-PAGE, DLS, and nsEM (**Figures S1.3A-S1.3D**). All four monovalent trihead nanoparticles exhibited individually resolved trihead densities on the nanoparticle exteriors in nsEM averages, while the MH-PR34-I53_dn5 nanoparticle lacked visible antigen density due to the flexibility of the monoheads (**Figure 1.2D**). Taken together, the BLI, SEC, and nsEM averages indicate the formation of closed, relatively rigid trihead nanoparticle immunogens for all four strains.

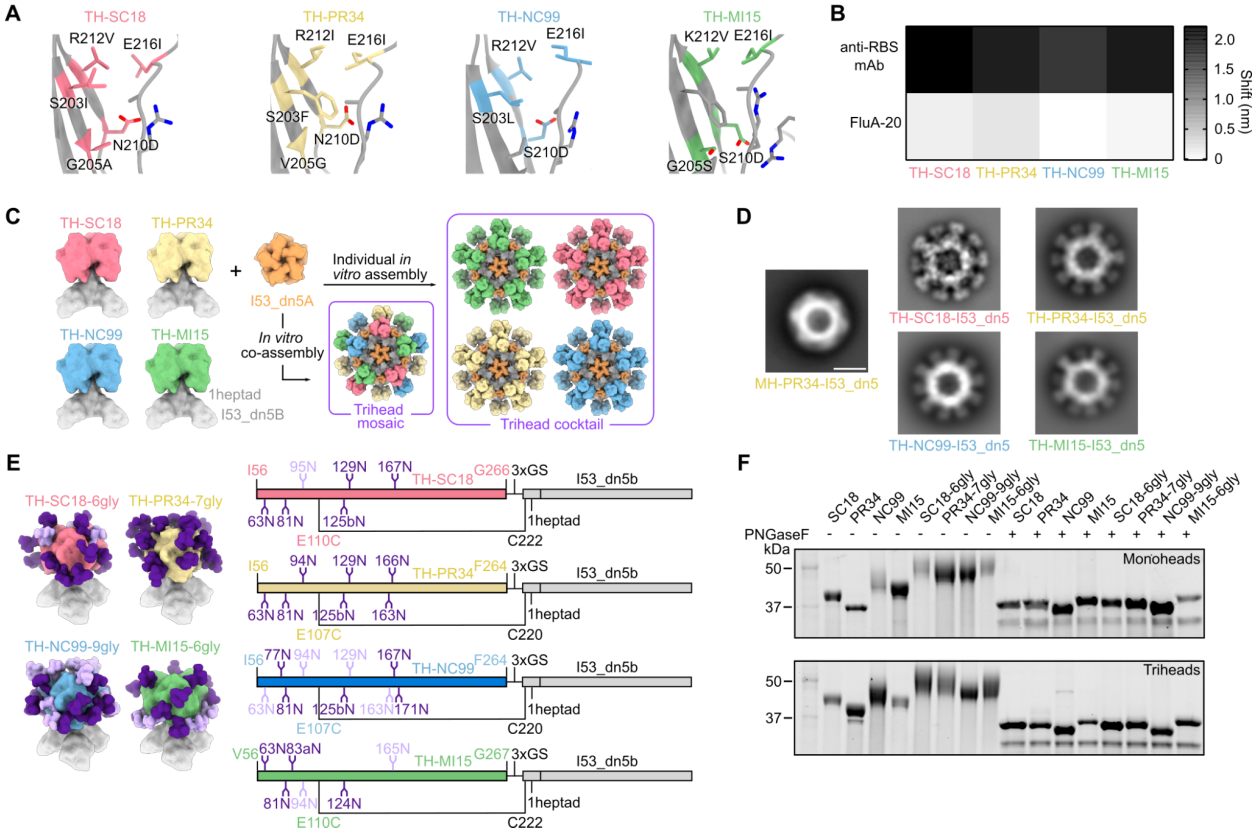

Figure 1.2 Design of Hyperglycosylated Trihead Antigens from Additional H1 HAs
(A) Diagram of head trimer interfaces for TH-SC18, TH-PR34, TH-NC99, and TH-MI15, where mutated residues are colored and labeled.
(B) BLI of trihead components against RBS-directed mAbs (5J8, anti-PR34, and C05) and FluA-20.
(C) Schematic of TH-SC18, TH-PR34, TH-NC99, and TH-MI15 constructs and their *in vitro* assembly into mosaic or cocktail I53_dn5 nanoparticles.
(D) nsEM 2D class averages of MH-PR34-I53_dn5 and trihead I53_dn5 nanoparticles. Scale bar = 25 nm.
(E) Model structures and gene diagrams for hyperglycosylated triheads with wild-type glycans in light purple and glycan knock-ins in dark purple. Strain-specific H1 HA numbering is in respective HA strain color and trihead model numbering is in black.
(F) Reducing SDS-PAGE of wild-type and hyperglycosylated monoheads and triheads without and with PNGaseF digestion.

As with TH-NC99-9gly, engineered glycans were used to mask epitopes outside the RBS in each H1 trihead. Individual glycans added to TH-SC18 were tested for their effects on trihead secretion before combination into one hyperglycosylated construct. These data were then used to guide hyperglycosylation of TH-PR34 and TH-MI15. TH-SC18-6gly has one wild-type and five engineered glycans, TH-PR34-7gly has zero wild-type and seven engineered glycans, and TH-MI15-6gly has two wild-type and five engineered glycans (**Figure 1.2E** and **Table S1.1**). All hyperglycosylated trihead components showed apparent increases in molecular weight by SDS-PAGE compared to their wild-type counterparts, while treatment with PNGase F resulted in nearly uniform migration of all constructs at a lower apparent molecular weight (**Figures 1.2F**

and S1.2C). All hyperglycosylated trihead components maintained the desired antigenic profile of high anti-RBS antibody binding with minimal FluA-20 binding and had circular dichroism (CD) spectra that closely matched those of the corresponding non-hyperglycosylated triheads, indicating they retained their native structure (**Figures S1.4A-S1.4C**). The four hyperglycosylated trihead components were combined in an equimolar mixture and then co-assembled *in vitro* with the I53_dn5A pentamer to form a hyperglycosylated trihead mosaic nanoparticle that was purified by SEC (**Figure S1.3A**). SDS-PAGE, DLS, and nsEM of the purified assembly revealed monodisperse nanoparticles of the expected size and morphology (**Figures S1.3B-S1.3D**).

We compared the stabilities of the hyperglycosylated monohead and trihead components using hydrogen-deuterium exchange mass spectrometry (HDX-MS) and nano differential scanning fluorimetry (nanoDSF). Deuterium uptake profiles across MH-NC99-9gly and all four hyperglycosylated triheads were consistent with the antigens adopting similar conformations, although with some local differences (**Figure S1.5A**). For example, HDX-MS analysis of RBS peptides showed that TH-SC18-6gly has greater dynamics at the 190-helix and 220-loop relative to the other three strains of hyperglycosylated triheads (**Figures S1.5B-S1.5C**). Similarly, trimer interface peptides lying in the 220-loop and 200-loop in the TH-SC18-6gly were also less ordered, especially compared to TH-NC99-9gly and TH-PR34-7gly, which were the most ordered in these regions. Comparing MH-NC99-9gly and TH-NC99-9gly showed that the monohead antigen displayed substantially higher exchange than the trihead at the trimer interface in the 220-loop, as well as slightly elevated dynamics in other regions. Thermal denaturation monitored by intrinsic tryptophan fluorescence showed similar trends in stability, where TH-SC18-6gly had the lowest melting temperature (T_m) and TH-NC99-9gly had the highest T_m among the triheads (**Figure S1.5D**). Additionally, three out of four hyperglycosylated monoheads had T_ms ≥4°C lower than their trihead counterparts. Together, these analyses indicate that the trihead antigens are locally and globally more stable than monomeric RBDs in addition to being rigidly linked to the I53_dn5 nanoparticle scaffold.

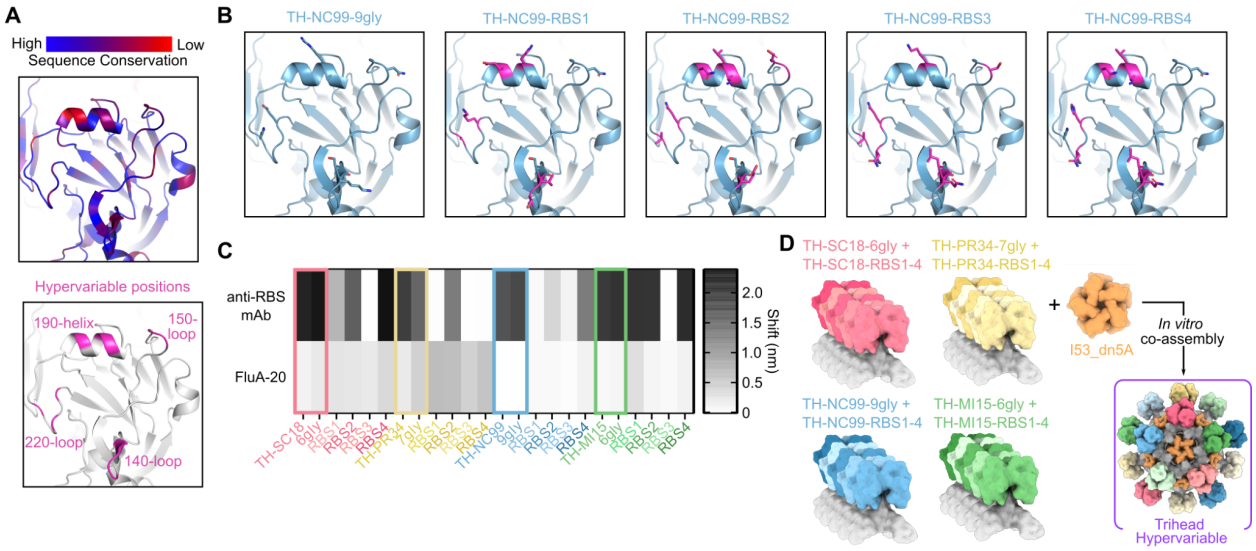

Figure 1.3 Design and Characterization of Hypervariable Trihead Immunogens
(A) Sequence conservation amongst 643 unique H1 sequences (top) and positions mutated in hypervariable library as dark pink (bottom) modeled on the NC99 HA structure (PDB: 7SCN).
(B) TH-NC99-9gly wild-type and hypervariable variants modeled onto the NC99 HA structure (PDB: 7SCN), with all positions mutated in the library shown as sticks, wild-type residues in blue, and mutated residues in magenta.
(C) BLI of triheads and hyperglycosylated triheads, with colored squares around these constructs, and trihead RBS variant components against RBS-directed mAbs (5J8, anti-PR34, and C05) and FluA-20.
(D) Schematic of hypervariable trihead components and assembly into an I53_dn5 nanoparticle.

1.1.3 Design and Characterization of Hypervariable Trihead Immunogens

As a further test of the hypothesis that mosaic nanoparticle display focuses antibody responses on conserved epitopes, we designed a hypervariable antigen library featuring mutations within the RBS periphery. This is a particularly variable region in hemagglutinins from different influenza virus strains, and mutations in this region are a central driver of antigenic drift (**Figure 1.3A**) (Koel et al. 2013). We reasoned that co-display of a library of trihead variants with mutations in the RBS periphery may elicit fewer strain-specific antibodies in favor of responses targeting the conserved RBS. We constructed our library to recapitulate this variability by introducing naturally occurring mutations or those identified by deep mutational scanning into key hypervariable positions (**Figure 1.3A**) (Doud and Bloom 2016; Wu et al. 2017). We made four variants of each hyperglycosylated trihead, each comprising a unique combination of 2-10 amino acid mutations in the RBS periphery (**Figure 1.3B** and **Table S1.3**). Binding studies using BLI showed that the variants had distinct antigenic profiles as intended, with some mutations leading to a complete loss of binding to particular anti-RBS mAbs (**Figures 1.3C and S1.4A**). However, all RBS variants maintained minimal FluA-20 binding, exhibited the expected SEC elution profiles and apparent molecular weights on SDS-PAGE, and had similar CD spectra showing a mixture of alpha helix and beta sheet, indicating that they formed well-folded, closed triheads (**Figures 1.3C, S1.4C, and S1.6A-S1.6B**). The four base hyperglycosylated triheads and all of their variants were then pooled and co-assembled with I53_dn5A pentamer to generate a hyperglycosylated, hypervariable nanoparticle containing 20 unique trihead antigens

(**Figures 1.3D**). This hypervariable trihead nanoparticle was purified by SEC and was monodisperse by SDS-PAGE, DLS, and nsEM (**Figures S1.3A-S1.3D**). Co-display of all trihead mosaic nanoparticles (TH-mosaic-I53_dn5, TH-hyperglycosylated-mosaic-I53_dn5, and TH-hypervariable-hyperglycosylated-mosaic-I53_dn5) was confirmed using sandwich BLI by comparison to the TH-cocktail-I53_dn5 immunogen (**Figure S1.6C**). The NC99-specific mAb C05 was first loaded onto AR2G biosensors, followed by nanoparticle loading and sequential binding to a PR34-specific mAb and 5J8, which binds both MI15 and SC18. Although all nanoparticles bound to the immobilized C05 mAb, only the three mosaic nanoparticles showed subsequent binding to the PR34-specific mAb and 5J8. These data indicate that the mosaic nanoparticles co-display trihead antigens that bind all three antibodies, and that there is no detectable subunit exchange in the cocktail nanoparticle preparation. We note that the lower amount of hypervariable trihead nanoparticle loading and subsequent antibody binding is consistent with the individual hypervariable trihead component BLI, which demonstrated that some mutations within the RBS periphery abrogated specific mAb binding, particularly for the anti-PR34 mAb (**Figure 1.3C** and **S1.4A**).

1.1.4 Vaccine-elicited Antibody Responses in Rabbits Immunized with Monohead and Trihead Nanoparticles

We then evaluated our series of monohead and trihead nanoparticle immunogens in an immunogenicity study in New Zealand white rabbits. We chose rabbits because their long CDRH3 repertoire may facilitate the elicitation of antibodies that can penetrate into the RBS (Whittle et al. 2011; Ekiert et al. 2012; Sanders et al. 2015), and also because they permit the collection of sufficient serum to conduct a number of distinct serological analyses. Rabbits were immunized at weeks 0, 4, and 20 with 25 μg immunogen formulated with AddaVax (**Figure 1.4A**). Negligible binding titers at week 0 against a vaccine-matched MI15 HA-foldon trimer showed that there were no pre-existing anti-HA antibodies in these animals (**Figure S1.7A-B**). Evaluation of vaccine-matched (NC99 and MI15) serum antibody binding, HAI, and microneutralization using sera obtained at weeks 6 and 22 revealed several differences between the groups. First, the cocktail and mosaic monohead groups consistently had lower binding, HAI, and neutralization titers than all other groups at week 6, although the differences were not always statistically significant (**Figures 1.4B-D**). Interestingly, the hyperglycosylated monohead mosaic elicited antibody responses that were significantly higher than the other monohead groups and comparable to the trihead immunogens. At week 22, the monohead cocktail group had significantly lower NC99-neutralizing activity than all other groups, as well as NC99 HAI titers that trended lower (**Figures 1.4E and S1.5C-D**). By contrast, the monohead and trihead mosaic groups had significantly lower MI15-neutralizing activity than most of the other groups (**Figure 1.4E**). Taken together, the data show that the monohead cocktail and mosaic nanoparticle immunogens were generally less immunogenic than the other groups, while the hyperglycosylated and hypervariable nanoparticles consistently elicited potent vaccine-matched responses.

Across four vaccine-mismatched H1 strains (see **Table S1.1**), the hyperglycosylated monohead group had the highest binding titers of all groups, both at weeks 6 and 22 (**Figures 1.4B and S1.7C**). The hyperglycosylated monohead also induced relatively high levels of HAI, however it

elicited lower neutralizing activity than the hyperglycosylated trihead groups for all mismatched H1 strains at both weeks 6 and 22, although this was not always significant (**Figures 1.4C-E and S1.7D**). The relatively low level of neutralizing activity despite high binding titers indicates that the hyperglycosylated monohead nanoparticle elicited a high proportion of non-neutralizing antibodies, likely targeting the trimer interface. Interestingly, glycan masking of antigens has been shown to alter where on the antigen the majority of responses are being directed, but does not change the overall magnitude of the response (Duan et al. 2018; Bajic et al. 2019). By contrast in this study, the hyperglycosylated monohead mosaic outperformed its non-hyperglycosylated comparator group in every comparison, including overall binding titers across the strains tested, although not always with statistical significance. Alongside the hyperglycosylated monohead, the hyperglycosylated trihead group had the highest mismatched HAI responses against most strains tested (Iowa43, USSR77, and Brisbane07) with the exception of Malaysia54, where the hypervariable trihead group induced the highest HAI titers. This trend in HAI was mirrored in the microneutralization assays, where the highest neutralizing titers were obtained from the two hyperglycosylated trihead groups at weeks 6 and 22 for Malaysia54, and at week 6 for SI06. For the mismatched viruses FM47 and USSR77, neutralizing responses were low across all groups at week 6, with the exception of measurable activity in the hypervariable trihead group. However, by week 22 all trihead groups neutralized these viruses more potently than all monohead groups. Taken together, the consistently high vaccine-mismatched HAI and neutralization obtained from the two hyperglycosylated trihead groups suggests that stable trihead closure and hyperglycosylation both contributed towards eliciting superior immune responses.

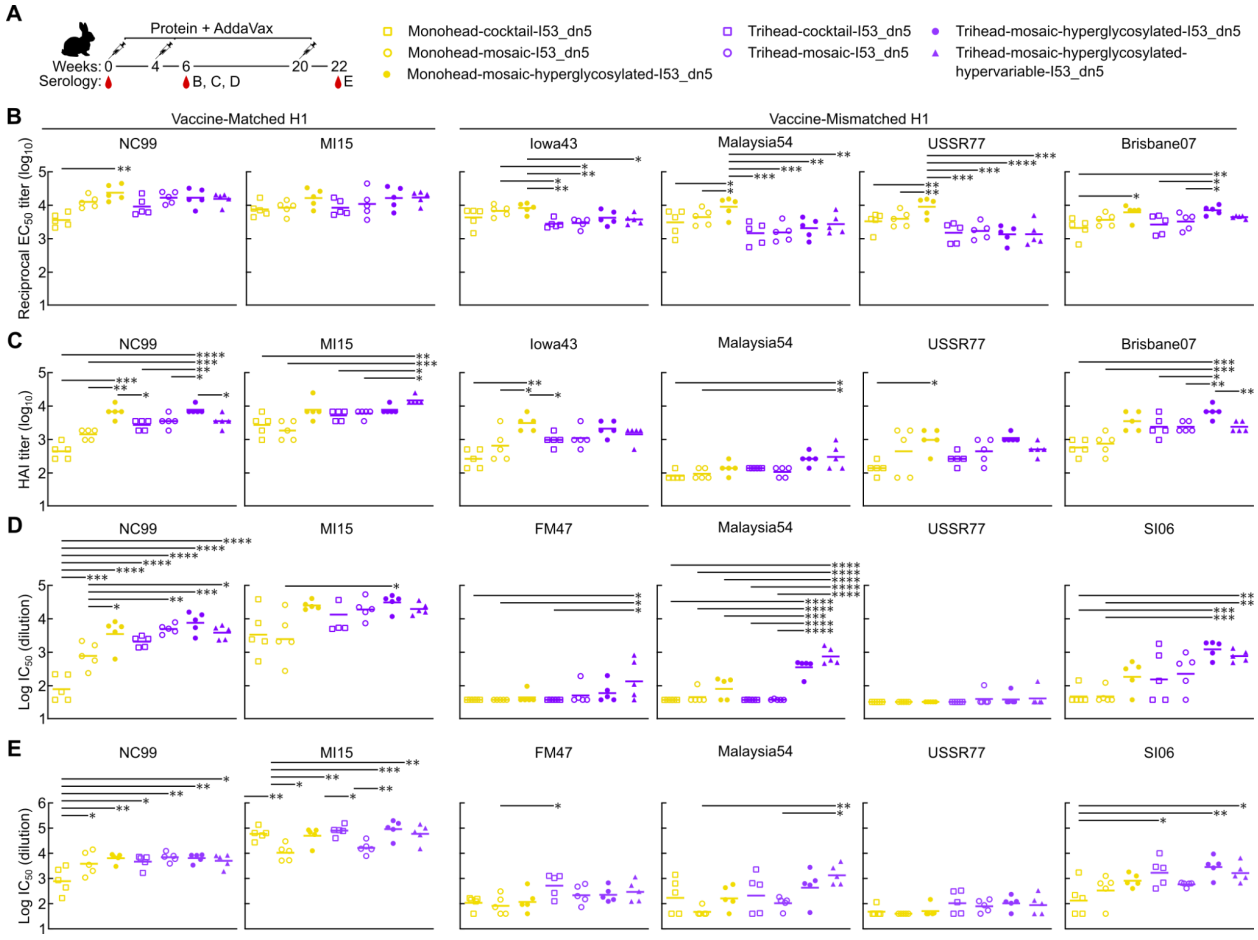

Figure 1.4 Vaccine-elicited Antibody Responses in Rabbits Immunized with Monohead and Trihead Nanoparticles

(A) Hypervariable trihead nanoparticle rabbit immunization schedule and groups.

(B-D) B. ELISA binding titers, C. HAI titers, and D. Microneutralization titers in immune sera at week 6.

(E) Microneutralization titers at week 22.

Statistical significance was determined using one-way ANOVA with Tukey's multiple comparisons test; ∗p < 0.05; ∗∗p < 0.01; ∗∗∗p < 0.001; ∗∗∗∗p < 0.0001.

1.1.5 Epitope Mapping of Vaccine-Elicited Antibody Responses

We next sought to determine the epitope specificities of the serum antibodies elicited by each vaccine (**Figure 1.5A**). We first compared RBS knockout probes NC99-L194W and NC99-T155N/K157T to wild-type NC99 as ELISA antigens to assess the fraction of the antibody response in each group directed at the RBS. NC99-L194W mutates a key highly conserved residue within the RBS pocket, introducing steric bulk that knocks out only antibodies that bind directly to the sialic acid binding pocket, while NC99-T155N/K157T introduces an N-linked glycan that more broadly prevents binding of RBS-directed antibodies (Ellis et al., n.d.). Serum antibody binding to both RBS knockout probes was considerably lower than to wild-type NC99 in all trihead groups (binding ratios of 0.08-0.64 for NC99-L194W and 0.03-0.65 for NC99-T155N/K157T), while the differences in relative binding in the monohead groups was

smaller (binding ratios of 0.23-1.07 and 0.19-1.07, respectively) (**Figure 1.5B-C**). We attribute the greater reduction in binding using the T155N/K157T probe compared to the L194W to the fact that the glycan knock-in probe will interfere with antibodies targeting a larger area of the antigen. These results clearly indicate that the trihead immunogens elicited substantially more RBS-directed responses than the monohead immunogens.

We also used nsEM polyclonal epitope mapping (ns-EMPEM; (Bianchi et al. 2018; Han et al. 2021) to directly visualize where vaccine-elicited serum antibodies bound HA. MI15 strain-matched ns-EMPEM using week 6 serum showed that only a small fraction of the antibodies elicited by the hyperglycosylated monohead mosaic bound the RBS of intact HA trimers, and we mostly observed individual Fabs bound to HA monomers (**Figure 1.5D**). These Fabs likely bind the trimer interface, which has been shown to disrupt trimerization, and indeed our class averages closely resemble those originally reported for FluA-20 (Bangaru et al. 2019). By contrast, all three mosaic trihead immunogens elicited antibodies that bound mostly to the RBS of intact HA trimers, though a small fraction of Fab bound to monomeric HA was also observed in these groups. We were able to discern RBS-targeting antibody classes with several slightly different angles of approach. Notably, the hypervariable trihead group also exhibited density for Fabs binding to the side of the MI15 HA head. This may be attributed to the lack of a glycan in TH-PR34-7gly, TH-MI15-6gly, and TH-SC18-6gly near residues 119-122 (SC18 numbering), in addition to the low occupancy of the N-linked glycan introduced at position 171 in TH-NC99, resulting in inefficient masking of this epitope. We also performed ns-EMPEM against the vaccine-mismatched Malaysia54 HA using week 22 sera to determine which epitopes were targeted by cross-reactive vaccine-elicited antibodies. We again observed predominantly Fab-bound HA monomers in the hyperglycosylated monohead group, indicating a high proportion of trimer interface-directed responses (**Figure 1.5E**). Week 22 trihead mosaic serum also revealed only Fab-bound HA monomers, but in contrast to the hyperglycosylated monohead group, these Fabs targeted a multitude of various epitopes in the head domain. Finally, in both the hyperglycosylated and hypervariable mosaic trihead sera we observed Fabs bound only to trimeric Malaysia54 HA, mostly targeting the side of the head, in contrast to the predominantly RBS-directed antibodies seen in these sera at week 6 against the vaccine-matched MI15.

We draw several conclusions from these RBS knockout probe binding and ns-EMPEM data. First, both sets of data demonstrate that monomeric RBD antigens elicit a high proportion of trimer interface-directed antibodies, while the closed, stabilized trihead antigens elicit antibodies predominantly targeting the RBS. Second, the week 22 mismatched ns-EMPEM suggests that hyperglycosylation further decreases the elicitation of trimer interface-directed antibodies by trihead immunogens. Third, the cross-reactive responses obtained with the monohead antigens largely derived from trimer interface-directed antibodies, explaining why vaccine-mismatched neutralization is low. Finally, the cross-reactive responses obtained with the hyperglycosylated trihead immunogens predominantly target an epitope on the side of the head rather than the RBS, especially for the hypervariable immunogen that contains numerous mutations in the RBS periphery.

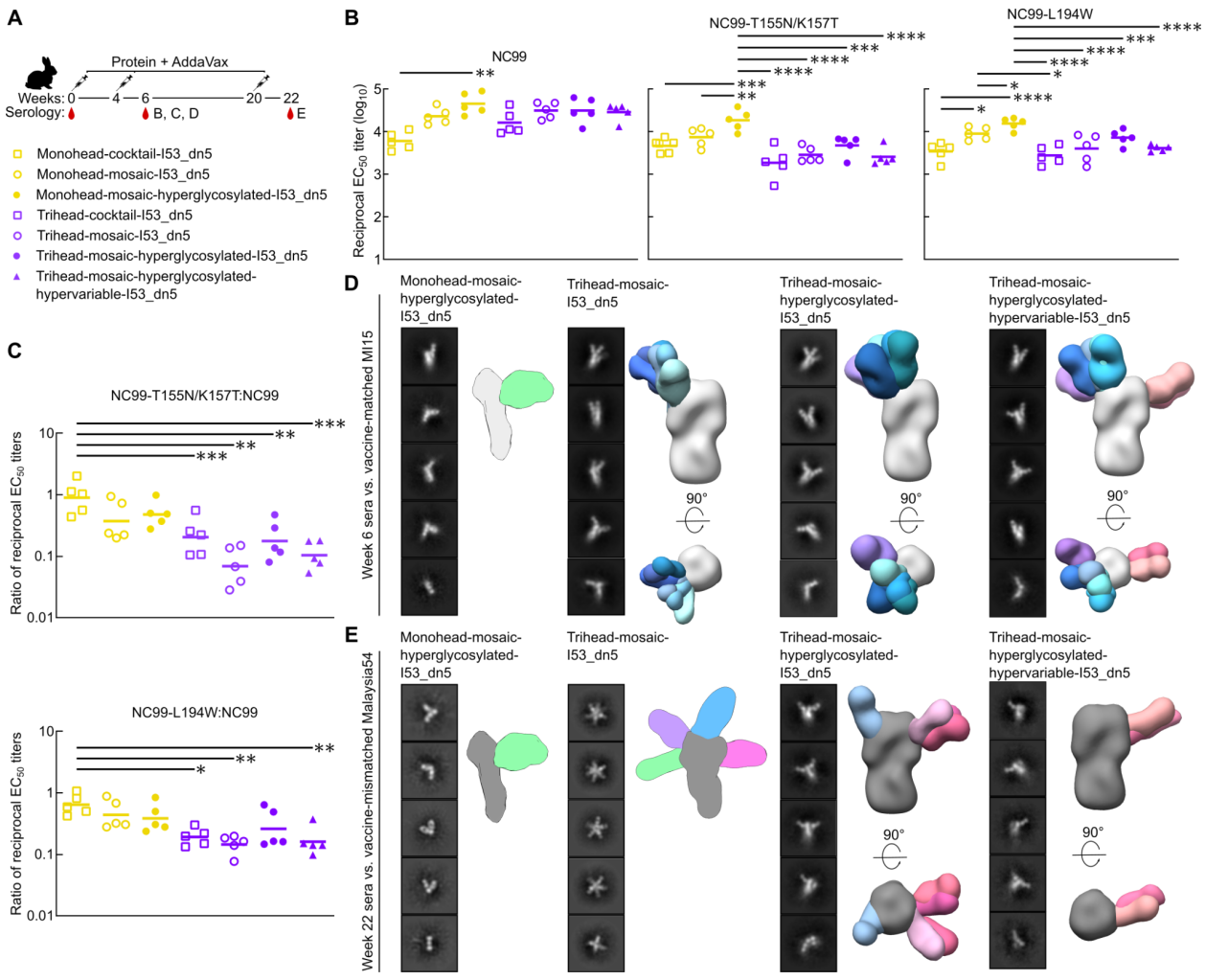

Figure 1.5 Epitope Mapping of Vaccine-elicited Antibody Responses

(A) Hypervariable trihead nanoparticle rabbit immunization schedule and groups.

(B) ELISAs using NC99 probes against week 6 rabbit study serum. NC99 ELISA is the same as in Figure 4B.

(C) Ratio of NC99 probes to NC99 binding titers in panel B.

(D) Representative 2D class averages of week 6 serum from four groups in rabbit study against strain-matched MI15. Hyperglycosylated monohead group has a cartoon schematic of a likely 3D model, while all other groups are composite 3D models of ns-EMPEM analysis.

(E) Representative 2D class averages of week 22 serum from four groups in rabbit study against strain-mismatched Malaysia54. Hyperglycosylated monohead and mosaic trihead groups have a cartoon schematic of their likely 3D models, while other groups are composite 3D models of ns-EMPEM analysis.

Statistical significance was determined using one-way ANOVA with Tukey's multiple comparisons test; ∗p < 0.05; ∗∗p < 0.01; ∗∗∗p < 0.001; ∗∗∗∗p < 0.0001.

1.2 Discussion

Here we show that the initial NC99 trihead design strategy described in the accompanying manuscript (Ellis et al., n.d.) can be applied to several divergent H1 HAs, and that these trihead mutations improve the potency and breadth of vaccine-elicited antibody responses.

Portability—the applicability of design approaches or specific mutations to antigens from diverse

pathogen strains or isolates—is an important criterion in antigen design that has led to the generation of a number of promising antigen platforms. For example, “stabilized-stem” antigens based on influenza HA were made for both group 1 and 2 HAs, and when displayed on ferritin nanoparticle immunogens they elicited cross-group protection in multiple animals models (Yassine et al. 2015; Corbett et al. 2019; Moin et al. 2022). We recently reported the stabilization of the closed tetrameric state of several different influenza neuraminidases, using an approach that was largely inspired by homology-guided mutations (Ellis et al. 2022). For several class I fusion glycoproteins, strategic use of proline mutations to stabilize the prefusion conformation (or destabilize the postfusion conformation) has proven to be a widely applicable design strategy (Sanders and Moore 2021). Proline mutations have been key in the generation of antigens that elicit potent neutralizing antibody responses against several viruses including HIV (Sanders et al. 2013, 2015) and RSV (Krarup et al. 2015), and provided an antigen platform that enabled rapid pandemic response vaccines against SARS-CoV-2 (Pallesen et al. 2017; Hsieh et al. 2020; Wrapp et al. 2020). The portability and improved immunogenicity we report here and in the accompanying manuscript (Ellis et al., n.d.) establish triheads as a promising new antigen platform for influenza vaccine design.

The higher HAI and neutralizing antibody responses we obtained with hyperglycosylated antigens are consistent with previous studies that have established hyperglycosylation as an effective antigen design strategy, while also raising mechanistic questions that motivate further studies. Our detailed antigenic characterization clearly revealed that several epitopes were successfully masked by the additional glycans in our hyperglycosylated immunogens, reducing the overall peptidic surface that can be targeted by antibodies. Nevertheless, in our rabbit study the hyperglycosylated monohead immunogen elicited higher binding titers across various H1 strains than either non-hyperglycosylated monohead immunogen (i.e., cocktail or mosaic). Though we did not asses glycan composition, a possible explanation for this discrepancy is that the potential presence of high-mannose glycans in the hyperglycosylated immunogens may drive better antigen trafficking to lymph nodes and B cell follicles, as demonstrated in recent studies from the Irvine lab (Read et al. 2022; Tokatlian et al. 2019). This effect could result in overall increases in the magnitude or quality of the vaccine-elicited antibody response that are independent of any potential redirection of vaccine-elicited antibody responses to target epitopes due to glycan masking. It is likewise possible that the hyperglycosylated immunogens are less susceptible to proteolytic degradation *in vivo*, which could also increase immunogenicity overall (Cirelli et al. 2019; Aung et al. 2023). These potential mechanisms are also consistent with the antibody responses elicited by our hyperglycosylated and non-hyperglycosylated trihead immunogens, where the former elicited higher HAI and neutralizing activity despite effectively no changes in binding antibody titers. It therefore appears that hyperglycosylation “focused” the antibody response on target epitopes near the receptor binding site. Several previous studies have shown that hyperglycosylation tends to increase the proportion—but not the overall magnitude—of on-target antibodies (Duan et al. 2018; Bajic et al. 2019). In fact, overall vaccine-elicited antibody titers can be reduced by epitope masking (Weidenbacher and Kim 2019). One potential explanation for our observation of clear increases in HAI and neutralizing activity may be an increase in overall immunogenicity accompanied by a reduction in off-target antibody responses. Glycan-dependent effects on trafficking and stability

may account for the former, while the epitope masking provided by the glycans could account for the latter. Our EMPEM data in aggregate support suppression of non-RBS responses by hyperglycosylation, with the caveat related to under-occupancy at position 171 of the hyperglycosylated NC99 trihead as noted above. In summary, we observed a focusing-like effect from our hyperglycosylated trihead immunogens, but which of several potential mechanisms was primarily responsible remains to be determined. Future studies on the contributions of various mechanisms to the overall response will benefit from the use of systematic series of immunogens like those described here, in the accompanying manuscript (Ellis et al., n.d.), and in previous work (Read et al. 2022; Kato et al. 2020; Abbott et al. 2018).

In contrast to trihead closure and hyperglycosylation, the effects of mosaic nanoparticle display and hypervariable antigen design were less clear in our experiments. In the first study of mosaic nanoparticle immunogens, a significant advantage in eliciting cross-reactive B cell responses was observed when presenting HA RBDs on ferritin nanoparticles in a mosaic array compared to either a cocktail or sequential immunization regimen (Kanekiyo et al. 2019). In this work, we observed more strain-specificity in vaccine-matched responses elicited by the monohead cocktail group compared to the monohead mosaic group. However, we did not observe any significant differences between other cocktail vs. mosaic comparisons for either monohead and trihead immunogens. The addition of the hypervariable RBS periphery also did not show any significant differences compared to the hyperglycosylated trihead group. There are several differences between this study and that of Kanekiyo and colleagues that could account for why mosaics were only superior in the latter, including animal model, HA strain compositions, nanoparticle size and valency, T cell epitope content, monomeric RBDs vs. trihead antigens, and flexible vs. rigid attachment to the nanoparticle scaffold. One noticeable similarity between the two studies is that the cross-neutralizing responses we observed seem to derive from antibodies directed against the side of the HA head that bind an epitope similar to that of 441D6 (Kanekiyo et al. 2019). Although it is likely that glycan under-occupancy at this site is partially responsible, it is intriguing to speculate that BCR cross-linking by mosaic nanoparticles could explain the boost in relatively rare cross-reactive antibodies against this epitope in both studies. Additional studies that more rigorously characterize this epitope on the side of the head and the antibody responses elicited against it could inform future vaccine design efforts.

In conclusion, we have shown that trihead nanoparticle immunogens are a promising platform for next-generation influenza vaccine design. Furthermore, our evaluation of multiple layers of immune focusing techniques provides a roadmap for efforts using this and other antigen platforms to develop safe and effective vaccines against a wide variety of pathogens.

1.3 Methods

Gene Expression and Protein Purification

All HA constructs used in this study were codon-optimized for human cell expression and made in the CMV/R vector by Genscript with a C-terminal hexahistidine affinity tag. PEI MAX was used for transient transfection of HEK293F cells. After four days, mammalian cell supernatants were clarified via centrifugation and filtration. Monohead and trihead components and HA foldons were all purified using IMAC. 1 mL of Ni^{2+}-sepharose Excel or Talon resin was added

per 100 mL clarified supernatant along with 5 mL of 1 M Tris, pH 8.0 and 7 mL of 5 M NaCl and left to batch bind while shaking at room temperature for 30 min. Resin was then collected in a gravity column, washed with 5 column volumes of 50 mM Tris, pH 8.0, 500 mM NaCl, 20 mM imidazole, and protein was eluted using 50 mM Tris, pH 8.0, 500 mM NaCl, 300 mM imidazole. Further component purification was done using SEC on a Superdex 200 Increase 10/300 gel filtration column equilibrated in 25 mM Tris, pH 8.0, 150 mM NaCl, 5% glycerol. HA-ferritin nanoparticles used in HAI assays were purified as described previously (Kanekiyo et al. 2013).

Expression and purification of the I53_dn5A pentamer component from *E. coli* was carried out as previously described (Boyoglu-Barnum et al. 2021). Assembly of trihead-I53_dn5 nanoparticles was carried out by mixing purified HA trihead-I53_dn5B and pentameric I53_dn5A components together *in vitro* at a 1:1 molar ratio at 15-40 μM final concentrations. Nanoparticles were left to assemble for 30 min at room temperature with rocking. Nanoparticles were then purified using SEC on a Superose 6 Increase 10/300 gel filtration column equilibrated in 25 mM Tris, pH 8.0, 150 mM NaCl, 5% glycerol.

Following purification, nanoparticle quality and concentration was first measured by UV-vis spectroscopy. Nanoparticle polydispersity and purity was then assessed using SDS-PAGE, DLS, and nsEM. Finally, endotoxin levels were measured using the LAL assay, with all immunogens used in animal studies containing less than 100 EU/mg in the final dose. Final immunogens were flash-frozen using liquid nitrogen and stored at -80°C.

Bio-layer Interferometry (BLI)

BLI was carried out using an Octet Red 96 system, at 25°C with 1000 rpm shaking. Anti-HA antibodies were diluted in kinetics buffer (PBS with 0.5% serum bovine albumin and 0.01% Tween) to a final concentration of 10 μg/mL before loading onto protein A biosensors (Sartorius) for 200 s. Monohead and trihead components were diluted to 500 nM in kinetics buffer and their association was measured for 200 s, followed by dissociation for 200 s in kinetics buffer alone.

Sandwich BLI

AR2G biosensors (Sartorius) were first activated by the addition of freshly mixed 20 mM 1-Ethyl-3-(3-dimethylaminopropyl)carbodiimide and 10 mM Sulfo-N-hydroxysulfosuccinimide. C05 mAb at 5 μg/mL in 10 mM acetate buffer, pH 5.0 was then loaded, followed by quenching with 1 M ethanolamine, pH 8.5. Nanoparticles at 30 μg/mL in kinetics buffer (PBS with 0.5% serum bovine albumin and 0.01% Tween) were then loaded, followed by a baseline step in kinetics buffer before subsequent association and dissociation of anti-PR34 and then 5J8, both at 50 nM in kinetics buffer.

Negative Stain Electron Microscopy

3.5 μl of 70 μg/mL nanoparticles were applied to glow-discharged 400-mesh carbon-coated grids (Electron Microscopy Sciences) and stained with 2% (wt/vol) uranyl formate. Data were collected using EPU 2.0 on a 120 kV Talos L120C transmission electron microscope (Thermo Scientific) with a BM-Ceta camera. CryoSPARC (Punjani et al. 2017) was used for CTF correction, particle picking and extraction, and 2D classification.

Dynamic Light Scattering
DLS was carried out on an UNcle (UNchained Labs) at 25°C. 10 acquisitions of 5 sec each were acquired for each spectrum. Protein concentration (ranging from 0.1-1 mg/mL) and buffer conditions were accounted for in the software.

Glycan Occupancy Quantitation
Glycan occupancy quantitation was performed using peptide mass spectrometry to determine the relative abundance of peptides in the non-glycosylated and de-glycosylated states after full deglycosylation using N-glycanase (Stavenhagen et al. 2013). Each construct was combined with guanidine hydrochloride and DTT (6 M and 20 mM final concentration, respectively) and boiled for 30 minutes. Cysteines were then alkylated with the addition of 40 mM iodoacetamide and incubated in the dark for 1 hour and quenched with another addition of 20 mM DTT. Samples were diluted 6-fold in 10 mM Tris pH 8.0, 1 mM $CaCl_2$ and treated with N-glycanase (New England Biolabs) for 1 hour at 37°C.

The samples were then split into two and treated with either LysC or GluC proteases (ThermoScientific, 1:20 protease:substrate molar ratio) overnight at 37°C. Digestions were quenched with the addition of 0.25% formic acid. Peptides were trapped and desalted using C18 spin columns (ThermoScientific) using the manufacturer's suggested protocol and dried by speedvac. Purified peptides were resuspended in 20 µL of 0.1% formic acid. LC-MS analysis was performed on an Thermo EASYnLC coupled to a Thermo Orbitrap Fusion operating in data-dependent mode using EThcD fragmentation. Peptides were resolved over a pulled 30 µm ID silica tip packed with Reprosil-Pur 120 C18-AQ, 5 µm (ESI Source Solutions) using a linear gradient of 5-30%B (A: 0.1% formic acid; B: acetonitrile with 0.1% formic acid) over 90 minutes at a flowrate of 300 nL/min. LC-MS data were analyzed with Byonic (Protein Metrics Inc.) with a score cutoff of 100 and quantitative analysis was performed using Skyline (Pino et al. 2020).

Circular Dichroism
CD measurements were carried out on a JASCO J1500 spectrometer at 25°C, using 1 mm path-length cuvette, at wavelengths from 200-260 nm. Proteins were measured at 0.2-0.3 mg/ml in TBS buffer.

Hydrogen Deuterium Exchange Mass Spectrometry
40 pmol of each protein per timepoint were incubated in deuterated buffer (20 mM PBS, 85% D2O, pH∗ 7.48) for 3 s, 1 min, 30 min, and 22 hrs at room temperature (23°C). The reaction was stopped by diluting 1:1 in ice-cold quench buffer (200 mM tris(2-chlorethyl) phosphate (TCEP), 4 M urea, 0.2% formic acid) to a final pH of 2.495. Samples were immediately flash frozen in liquid nitrogen and stored at −80°C prior to analysis. As previously described, online nepenthesin-2 (Nepenthesin-2 protease column, 2.1 x 20 mm, purchased from POROS) digestion was performed and analyzed by LC-MS-IMS utilizing a Waters ACQUITY UPLC CSH C18 VanGuard column (130 Å, 1.7 µm, 1mm x 100 mm) and a Waters Synapt G2-Si Q-TOF mass spectrometer (Verkerke et al. 2016). A custom HDX cold box maintained the protease digestion at 4°C and the LC plumbing at 0°C throughout the 15 minute gradient (Watson et al. 2021). Waters MSe

data was collected on the Waters Synapt G2-Si Q-TOF and was processed using Byonic (Version 3.8, Protein Metrics Inc.) to obtain a peptide reference list for each construct. Some homologous peptides were determined by aligning sequences using Clustal-Omega and calculating theoretical monoisotopic m/z values using ExPASy PeptideMass. Percent exchange values were calculated with theoretical total deuteration profiles produced by HD-Examiner (version 3.3, Seirra Analytics). An internal exchange standard (Pro-Pro-Pro-Ile [PPPI]) was included in each reaction to control for variations in ambient temperature during the labeling reactions. Data for each timepoint was collected in duplicate and error bars were plotted using one standard deviation. Back-exchange was determined by comparing experimental totally deuterated spectra to theoretical totally deuterated spectra. The average back exchange across all peptides was determined to be 31.6%. TH-NC99-9gly data was collected separately from the rest of the triheads and at a higher cone voltage (150 V) which reduced peptide signal at higher charge states (3+, 4+). To control for increases in back exchange from the higher cone voltage, a 3s and 1m control (TH-SC18-RBS2) was run at both voltages (40V and 150V) producing an average difference of 2.6% which is smaller than the differences we observe in the data.

NanoDSF

All proteins were formulated at 0.5 mg/mL in 25 mM Tris, pH 8.0, 150 mM NaCl, 5% glycerol and then mixed at 9 volumes to 1 volume of 200× concentrate SYPRO orange (Thermo Fisher) diluted in the same buffer. NanoDSF to determine melting temperatures was carried out on an UNcle (UNchained Labs) by measuring the barycentric mean of the fluorescence emission spectrum during a thermal ramp from 25°C to 95°C, with a 1°C increase in temperature per minute.

HA Sequence Conservation Plot

643 unique H1 HA sequences were downloaded from the Influenza Research Database (https://legacy.fludb.org/). Sequence conservation amongst these was then plotted on HA using PyMOL
(The PyMOL Molecular Graphics System, Version 2.0, Schrödinger, LCC).

Immunization

Female BALB/c mice (Jackson Laboratories) were immunized intramuscularly with 1.5 µg purified nanoparticle immunogen in 100 µl (50 µl in each hind leg) of 50% (v/v) mixture of AddaVax adjuvant (Invivogen, San Diego, CA) (**Figure 1 and S1)**. For sera collection, mice were bled via submental venous puncture 2 weeks following each inoculation. Serum was isolated from hematocrit via centrifugation at 2,000 g for 10 min, and stored at -80°C until use. Female New Zealand white rabbits weighing approximately 4 kg were immunized intramuscularly with 25 µg purified nanoparticle immunogen in 1 ml (500 µl in each quadricep) of 50% (v/v) mixture of AddaVax adjuvant (**Figure 4, 5 and S7**).

ELISA

HA-foldon trimers were added to 96-well Nunc MaxiSorp plates (Thermo Scientific) at 5.0 µg/mL with 50 µL per well and incubated for 1 hour. Blocking buffer composed of Tris Buffered Saline Tween (TBST: 25 mM Tris pH 8.0, 150 mM NaCl, 0.05% (v/v) Tween20) with 5% Nonfat milk

was then added at 200 µl per well and incubated for 1 hour. Next plates were washed, with all washing steps consisting of 3x washing with TBST using a robotic plate washer (Biotek). 5-fold serial dilutions of serum starting at 1:100 were made in blocking buffer, added to plates at 50 µl per well, and incubated for 1 hour. Plates were washed again before addition of 50 µl per well of either anti-mouse or anti-rabbit HRP-conjugated goat secondary antibody (CellSignaling Technology) diluted 1:2,000 in blocking buffer and incubated for 30 minutes. All incubations were carried out with shaking at room temperature. Plates were washed a final time, and then 100 µl per well of TMB (3,3′,5′,5-tetramethylbenzidine, SeraCare) was added for 2 minutes, followed by quenching with 100 µl per well of 1 N HCl. Reading at 450 nm absorbance was done on an Epoch plate reader (BioTek).

Competition ELISA

Competition ELISAs were performed in the same manner as the above ELISA protocol with some modifications as follows. For competition with FluA-20, 5-fold serial serum dilutions were made starting at 1:10, and for competition with C05, 3-fold serial serum dilutions were made starting at 1:5. Serum was left to incubate for 30 minutes, followed by addition of 50 µl of 0.1 µg/ml competitor antibody in blocking buffer and incubation for 45 minutes. After washing, anti-human HRP-conjugated goat secondary antibody (Southern Biotech) was added at 20,000x at 50 µl per well and incubated for 30 minutes.

HAI

Serum was inactivated using receptor-destroying enzyme (RDE) II (Seiken) in PBS at a 3:1 ratio of RDE to serum for 16 hours at 37°C, followed by 40 minutes at 56°C. Inactivated serum was serially diluted 2-fold in PBS in V-bottom plates at 25 µl per well. 25 µl HA-ferritin nanoparticles at 4 hemagglutinating units were then added to all wells and incubated at room temperature for 30 min (Whittle et al. 2014). Lastly, 50 µl of 10-fold diluted turkey red blood cells (Lampire) in PBS was added to each well. Hemagglutination was left to proceed for at least 1 hour before recording HAI titer.

Reporter-based microneutralization assay

Influenza A reporter viruses were made as previously described (Creanga et al. 2021). Briefly, H1N1 viruses were made with a modified PB1 segment expressing the TdKatushka reporter gene (R3ΔPB1), rescued, and propagated in MDCK-SIAT-PB1 cells in the presence of TPCK-treated trypsin (1 µg ml−1, Sigma) at 37 °C. Virus stocks were stored at −80 °C and were titrated before use in the assay. Rabbit sera was treated with receptor destroying enzyme (RDE II; Denka Seiken) and heat-inactivated before use in neutralization assays. 384 well plates (Greiner) were pre-seeded with 1.0 × 10^5 MDCK-SIAT1-PB1 cells and incubated overnight. Immune sera or monoclonal antibody controls (CR8071 and CR9114 (Dreyfus et al. 2012)) were serially diluted and incubated for 1 h at 37 °C with pre-titrated virus (A/Fort Monmouth/1/1947, A/Malaysia/302/1954, A/New Caledonia/20/1999, A/USSR/90/1977, A/Solomon Islands/3/2006, A/Michigan/45/2015). Serum-virus mixtures were then transferred in quadruplicate onto the pre-seeded 384 well plates and incubated at 37 °C for 18-26 hours. The number of fluorescent cells in each well was counted automatically using a Celigo image cytometer (Nexcelom Biosciences). IC50 values, defined as the serum dilution or antibody concentration that gives

50% reduction in virus-infected cells, were calculated from neutralization curves using a four-parameter nonlinear regression model.

EMPEM

1 mL rabbit serum was diluted 3x in PBS and incubated overnight with 1 ml packed rProtein A Sepharose Fast Flow resin (Cytiva). The FT was removed using gravity purification and resin was washed with 20 CVs PBS. IgGs were eluted by incubating resin for 20 min with 1 CV of 0.1 M glycine, pH 2.5, repeated twice. Elutions were neutralized with 1 M Tris, pH 8.0 to a final concentration of 50 mM. IgGs were then buffer exchanged into PBS and concentrated to 250 µl for digestion into fabs. Fab digestion was carried out by adding in 250 µl freshly made 2x digestion buffer (40 mM $NaPO_4$ pH 6.5, 20 mM EDTA, 40 mM Cysteine) and 500 µl papain resin in 500 µl 1x digestion buffer, and incubated with shaking at 37°C for 16 hours. Papain digestion reaction was centrifuged and supernatant containing fabs was collected and filtered. Papain was subsequently washed with 1 CV 20 mM Tris, pH 8.0 and this supernatant was added to the first. Digested sera was then purified by SEC on a Superdex 200 Increase 10/300 GL column. Purified fabs were then concentrated to 50 µl, mixed with 50-fold molar excess of HA-foldon trimers, and incubated for 16-20 hours at room temperature with gentle rocking. Immune complexes were purified by SEC on a Superdex 200 Increase 10/300 GL column and used in EM.

Supplementary Figures

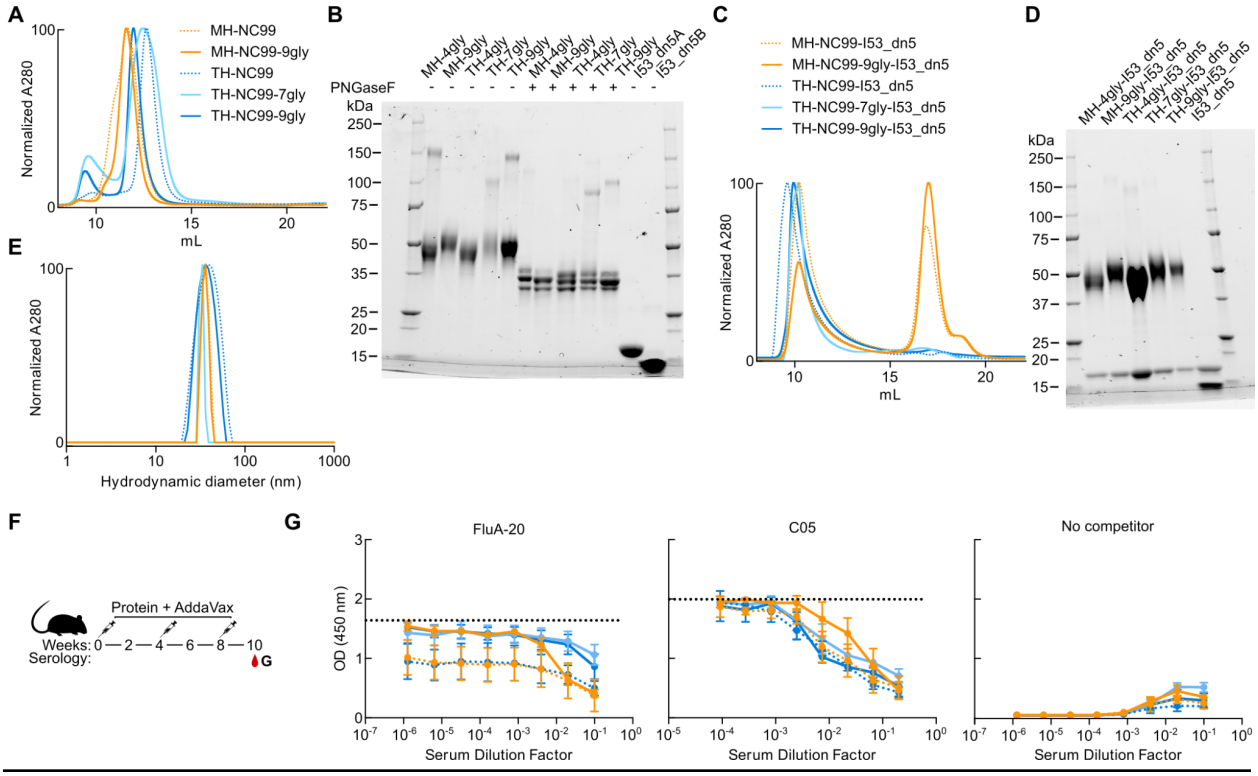

Figure S1.1 Hyperglycosylated TH-NC99-I53_dn5 Mouse Study

(A) SEC chromatograms of NC99 trihead nanoparticle components on a Superdex 200 Increase 10/300 GL column.

(B) Reducing SDS-PAGE of wild-type and hyperglycosylated NC99 monoheads and trihead components without and with PNGaseF digestion, as well as bare I53_dn5B and I53_dn5A nanoparticle components.

(C) NC99 trihead-I53_dn5 nanoparticle legend for Figures S1B, S1D, and S1F. SEC chromatograms of NC99 trihead-I53_dn5 nanoparticle immunogens on a Superose 6 Increase 10/300 GL column.

(D) Reducing SDS-PAGE of NC99 trihead-I53_dn5 nanoparticles, as well as the bare I53_dn5 nanoparticle.

(E) DLS of NC99 trihead-I53_dn5 nanoparticles.

(F) Schematic illustrating mouse study timeline, immunizations, and serology timepoint.

(G) Competition ELISA curves for NC99-foldon trimer ELISA antigen between week 10 sera and either FluA-20, C05, or a no competitor negative control. Dashed line is positive control of monoclonal binding in absence of sera.

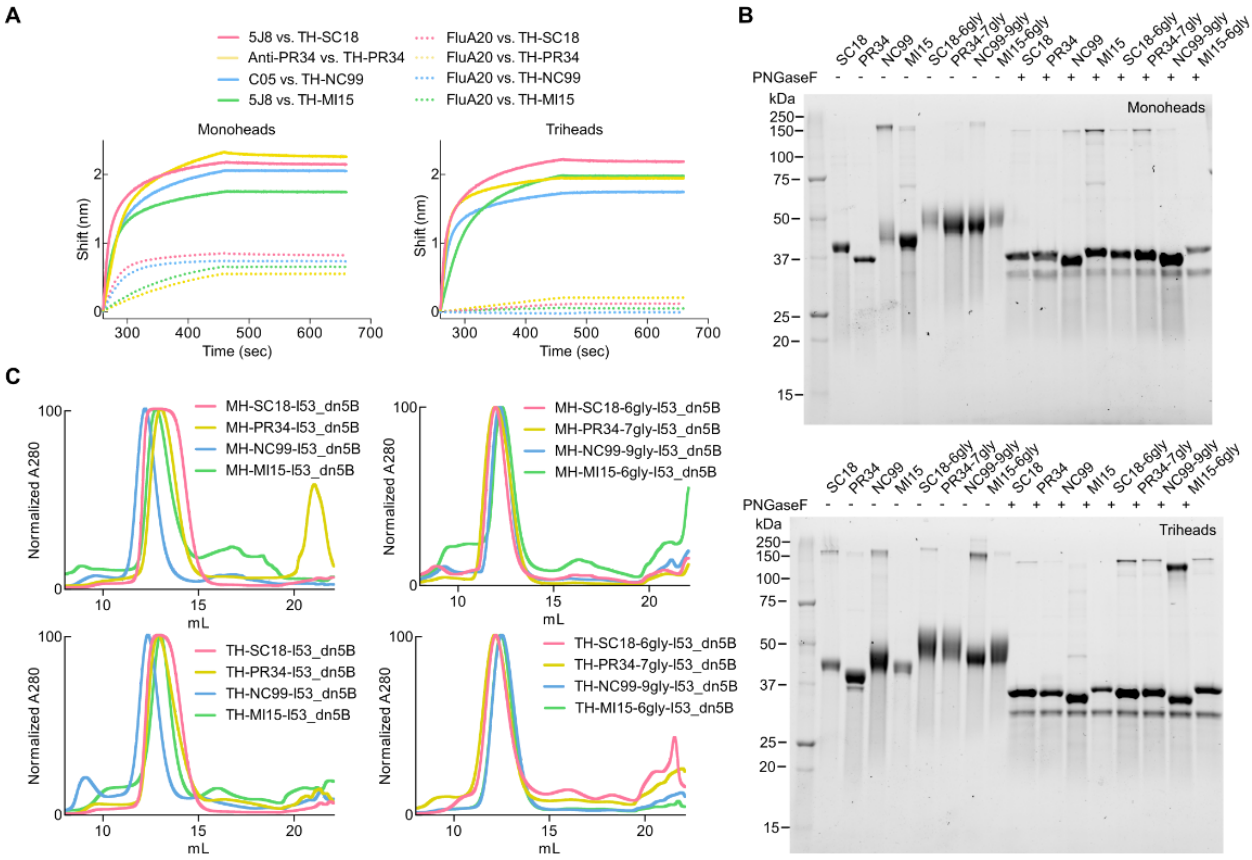

Figure S1.2 Mosaic and Hyperglycosylated Trihead Components Purification and Characterization
(A) BLI of monohead and trihead nanoparticle components against RBS-directed mAbs (5J8, anti-PR34, and C05) and FluA-20.
(B) Reducing SDS-PAGE of wild-type and hyperglycosylated monohead and trihead nanoparticle components without and with PNGaseF digestion.
(C) SEC chromatograms of wild-type and hyperglycosylated monohead and trihead nanoparticle components on a Superdex 200 Increase 10/300 GL column.

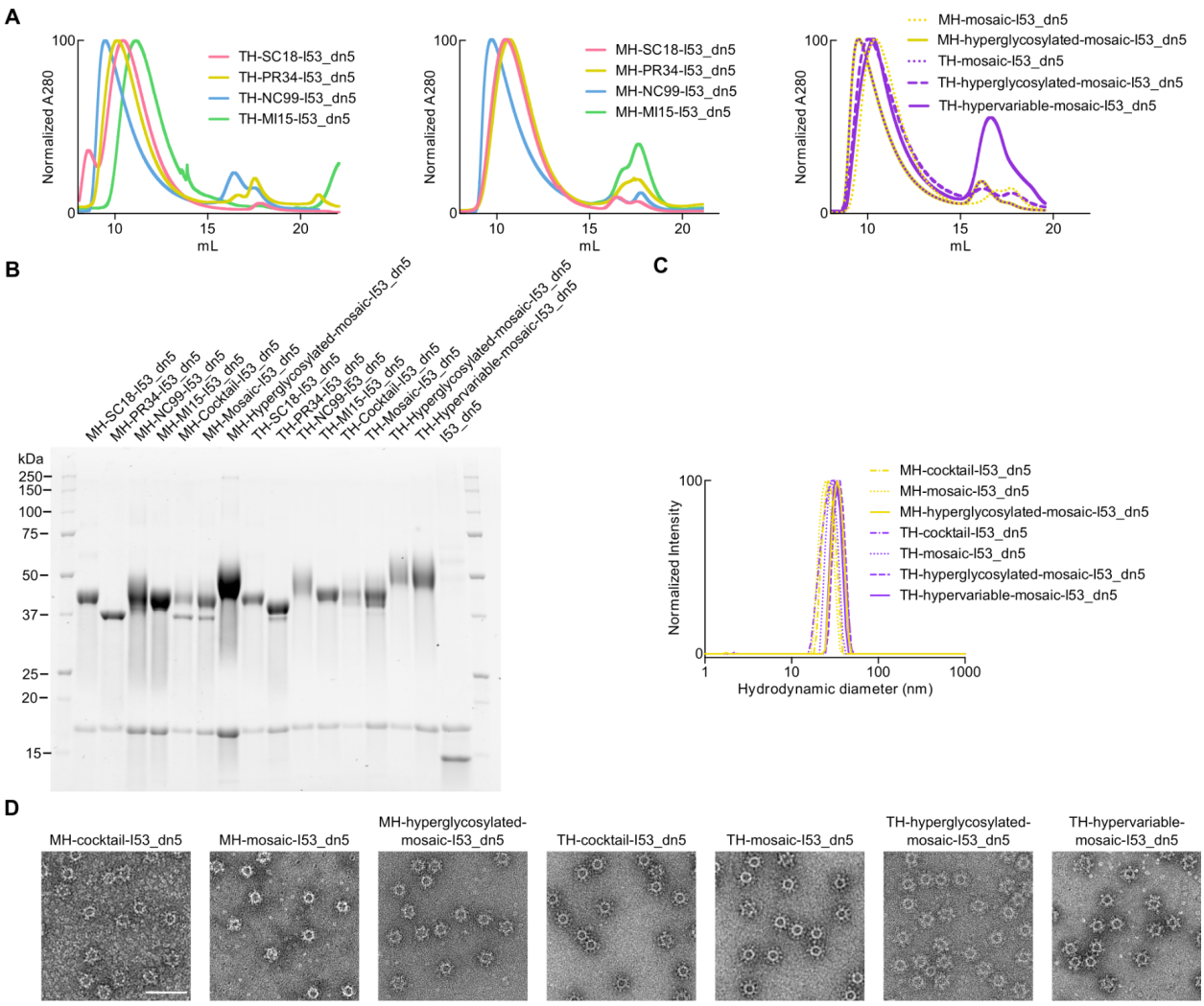

Figure S1.3 Mosaic, Hyperglycosylated, and Hypervariable Trihead Nanoparticles Purification and Characterization

(A) SEC chromatograms of individual H1 strains of monohead- and trihead-I53_dn5 nanoparticles and all mosaic nanoparticles on a Superose 6 Increase 10/300 GL column.

(B) Reducing SDS-PAGE of individual H1 strains of monohead- and trihead-I53_dn5 nanoparticles and all mosaic nanoparticles, as well as the bare I53_dn5 nanoparticle.

(C-D) C. DLS and D. nsEM of all mosaic nanoparticles. Scale bar = 100 nm.

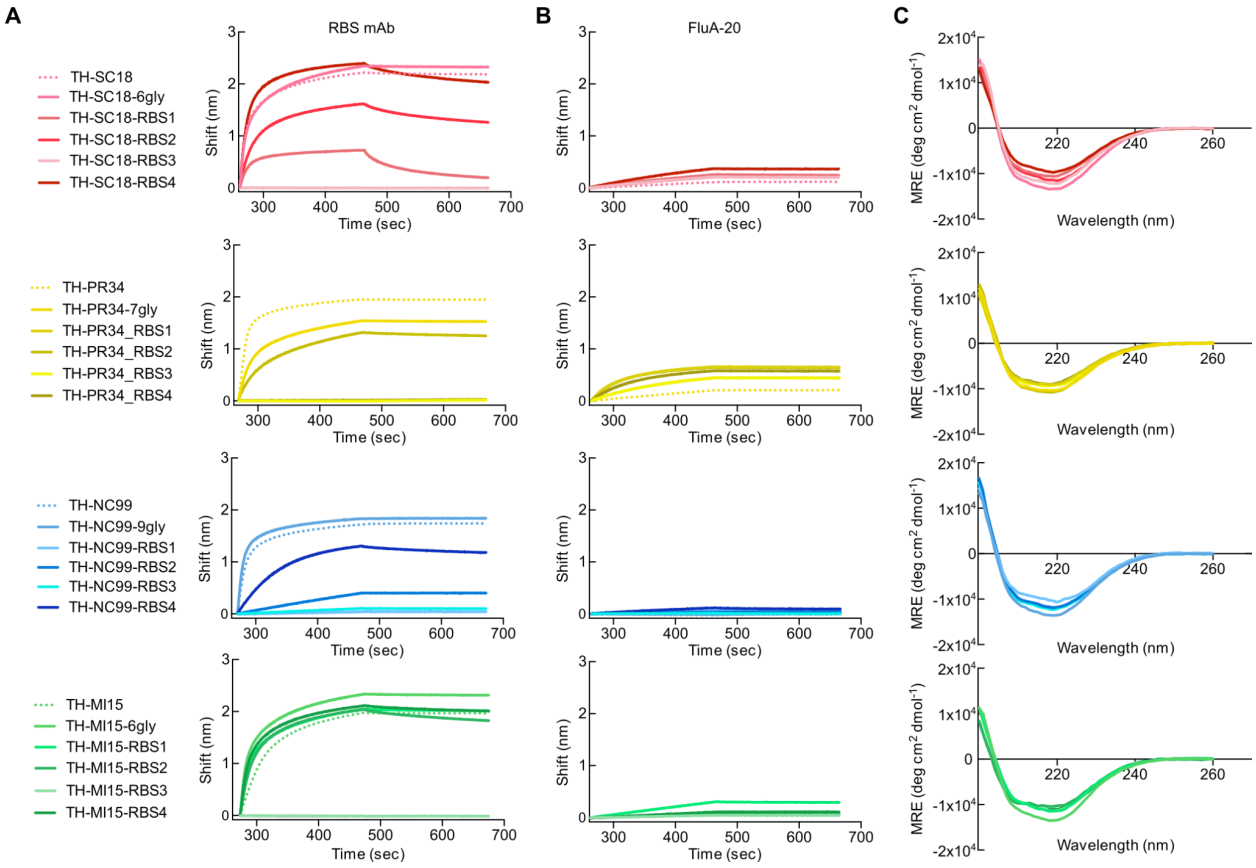

Figure S1.4 Hypervariable Trihead Immunogen Biophysical Characterization

(A) Legend of constructs in panels A-C. Binding of RBS-directed mAbs to all trihead components.

(B) FluA-20 binding to all trihead components.

(C) Far-UV circular dichroism (CD) spectra of all hypervariable trihead components.

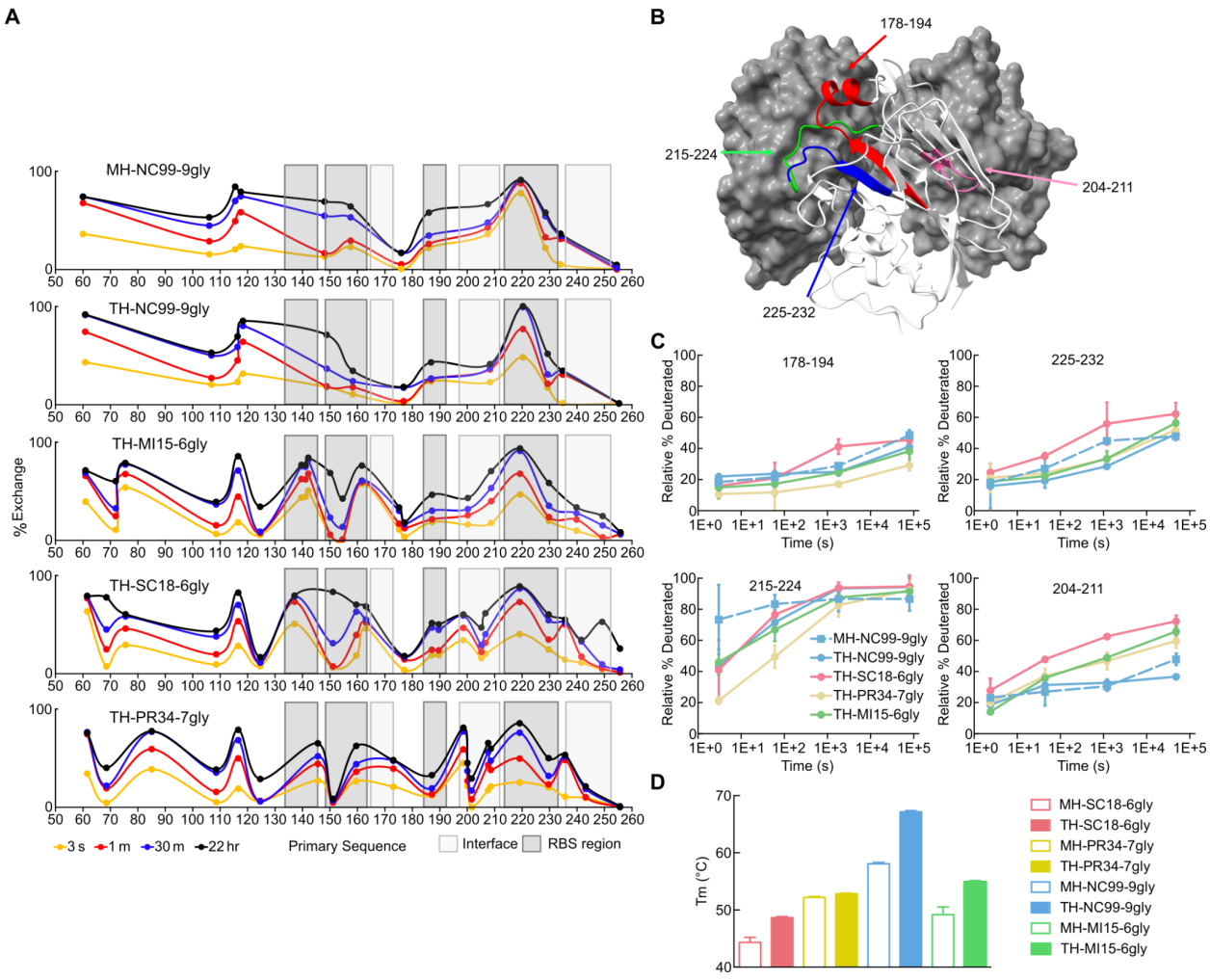

Figure S1.5 Hyperglycosylated Trihead Stability Characterization by HDX and Thermal Melts
(A) Deuterium uptake profiles across primary sequence plotted at four different timepoints for each construct.
(B) HDX peptides in panel B highlighted by color on the SI06 (PDB: 5UG0) HA head domain.
(C) Percent deuteration over time for two peptides in the RBS (178-194 and 225-232) and two peptides in the head trimer interface (215-224 and 204-211).
(D) Melting temperatures of hyperglycosylated monoheads and triheads.

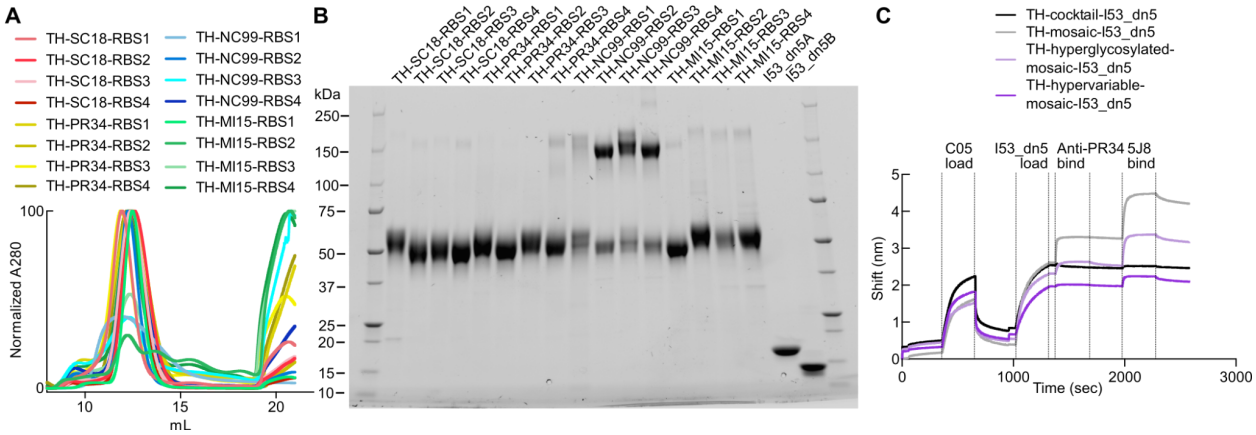

Figure S1.6 Hypervariable Trihead Immunogen Purification and Mosaic Nanoparticles BLI

(A) SEC chromatograms of hypervariable trihead nanoparticle components on a Superdex 200 Increase 10/300 GL column.

(B) Reducing SDS-PAGE of hypervariable trihead-I53_dn5 nanoparticle components, as well as bare I53_dn5B and I53_dn5A nanoparticle components.

(C) Sandwich BLI of trihead nanoparticle immunogens with C05 first captured on AR2G biosensors and then subsequent binding of nanoparticles, anti-PR34, and 5J8.

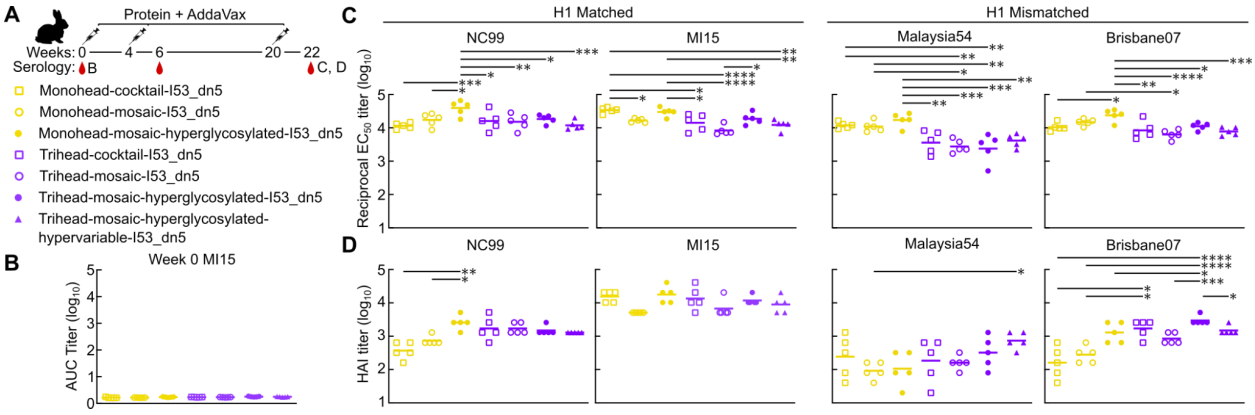

Figure S1.7 Vaccine-elicited Antibody Responses at Weeks 0 and 22 in Rabbits Immunized with Monohead and Trihead Nanoparticles

(A). Hypervariable trihead nanoparticle rabbit immunization schedule and groups.

(B) ELISA AUC titers against vaccine-matched MI15 at week 0.

(C-D) C. ELISA reciprocal EC_{50} titers and D. HAI titers at week 22, two weeks post second boost. Statistical significance was determined using one-way ANOVA with Tukey's multiple comparisons test; ∗p < 0.05; ∗∗p < 0.01; ∗∗∗p < 0.001; ∗∗∗∗p < 0.0001.

Table S1.1 Amino acid sequences of novel proteins used in this study

2heptad Monoheads

>MH-NC99
MDSKGSSQKGSRLLLLLVVSNLLLPQGVLAIAPLQLGNCSVAGWILGNPECELLISKESWSYIVETPNPEN
GTCFPGYFADYEELREQLSSVSSFERFEIFPKESSWPNHTVTGVSASCSHNGKSSFYRNLLWLTGKNGLY
PNLSKSYVNNKEKEVLVLWGVHHPPNIGNQRALYHTENAYVSVVSSHYSRRFTPEIAKRPKVRDQEGRIN
YYWTLLEPGDTIIFEANGNLIAPWYAFALSRGFGSGSGKRIENILSKIYHIENEIAELAYLLGELAYKLGEYRIA
IRAYRIALKSDPNNAEAWYNLGNAYYKQGRYREAIEYYQKALELDPNNAEAWYNLGNAYYERGEYEEAIE
YYRKALRLDPNNADAMQNLLNAKMREEGGWELQHHHHHH

>MH-NC99-9gly
MDSKGSSQKGSRLLLLLVVSNLLLPQGVLAIAPLQLGNCSVAGWILGNPECNLSINASSWSYIVETPNPEN
GTCFPGYFADYEELREQLSSVSSFERFEIFPKNSSWPNHTVTGVSASCSHNGKSSFYRNLLWLTGKNGL
YPNLSKNYTNNKSKEVLVLWGVHHPPNIGNQRALYHTENAYVSVVSSHYSRRFTPEIAKRPKVRDQEGRI
NYYWTLLEPGDTIIFEANGNLIAPWYAFALSRGFGSGSGKRIENILSKIYHIENEIAELAYLLGELAYKLGEYR
IAIRAYRIALKSDPNNAEAWYNLGNAYYKQGRYREAIEYYQKALELDPNNAEAWYNLGNAYYERGEYEEAI
EYYRKALRLDPNNADAMQNLLNAKMREEGGWELQHHHHHH

2heptad Triheads

>TH-NC99
MDSKGSSQKGSRLLLLLVVSNLLLPQGVLAIAPLQLGNCSVAGWILGNPECELLISKESWSYIVETPNPEN
GTCFPGYFADYEELRCQLSSVSSFERFEIFPKESSWPNHTVTGVSASCSHNGKSSFYRNLLWLTGKNGL
YPNLSKSYVNNKEKEVLVLWGVHHPPNIGNQRALYHTENAYVLVVSSHYDRVFTPIIAKRPKVRDQEGRIN
YYWTLLEPGDTIIFEANGNLIAPWYAFALSRGFGSGSGSCIENINSKIYHIENEIAELAYLLGELAYKLGEYRI
AIRAYRIALKSDPNNAEAWYNLGNAYYKQGRYREAIEYYQKALELDPNNAEAWYNLGNAYYERGEYEEAI
EYYRKALRLDPNNADAMQNLLNAKMREEGGWELQHHHHHH

>TH-NC99-7gly
MDSKGSSQKGSRLLLLLVVSNLLLPQGVLAIAPLQLGNCSVAGWILGNPECELLINASSWSYIVETPNPEN
GTCFPGYFADYEELRCQLSSVSSFERFEIFPKNSSWPNHTVTGVSASCSHNGKSSFYRNLLWLTGKNGL
YPNLSKSYVNNKSKEVLVLWGVHHPPNIGNQRALYHTENAYVLVVSSHYDRVFTPIIAKRPKVRDQEGRIN
YYWTLLEPGDTIIFEANGNLIAPWYAFALSRGFGSGSGSCIENINSKIYHIENEIAELAYLLGELAYKLGEYRI
AIRAYRIALKSDPNNAEAWYNLGNAYYKQGRYREAIEYYQKALELDPNNAEAWYNLGNAYYERGEYEEAI
EYYRKALRLDPNNADAMQNLLNAKMREEGGWELQHHHHHH

>TH-NC99-9gly
MDSKGSSQKGSRLLLLLVVSNLLLPQGVLAIAPLQLGNCSVAGWILGNPECNLSINASSWSYIVETPNPEN
GTCFPGYFADYEELRCQLSSVSSFERFEIFPKNSSWPNHTVTGVSASCSHNGKSSFYRNLLWLTGKNGL
YPNLSKNYTNNKSKEVLVLWGVHHPPNIGNQRALYHTENAYVLVVSSHYDRVFTPIIAKRPKVRDQEGRIN
YYWTLLEPGDTIIFEANGNLIAPWYAFALSRGFGSGSGSCIENINSKIYHIENEIAELAYLLGELAYKLGEYRI
AIRAYRIALKSDPNNAEAWYNLGNAYYKQGRYREAIEYYQKALELDPNNAEAWYNLGNAYYERGEYEEAI
EYYRKALRLDPNNADAMQNLLNAKMREEGGWELQHHHHHH

1heptad Monoheads

>MH-SC18

MDSKGSSQKGSRLLLLLVVSNLLLPQGVLAIAPLQLGKCNIAGWLLGNPECDLLLTASSWSYIVETSNSEN
GTCYPGDFIDYEELRCQLSSVSSFEKFEIFPKTSSWPNHETTKGVTAACSYAGASSFYRNLLWLTKKGSS
YPKLSKSYVNNKGKEVLVLWGVHHPPTGTDQQSLYQNADAYVSVGSSKYNRRFTPEIAARPKVRDQAGR
MNYYWTLLEPGDTITFEATGNLIAPWYAFALNRGSGSGSGSCIEHIENEIAELAYLLGELAYKLGEYRIAIRA
YRIALKSDPNNAEAWYNLGNAYYKQGRYREAIEYYQKALELDPNNAEAWYNLGNAYYERGEYEEAIEYYR
KALRLDPNNADAMQNLLNAKMREEGGWELQHHHHHH

>MH-PR34
MDSKGSSQKGSRLLLLLVVSNLLLPQGVLAIAPLQLGKCNIAGWLLGNPECDPLLSVRSWSYIVETPNSEN
GICYPGDFIDYEELRCQLSSVSSFERFEIFPKESSWPNHNTNGVTAACSHEGKSSFYRNLLWLTEKEGSY
PKLKNSYVNKKGKEVLVLWGIHHPPNSKEQQNLYQNENAYVSVVTSNYNRRFTPEIAERPKVRDQAGRM
NYYWTLLKPGDTIIFEANGNLIAPMYAFALRRGFGSGSGSCIEHIENEIAELAYLLGELAYKLGEYRIAIRAYR
IALKSDPNNAEAWYNLGNAYYKQGRYREAIEYYQKALELDPNNAEAWYNLGNAYYERGEYEEAIEYYRKA
LRLDPNNADAMQNLLNAKMREEGGWELQHHHHHH

>MH-NC99
MDSKGSSQKGSRLLLLLVVSNLLLPQGVLAIAPLQLGNCSVAGWILGNPECELLISKESWSYIVETPNPEN
GTCFPGYFADYEELRCQLSSVSSFERFEIFPKESSWPNHTVTGVSASCSHNGKSSFYRNLLWLTGKNGL
YPNLSKSYVNNKEKEVLVLWGVHHPPNIGNQRALYHTENAYVSVVSSHYSRRFTPEIAKRPKVRDQEGRI
NYYWTLLEPGDTIIFEANGNLIAPWYAFALSRGFGSGSGSCIEHIENEIAELAYLLGELAYKLGEYRIAIRAYR
IALKSDPNNAEAWYNLGNAYYKQGRYREAIEYYQKALELDPNNAEAWYNLGNAYYERGEYEEAIEYYRKA
LRLDPNNADAMQNLLNAKMREEGGWELQHHHHHH

>MH-MI15
MDSKGSSQKGSRLLLLLVVSNLLLPQGVLAVAPLHLGKCNIAGWILGNPECESLSTASSWSYIVETSNSDN
GTCFPGDFINYEELRCQLSSVSSFERFEIFPKTSSWPNHDSNKGVTAACPHAGAKSFYKNLIWLVKKGNS
YPKLNQSYINDKGKEVLVLWGIHHPSTTADQQSLYQNADAYVFVGTSRYSKKFKPEIATRPKVRDQEGRM
NYYWTLVEPGDKITFEATGNLVVPRYAFTMERNAGSGSGSCIEHIENEIAELAYLLGELAYKLGEYRIAIRAY
RIALKSDPNNAEAWYNLGNAYYKQGRYREAIEYYQKALELDPNNAEAWYNLGNAYYERGEYEEAIEYYRK
ALRLDPNNADAMQNLLNAKMREEGGWELQHHHHHH

>MH-SC18-6gly
MDSKGSSQKGSRLLLLLVVSNLLLPQGVLAIAPLQLGNCSIAGWLLGNPECDLLLNASSWSYIVETSNSEN
GTCYPGDFIDYEELRCQLSSVSSFEKFEIFPKNSSWPNHTTTKGVTAACSYAGASSFYRNLLWLTKKGSS
YPKLSKNYTNNKGKEVLVLWGVHHPPTGTDQQSLYQNADAYVSVGSSKYNRRFTPEIAARPKVRDQAGR
MNYYWTLLEPGDTITFEATGNLIAPWYAFALNRGSGSGSGSCIEHIENEIAELAYLLGELAYKLGEYRIAIRA
YRIALKSDPNNAEAWYNLGNAYYKQGRYREAIEYYQKALELDPNNAEAWYNLGNAYYERGEYEEAIEYYR
KALRLDPNNADAMQNLLNAKMREEGGWELQHHHHHH

>MH-PR34-7gly
MDSKGSSQKGSRLLLLLVVSNLLLPQGVLAIAPLQLGNCSIAGWLLGNPECDPLLNVSSWSYIVETPNSEN
GTCYPGDFIDYEELRCQLSSVSSFERFEIFPKNSSWPNHTTNGVTAACSHEGKSSFYRNLLWLTEKEGSY
PNLTNNYTNKKGKEVLVLWGIHHPPNSKEQQNLYQNENAYVSVVTSNYNRRFTPEIAERPKVRDQAGRM
NYYWTLLKPGDTIIFEANGNLIAPMYAFALRRGFGSGSGSCIEHIENEIAELAYLLGELAYKLGEYRIAIRAYR
IALKSDPNNAEAWYNLGNAYYKQGRYREAIEYYQKALELDPNNAEAWYNLGNAYYERGEYEEAIEYYRKA
LRLDPNNADAMQNLLNAKMREEGGWELQHHHHHH

>MH-NC99-9gly

MDSKGSSQKGSRLLLLLVVSNLLLPQGVLAIAPLQLGNCSVAGWILGNPECNLSINASSWSYIVETPNPEN
GTCFPGYFADYEELRCQLSSVSSFERFEIFPKNSSWPNHTVTGVSASCSHNGKSSFYRNLLWLTGKNGL
YPNLSKNYTNNKSKEVLVLWGVHHPPNIGNQRALYHTENAYVSVVSSHYSRRFTPEIAKRPKVRDQEGRI
NYYWTLLEPGDTIIFEANGNLIAPWYAFALSRGFGSGSGSCIEHIENEIAELAYLLGELAYKLGEYRIAIRAYR
IALKSDPNNAEAWYNLGNAYYKQGRYREAIEYYQKALELDPNNAEAWYNLGNAYYERGEYEEAIEYYRKA
LRLDPNNADAMQNLLNAKMREEGGWELQHHHHHH

>MH-MI15-7gly
MDSKGSSQKGSRLLLLLVVSNLLLPQGVLAVAPLHLGNCSIAGWILGNPECESLNTSSNWSYIVETSNSDN
GTCFPGDFINYEELRCQLSSVSSFERFEIFPKNSSWPNHDSNKGVTAACPHAGAKSFYKNLIWLVKKGNS
YPKLNQSYINDKGKEVLVLWGIHHPSTTADQQSLYQNADAYVFVGTSRYSKKFKPEIATRPKVRDQEGRM
NYYWTLVEPGDKITFEATGNLVVPRYAFTMERNAGSGSGSCIEHIENEIAELAYLLGELAYKLGEYRIAIRAY
RIALKSDPNNAEAWYNLGNAYYKQGRYREAIEYYQKALELDPNNAEAWYNLGNAYYERGEYEEAIEYYRK
ALRLDPNNADAMQNLLNAKMREEGGWELQHHHHHH

1heptad Triheads

>TH-SC18
MDSKGSSQKGSRLLLLLVVSNLLLPQGVLAIAPLQLGKCNIAGWLLGNPECDLLLTASSWSYIVETSNSEN
GTCYPGDFIDYEELRCQLSSVSSFEKFEIFPKNSSWPNHETTKGVTAACSYAGASSFYRNLLWLTKKGSS
YPKLSKSYVNNKGKEVLVLWGVHHPPTGTDQQSLYQNEDAYVIVASSKYDRVFTPLIAARPKVRDQAGRM
NYYWTLLEPGDTITFEATGNLIAPWYAFALNRGSGSGSGSCIEHIENEIAELAYLLGELAYKLGEYRIAIRAY
RIALKSDPNNAEAWYNLGNAYYKQGRYREAIEYYQKALELDPNNAEAWYNLGNAYYERGEYEEAIEYYRK
ALRLDPNNADAMQNLLNAKMREEGGWELQHHHHHH

>TH-PR34
MDSKGSSQKGSRLLLLLVVSNLLLPQGVLAIAPLQLGNCSIAGWLLGNPECDPLLSVRSWSYIEETPNSEN
GICYPGDFIDYEELRCQLSSVSSFERFEIFPKESSWPNHNTNGVTAACSHEGKSSFYRNLLWLTEKEGSY
PKLKNSYVNKKGKEVLVLWGIHHPPNSKEQQNLYQNENAYVFVGTSNYDRIFTPIIAERPKVRDQAGRMN
YYWTLLKPGDTIIFEANGNLIAPMYAFALRRGFGSGSGSCIEHIENEIAELAYLLGELAYKLGEYRIAIRAYRI
ALKSDPNNAEAWYNLGNAYYKQGRYREAIEYYQKALELDPNNAEAWYNLGNAYYERGEYEEAIEYYRKA
LRLDPNNADAMQNLLNAKMREEGGWELQHHHHHH

>TH-NC99
MDSKGSSQKGSRLLLLLVVSNLLLPQGVLAIAPLQLGNCSVAGWILGNPECELLISKESWSYIVETPNPEN
GTCFPGYFADYEELRCQLSSVSSFERFEIFPKESSWPNHTVTGVSASCSHNGKSSFYRNLLWLTGKNGL
YPNLSKSYVNNKEKEVLVLWGVHHPPNIGNQRALYHTENAYVLVVSSHYDRVFTPIIAKRPKVRDQEGRIN
YYWTLLEPGDTIIFEANGNLIAPWYAFALSRGFGSGSGSCIEHIENEIAELAYLLGELAYKLGEYRIAIRAYRI
ALKSDPNNAEAWYNLGNAYYKQGRYREAIEYYQKALELDPNNAEAWYNLGNAYYERGEYEEAIEYYRKA
LRLDPNNADAMQNLLNAKMREEGGWELQHHHHHH

>TH-MI15
MDSKGSSQKGSRLLLLLVVSNLLLPQGVLAVAPLHLGKCNIAGWILGNPECESLSTASSWSYIVETSNSDN
GTCFPGNFINYEELRCQLSSVSSFERFEIFPKTSSWPNHDSNKGVTAACPHAGAKSFYKNLIWLVKKGNS
YPKLNQSYINDKGKEVLVLWGIHHPSTTADQQSLYQNEDTYVFVSTSRYDKVFKPIIATRPKVRDQEGRMN
YYWTLVEPGDKITFEATGNLVVPRYAFTMERNAGSGSGSCIEHIENEIAELAYLLGELAYKLGEYRIAIRAYRI
ALKSDPNNAEAWYNLGNAYYKQGRYREAIEYYQKALELDPNNAEAWYNLGNAYYERGEYEEAIEYYRKA
LRLDPNNADAMQNLLNAKMREEGGWELQHHHHHH

>TH-SC18-6gly
MDSKGSSQKGSRLLLLLVVSNLLLPQGVLAIAPLQLGNCSIAGWLLGNPECDLLLNASSWSYIVETSNSEN
GTCYPGDFIDYEELRCQLSSVSSFEKFEIFPKNSSWPNHTTTKGVTAACSYAGASSFYRNLLWLTKKGSS
YPKLSKNYTNNKGKEVLVLWGVHHPPTGTDQQSLYQNEDAYVIVASSKYDRVFTPLIAARPKVRDQAGRM
NYYWTLLEPGDTITFEATGNLIAPWYAFALNRGSGSGSGSCIEHIENEIAELAYLLGELAYKLGEYRIAIRAY
RIALKSDPNNAEAWYNLGNAYYKQGRYREAIEYYQKALELDPNNAEAWYNLGNAYYERGEYEEAIEYYRK
ALRLDPNNADAMQNLLNAKMREEGGWELQHHHHHH

>TH-PR34-7gly
MDSKGSSQKGSRLLLLLVVSNLLLPQGVLAIAPLQLGNCSIAGWLLGNPECDPLLNVSSWSYIEETPNSEN
GTCYPGDFIDYEELRCQLSSVSSFERFEIFPKNSSWPNHTTNGVTAACSHEGKSSFYRNLLWLTEKEGSY
PNLTNNYTNKKGKEVLVLWGIHHPPNSKEQQNLYQNENAYVFVGTSNYDRVFTPIIAERPKVRDQAGRMN
YYWTLLKPGDTIIFEANGNLIAPMYAFALRRGFGSGSGSCIEHIENEIAELAYLLGELAYKLGEYRIAIRAYRI
ALKSDPNNAEAWYNLGNAYYKQGRYREAIEYYQKALELDPNNAEAWYNLGNAYYERGEYEEAIEYYRKA
LRLDPNNADAMQNLLNAKMREEGGWELQHHHHHH

>TH-NC99-9gly
MDSKGSSQKGSRLLLLLVVSNLLLPQGVLAIAPLQLGNCSVAGWILGNPECNLSINASSWSYIVETPNPEN
GTCFPGYFADYEELRCQLSSVSSFERFEIFPKNSSWPNHTVTGVSASCSHNGKSSFYRNLLWLTGKNGL
YPNLSKNYTNNKSKEVLVLWGVHHPPNIGNQRALYHTENAYVLVVSSHYDRVFTPIIAKRPKVRDQEGRIN
YYWTLLEPGDTIIFEANGNLIAPWYAFALSRGFGSGSGSCIENINSKIYHIENEIAELAYLLGELAYKLGEYRI
AIRAYRIALKSDPNNAEAWYNLGNAYYKQGRYREAIEYYQKALELDPNNAEAWYNLGNAYYERGEYEEAI
EYYRKALRLDPNNADAMQNLLNAKMREEGGWELQHHHHHH

>TH-MI15-7gly
MDSKGSSQKGSRLLLLLVVSNLLLPQGVLAVAPLHLGNCSIAGWILGNPECESLNTSSNWSYIVETSNSDN
GTCFPGNFINYEELRCQLSSVSSFERFEIFPKNSSWPNHDSNKGVTAACPHAGAKSFYKNLIWLVKKGNS
YPKLNQSYINDKGKEVLVLWGIHHPSTTADQQSLYQNEDTYVFVSTSRYDKVFKPIIATRPKVRDQEGRMN
YYWTLVEPGDKITFEATGNLVVPRYAFTMERNAGSGSGSCIEHIENEIAELAYLLGELAYKLGEYRIAIRAYRI
ALKSDPNNAEAWYNLGNAYYKQGRYREAIEYYQKALELDPNNAEAWYNLGNAYYERGEYEEAIEYYRKA
LRLDPNNADAMQNLLNAKMREEGGWELQHHHHHH

>TH-SC18-RBS1
MDSKGSSQKGSRLLLLLVVSNLLLPQGVLAIAPLQLGNCSIAGWLLGNPECDLLLNASSWSYIVETSNSEN
GTCYPGDFIDYEELRCQLSSVSSFEKFEIFPKNSSWPNHTTTKGVTAACSYAGENSFYRNLLWLTKSGDS
YPKLSKNYTNNKGKEVLVLWGVHHPPTGADQTDLYQNEDAYVIVASSKYDRVFTPLIAARPKVRDQAGRM
NYYWTLLEPGDTITFEATGNLIAPWYAFALNRGSGSGSGSCIEHIENEIAELAYLLGELAYKLGEYRIAIRAY
RIALKSDPNNAEAWYNLGNAYYKQGRYREAIEYYQKALELDPNNAEAWYNLGNAYYERGEYEEAIEYYRK
ALRLDPNNADAMQNLLNAKMREEGGWELQHHHHHH

>TH-SC18-RBS2
MDSKGSSQKGSRLLLLLVVSNLLLPQGVLAIAPLQLGNCSIAGWLLGNPECDLLLNASSWSYIVETSNSEN
GTCYPGDFIDYEELRCQLSSVSSFEKFEIFPKNSSWPNHTTTKGVTAACSYAGMNSFYRNLLWLTKKGNS
YPKLSKNYTNNKGKEVLVLWGVHHPPTGEDQKSLYQNEDAYVIVASSKYDRVFTPLIAARPEVRDQIGRM
NYYWTLLEPGDTITFEATGNLIAPWYAFALNRGSGSGSGSCIEHIENEIAELAYLLGELAYKLGEYRIAIRAY
RIALKSDPNNAEAWYNLGNAYYKQGRYREAIEYYQKALELDPNNAEAWYNLGNAYYERGEYEEAIEYYRK
ALRLDPNNADAMQNLLNAKMREEGGWELQHHHHHH

>TH-SC18-RBS3
MDSKGSSQKGSRLLLLLVVSNLLLPQGVLAIAPLQLGNCSIAGWLLGNPECDLLLNASSWSYIVETSNSEN
GTCYPGDFIDYEELRCQLSSVSSFEKFEIFPKNSSWPNHTTTKGVTAACSYAGEDSFYRNLLWLTKKGKS
YPKLSKNYTNNKGKEVLVLWGVHHPPTGADQEDLYQNEDAYVIVASSKYDRVFTPLIAARPQVRNQIGRM
NYYWTLLEPGDTITFEATGNLIAPWYAFALNRGSGSGSGSCIEHIENEIAELAYLLGELAYKLGEYRIAIRAY
RIALKSDPNNAEAWYNLGNAYYKQGRYREAIEYYQKALELDPNNAEAWYNLGNAYYERGEYEEAIEYYRK
ALRLDPNNADAMQNLLNAKMREEGGWELQHHHHHH

>TH-SC18-RBS4
MDSKGSSQKGSRLLLLLVVSNLLLPQGVLAIAPLQLGNCSIAGWLLGNPECDLLLNASSWSYIVETSNSEN
GTCYPGDFIDYEELRCQLSSVSSFEKFEIFPKNSSWPNHTTTKGVTAACSYAGAASFYRNLLWLTKKGSS
YPKLSKNYTNNKGKEVLVLWGVHHPPTGEDQKSLYQNEDAYVIVASSKYDRVFTPLIAARPEVRNQKGRM
NYYWTLLEPGDTITFEATGNLIAPWYAFALNRGSGSGSGSCIEHIENEIAELAYLLGELAYKLGEYRIAIRAY
RIALKSDPNNAEAWYNLGNAYYKQGRYREAIEYYQKALELDPNNAEAWYNLGNAYYERGEYEEAIEYYRK
ALRLDPNNADAMQNLLNAKMREEGGWELQHHHHHH

>TH-PR34-RBS1
MDSKGSSQKGSRLLLLLVVSNLLLPQGVLAIAPLQLGNCSIAGWLLGNPECDPLLNVSSWSYIEETPNSEN
GTCYPGDFIDYEELRCQLSSVSSFERFEIFPKNSSWPNHTTNGVTAACSHEGQDSFYRNLLWLTEKEGSY
PNLTNNYTNKKGKEVLVLWGIHHPPNSSEQKNLYQNENAYVFVGTSNYDRIFTPIIAERPKVRGQHGRMN
YYWTLLKPGDTIIFEANGNLIAPMYAFALRRGFGSGSGSCIEHIENEIAELAYLLGELAYKLGEYRIAIRAYRI
ALKSDPNNAEAWYNLGNAYYKQGRYREAIEYYQKALELDPNNAEAWYNLGNAYYERGEYEEAIEYYRKA
LRLDPNNADAMQNLLNAKMREEGGWELQHHHHHH

>TH-PR34-RBS2
MDSKGSSQKGSRLLLLLVVSNLLLPQGVLAIAPLQLGNCSIAGWLLGNPECDPLLNVSSWSYIEETPNSEN
GTCYPGDFIDYEELRCQLSSVSSFERFEIFPKNSSWPNHTTNGVTAACSHEGKSSFYRNLLWLTEKQGSY
PNLTNNYTNKKGKEVLVLWGIHHPPNSEEQTALYQNENAYVFVGTSNYDRIFTPIIAERPEVRGQHGRMNY
YWTLLKPGDTIIFEANGNLIAPMYAFALRRGFGSGSGSCIEHIENEIAELAYLLGELAYKLGEYRIAIRAYRIAL
KSDPNNAEAWYNLGNAYYKQGRYREAIEYYQKALELDPNNAEAWYNLGNAYYERGEYEEAIEYYRKALR
LDPNNADAMQNLLNAKMREEGGWELQHHHHHH

>TH-PR34-RBS3
MDSKGSSQKGSRLLLLLVVSNLLLPQGVLAIAPLQLGNCSIAGWLLGNPECDPLLNVSSWSYIEETPNSEN
GTCYPGDFIDYEELRCQLSSVSSFERFEIFPKNSSWPNHTTNGVTAACSHEGKSSFYRNLLWLTEKKGSY
PNLTNNYTNKKGKEVLVLWGIHHPPNSNEQISLYQNENAYVFVGTSNYDRIFTPIIAERPKVRDQSGRMNY
YWTLLKPGDTIIFEANGNLIAPMYAFALRRGFGSGSGSCIEHIENEIAELAYLLGELAYKLGEYRIAIRAYRIAL
KSDPNNAEAWYNLGNAYYKQGRYREAIEYYQKALELDPNNAEAWYNLGNAYYERGEYEEAIEYYRKALR
LDPNNADAMQNLLNAKMREEGGWELQHHHHHH

>TH-PR34-RBS4
MDSKGSSQKGSRLLLLLVVSNLLLPQGVLAIAPLQLGNCSIAGWLLGNPECDPLLNVSSWSYIEETPNSEN
GTCYPGDFIDYEELRCQLSSVSSFERFEIFPKNSSWPNHTTNGVTAACSHEGKSSFYRNLLWLTEKEGSY
PNLTNNYTNKKGKEVLVLWGIHHPPNSKEQHDLYQNENAYVFVGTSNYDRIFTPIIAERPKVRDQAGRMN
YYWTLLKPGDTIIFEANGNLIAPMYAFALRRGFGSGSGSCIEHIENEIAELAYLLGELAYKLGEYRIAIRAYRI
ALKSDPNNAEAWYNLGNAYYKQGRYREAIEYYQKALELDPNNAEAWYNLGNAYYERGEYEEAIEYYRKA
LRLDPNNADAMQNLLNAKMREEGGWELQHHHHHH

>TH-NC99-RBS1

MDSKGSSQKGSRLLLLLVVSNLLLPQGVLAIAPLQLGNCSVAGWILGNPECNLSINASSWSYIVETPNPEN
GTCFPGYFADYEELRCQLSSVSSFERFEIFPKNSSWPNHTVTGVSASCSHNSVSSFYRNLLWLTGKNGLY
PNLSKNYTNNKSKEVLVLWGVHHPPNIENQHALYHTENAYVLVVSSHYDRVFTPIIAKRPAVRDQKGRINY
YWTLLEPGDTIIFEANGNLIAPWYAFALSRGFGSGSGSCIENINSKIYHIENEIAELAYLLGELAYKLGEYRIAI
RAYRIALKSDPNNAEAWYNLGNAYYKQGRYREAIEYYQKALELDPNNAEAWYNLGNAYYERGEYEEAIEY
YRKALRLDPNNADAMQNLLNAKMREEGGWELQHHHHHH

>TH-NC99-RBS2
MDSKGSSQKGSRLLLLLVVSNLLLPQGVLAIAPLQLGNCSVAGWILGNPECNLSINASSWSYIVETPNPEN
GTCFPGYFADYEELRCQLSSVSSFERFEIFPKNSSWPNHTVTGVSASCSHNGESSFYRNLLWLTGKGDL
YPNLSKNYTNNKSKEVLVLWGVHHPPNIQNQLNLYHTENAYVLVVSSHYDRVFTPIIAKRPVVRNQQGRIN
YYWTLLEPGDTIIFEANGNLIAPWYAFALSRGFGSGSGSCIENINSKIYHIENEIAELAYLLGELAYKLGEYRI
AIRAYRIALKSDPNNAEAWYNLGNAYYKQGRYREAIEYYQKALELDPNNAEAWYNLGNAYYERGEYEEAI
EYYRKALRLDPNNADAMQNLLNAKMREEGGWELQHHHHHH

>TH-NC99-RBS3
MDSKGSSQKGSRLLLLLVVSNLLLPQGVLAIAPLQLGNCSVAGWILGNPECNLSINASSWSYIVETPNPEN
GTCFPGYFADYEELRCQLSSVSSFERFEIFPKNSSWPNHTVTGVSASCSHNGQLSFYRNLLWLTGKSGL
YPNLSKNYTNNKSKEVLVLWGVHHPPNIGNQKALYHTENAYVLVVSSHYDRVFTPIIAKRPVVRNQQGRIN
YYWTLLEPGDTIIFEANGNLIAPWYAFALSRGFGSGSGSCIENINSKIYHIENEIAELAYLLGELAYKLGEYRI
AIRAYRIALKSDPNNAEAWYNLGNAYYKQGRYREAIEYYQKALELDPNNAEAWYNLGNAYYERGEYEEAI
EYYRKALRLDPNNADAMQNLLNAKMREEGGWELQHHHHHH

>TH-NC99-RBS4
MDSKGSSQKGSRLLLLLVVSNLLLPQGVLAIAPLQLGNCSVAGWILGNPECNLSINASSWSYIVETPNPEN
GTCFPGYFADYEELRCQLSSVSSFERFEIFPKNSSWPNHTVTGVSASCSHNGQLSFYRNLLWLTGKNGL
YPNLSKNYTNNKSKEVLVLWGVHHPPNIQNQLNLYHTENAYVLVVSSHYDRVFTPIIAKRPKVRNQHGRIN
YYWTLLEPGDTIIFEANGNLIAPWYAFALSRGFGSGSGSCIENINSKIYHIENEIAELAYLLGELAYKLGEYRI
AIRAYRIALKSDPNNAEAWYNLGNAYYKQGRYREAIEYYQKALELDPNNAEAWYNLGNAYYERGEYEEAI
EYYRKALRLDPNNADAMQNLLNAKMREEGGWELQHHHHHH

>TH-MI15-RBS1
MDSKGSSQKGSRLLLLLVVSNLLLPQGVLAVAPLHLGNCSIAGWILGNPECESLNTSSNWSYIVETSNSDN
GTCFPGNFINYEELRCQLSSVSSFERFEIFPKNSSWPNHDSNKGVTAACPHGNVKSFYKNLIWLVKKGAS
YPKLNQSYINDKGKEVLVLWGIHHPSTTTDQMNLYQNEDTYVFVSTSRYDKVFKPIIATRPKVRDQEGRM
NYYWTLVEPGDKITFEATGNLVVPRYAFTMERNAGSGSGSCIEHIENEIAELAYLLGELAYKLGEYRIAIRAY
RIALKSDPNNAEAWYNLGNAYYKQGRYREAIEYYQKALELDPNNAEAWYNLGNAYYERGEYEEAIEYYRK
ALRLDPNNADAMQNLLNAKMREEGGWELQHHHHHH

>TH-MI15-RBS2
MDSKGSSQKGSRLLLLLVVSNLLLPQGVLAVAPLHLGNCSIAGWILGNPECESLNTSSNWSYIVETSNSDN
GTCFPGNFINYEELRCQLSSVSSFERFEIFPKNSSWPNHDSNKGVTAACPHGNVKSFYKNLIWLVKKGDS
YPKLNQSYINDKGKEVLVLWGIHHPSTTKDQATLYQNEDTYVFVSTSRYDKVFKPIIATRPTVRGQQGRMN
YYWTLVEPGDKITFEATGNLVVPRYAFTMERNAGSGSGSCIEHIENEIAELAYLLGELAYKLGEYRIAIRAYRI
ALKSDPNNAEAWYNLGNAYYKQGRYREAIEYYQKALELDPNNAEAWYNLGNAYYERGEYEEAIEYYRKA
LRLDPNNADAMQNLLNAKMREEGGWELQHHHHHH

>TH-MI15-RBS3

MDSKGSSQKGSRLLLLLVVSNLLLPQGVLAVAPLHLGNCSIAGWILGNPECESLNTSSNWSYIVETSNSDN
GTCFPGNFINYEELRCQLSSVSSFERFEIFPKNSSWPNHDSNKGVTAACPHAGENSFYKNLIWLVKKGSS
YPKLNQSYINDKGKEVLVLWGIHHPSTTKDQMNLYQNEDTYVFVSTSRYDKVFKPIIATRPTVRGQQGRM
NYYWTLVEPGDKITFEATGNLVVPRYAFTMERNAGSGSGSCIEHIENEIAELAYLLGELAYKLGEYRIAIRAY
RIALKSDPNNAEAWYNLGNAYYKQGRYREAIEYYQKALELDPNNAEAWYNLGNAYYERGEYEEAIEYYRK
ALRLDPNNADAMQNLLNAKMREEGGWELQHHHHHH

>TH-MI15-RBS4
MDSKGSSQKGSRLLLLLVVSNLLLPQGVLAVAPLHLGNCSIAGWILGNPECESLNTSSNWSYIVETSNSDN
GTCFPGNFINYEELRCQLSSVSSFERFEIFPKNSSWPNHDSNKGVTAACPHAGAKSFYKNLIWLVKKGNS
YPKLNQSYINDKGKEVLVLWGIHHPSTTKDQATLYQNEDTYVFVSTSRYDKVFKPIIATRPKVRDQEGRMN
YYWTLVEPGDKITFEATGNLVVPRYAFTMERNAGSGSGSCIEHIENEIAELAYLLGELAYKLGEYRIAIRAYRI
ALKSDPNNAEAWYNLGNAYYKQGRYREAIEYYQKALELDPNNAEAWYNLGNAYYERGEYEEAIEYYRKA
LRLDPNNADAMQNLLNAKMREEGGWELQHHHHHH

>I53_dn5A pentamer
MDSKGSSQKGSRLLLLLVVSNLLLPQGVLAKYDGSKLRIGILHARGNAEIILELVLGALKRLQEFGVKRENIII
ETVPGSFELPYGSKLFVEKQKRLGKPLDAIIPIGVLIRGSTAHFDYIADSTTHQLMKLNFELGIPVIFGVLTTE
SDEQAEERAGTKAGNHGEDWGAAAVEMATKFNLEEQKLISEEDLHHHHHH

ELISA antigens

>Iowa43 (A/Iowa/1943)
MKARLLVLLCALAATDADTICIGYHANNSTDTVDTVLEKNVTVTHSVNLLEDSHNGKLCRLKGIAPLQLGKC
NIAGWILGNPECESLLSERSWSYIVETPNSENGTCFPGDFIDYEELREQLSSVSSFERFEIFSKESSWPKH
TTGGVTAACSHAGKSSFYRNLLWLTEKDGSYPNLNNSYVNKKGKEVLVLWGVHHPSNIKDQQTLYQKEN
AYVSVVSSNYNRRFTPEIAERPKVRGQAGRINYYWTLLKPGDTIMFEANGNLIAPWYAFALSRGFGSGIIT
SNASMHECDTKCQTPQGAINSSLPFQNIHPVTIGECPKYVRSTKLRMVTGLRNIPSIQSRGLFGAIAGFIEG
GWTGMIDGWYGYHWQNEQGSGYAADQKSTQNAINGITNIVNSVIEKMNTQFTAVGKEFNNLEKRMENLN
KKVDDGFLDIWTYNAELLVLLINERTLDFHDSNVKNLYEKVKNQLRNNAKEIGNGCFEFYHKCNNECMES
VKNGTYDYPKYSEESKLNREKIDGSGYIPEAPRDGQAYVRKDGEWVLLSTFLGSGLNDIFEAQKIEWHEG
HHHHHH

>Malaysia54 (A/Malaysia/302/1954)
MKARLLILLCALSATDADTICIGYHANNSTDTVDTVLEKNVTVTHSVNLLEDSHNGKLCRLKGIAPLQLGKC
NIAGWILGNPECESLLSNRSWSYIAETPNSENGICFPGDFADYEELREQLSSVSSFERFEIFPKESSWPKH
NITRGVTVACSHAKKSSFYKNLLWLTEANGLYPSLSKSYVNDREKEVLVLWGVHHPSNIEDQRTLYRKENA
YVSVVSSNYNRRFTPEIAERPKVRGQPGRMNYYWTLLEPGDKIIFEANGNLIAPWYAFALSRGPGSGIITS
NASMDECDTKCQTPQGAINSSLPFQNIHPVTIGECPKYVRSTKLRMVTGLRNIPSIQSRGLFGAIAGFIEG
GWTGMVDGWYGYHHQNEQGSGYAADQKSTQNAINGITNKVNSVIEKMNTQFTAVGKEFNKLEKRMENL
NKKVDDGFLDIWTYNAELLVLLENERTLDFHDSNVKNLYEKVKNQLRNNAKEIGNGCFEFYHKCDNECME
SVKNGTYDYPKYSEESKLNRAKIDGSGYIPEAPRDGQAYVRKDGEWVLLSTFLGSGLNDIFEAQKIEWHE
GHHHHHH

>USSR77 (A/USSR/90/1977)
MKAKLLVLLCALSATDADTICIGYHANNSTDTVDTVLEKNVTVTHSVNLLEDSHNGKLCRLKGIAPLQLGKC
NIAGWILGNPECESLFSKKSWSYIAETPNSENGACFPGYFADYEELREQLSSVSSFERFEIFPKERSWPK
HDVTRGVTASCSHKGKSSFYRNLLWLTEKNGSYPNLSKSYVNNKEKEVLVLWGVHHPSNIEDQKTIYRKE
NAYVSVVSSNYNRRFTPEIAERPKVRGQAGRINYYWTLLEPGDTIIFEANGNLIAPWHAFALNRGFGSGIIT

SNASMDECDTKCQTPQGAINSSLPFQNIHPVTIGECPKYVRSTKLRMVTGLRNIPSIQSRGLFGAIAGFIEG
GWTGMIDGWYGYHHQNEQGSGYAADQKSTQNAINGITNKVNSVIEKMNTQFTAVGKEFNKLEKRMENL
NKKVDDGFLDIWTYNAELLVLLENERTLDFHDSNVKNLYEKVKSQLKNNAKEIGNGCFEFYHKCNNECME
SVKNGTYDYPKYSEESKLNREKIDGSGYIPEAPRDGQAYVRKDGEWVLLSTFLGSGLNDIFEAQKIEWHE
GHHHHHH

>NC99 (A/New Caledonia/20/1999)
MKAKLLVLLCTFTATYADTICIGYHANNSTDTVDTVLEKNVTVTHSVNLLEDSHNGKLCLLKGIAPLQLGNC
SVAGWILGNPECELLISKESWSYIVETPNPENGTCFPGYFADYEELREQLSSVSSFERFEIFPKESSWPNH
TVTGVSASCSHNGKSSFYRNLLWLTGKNGLYPNLSKSYVNNKEKEVLVLWGVHHPPNIGNQRALYHTEN
AYVSVVSSHYSRRFTPEIAKRPKVRDQEGRINYYWTLLEPGDTIIFEANGNLIAPWYAFALSRGFGSGIITS
NAPMDECDAKCQTPQGAINSSLPFQNVHPVTIGECPKYVRSAKLRMVTGLRNIPQRETRGLFGAIAGFIE
GGWTGMVDGWYGYHHQNEQGSGYAADQKSTQNAINGITNKVNSVIEKMNTQFTAVGKEFNKLERRME
NLNKKVDDGFLDIWTYNAELLVLLENERTLDFHDSNVKNLYEKVKSQLKNNAKEIGNGCFEFYHKCNNEC
MESVKNGTYDYPKYSEESKLNREKIDGSGYIPEAPRDGQAYVRKDGEWVLLSTFLGSGLNDIFEAQKIEW
HEGHHHHHH

>NC99-T155N/K157T
MKAKLLVLLCTFTATYADTICIGYHANNSTDTVDTVLEKNVTVTHSVNLLEDSHNGKLCLLKGIAPLQLGNC
SVAGWILGNPECELLISKESWSYIVETPNPENGTCFPGYFADYEELREQLSSVSSFERFEIFPKESSWPNH
TVTGVSASCSHNGKSSFYRNLLWLNGTNGLYPNLSKSYVNNKEKEVLVLWGVHHPPNIGNQRALYHTEN
AYVSVVSSHYSRRFTPEIAKRPKVRDQEGRINYYWTLLEPGDTIIFEANGNLIAPWYAFALSRGFGSGIITS
NAPMDECDAKCQTPQGAINSSLPFQNVHPVTIGECPKYVRSAKLRMVTGLRNIPQRETRGLFGAIAGFIE
GGWTGMVDGWYGYHHQNEQGSGYAADQKSTQNAINGITNKVNSVIEKMNTQFTAVGKEFNKLERRME
NLNKKVDDGFLDIWTYNAELLVLLENERTLDFHDSNVKNLYEKVKSQLKNNAKEIGNGCFEFYHKCNNEC
MESVKNGTYDYPKYSEESKLNREKIDGSGYIPEAPRDGQAYVRKDGEWVLLSTFLGSGLNDIFEAQKIEW
HEGHHHHHH

>NC99-L194W
MKAKLLVLLCTFTATYADTICIGYHANNSTDTVDTVLEKNVTVTHSVNLLEDSHNGKLCLLKGIAPLQLGNC
SVAGWILGNPECELLISKESWSYIVETPNPENGTCFPGYFADYEELREQLSSVSSFERFEIFPKESSWPNH
TVTGVSASCSHNGKSSFYRNLLWLTGKNGLYPNLSKSYVNNKEKEVLVLWGVHHPPNIGNQRAWYHTEN
AYVSVVSSHYSRRFTPEIAKRPKVRDQEGRINYYWTLLEPGDTIIFEANGNLIAPWYAFALSRGFGSGIITS
NAPMDECDAKCQTPQGAINSSLPFQNVHPVTIGECPKYVRSAKLRMVTGLRNIPQRETRGLFGAIAGFIE
GGWTGMVDGWYGYHHQNEQGSGYAADQKSTQNAINGITNKVNSVIEKMNTQFTAVGKEFNKLERRME
NLNKKVDDGFLDIWTYNAELLVLLENERTLDFHDSNVKNLYEKVKSQLKNNAKEIGNGCFEFYHKCNNEC
MESVKNGTYDYPKYSEESKLNREKIDGSGYIPEAPRDGQAYVRKDGEWVLLSTFLGSGLNDIFEAQKIEW
HEGHHHHHH

>Brisbane07 (A/Brisbane/57/2007)
MKVKLLVLLCTFTATYADTICIGYHANNSTDTVDTVLEKNVTVTHSVNLLENSHNGKLCLLKGIAPLQLGNC
SVAGWILGNPECELLISKESWSYIVEKPNPENGTCFPGHFADYEELREQLSSVSSFERFEIFPKESSWPNH
TVTGVSASCSHNGESSFYRNLLWLTGKNGLYPNLSKSYANNKEKEVLVLWGVHHPPNIGVQKALYHTENA
YVSVVSSHYSRKFTPEIAKRPKVRDQEGRINYYWTLLEPGDTIIFEANGNLIAPRYAFALSRGFGSGIINSNA
PMDKCDAKCQTPQGAINSSLPFQNVHPVTIGECPKYVRSAKLRMVTGLRNIPSIQSRGLFGAIAGFIEGG
WTGMVDGWYGYHHQNEQGSGYAADQKSTQNAINGITNKVNSVIEKMNTQFTAVGKEFNKLERRMENLN
KKVDDGFIDIWTYNAELLVLLENERTLDFHDSNVKNLYEKVKSQLKNNAKEIGNGCFEFYHKCNDECMES
VKNGTYDYPKYSEESKLNREKIDGSGYIPEAPRDGQAYVRKDGEWVLLSTFLGSGLNDIFEAQKIEWHEG
HHHHHH

>MI15 (A/Michigan/45/2015)
MDSKGSSQKGSRLLLLLVVSNLLLPQGVLADTLCIGYHANNSTDTVDTVLEKNVTVTHSVNLLEDKHNGK
LCKLRGVAPLHLGKCNIAGWILGNPECESLSTASSWSYIVETSNSDNGTCFPGDFINYEELREQLSSVSSF
ERFEIFPKTSSWPNHDSNKGVTAACPHAGAKSFYKNLIWLVKKGNSYPKLNQSYINDKGKEVLVLWGIHH
PSTTADQQSLYQNADAYVFVGTSRYSKKFKPEIATRPKVRDQEGRMNYYWTLVEPGDKITFEATGNLVVP
RYAFTMERNAGSGIIISDTPVHDCNTTCQTPEGAINTSLPFQNIHPITIGKCPKYVKSTKLRLATGLRNVPSI
QSRGLFGAIAGFIEGGWTGMVDGWYGYHHQNEQGSGYAADLKSTQNAIDKITNKVNSVIEKMNTQFTAV
GKEFNHLEKRIENLNKKVDDGFLDIWTYNAELLVLLENERTLDYHDSNVKNLYEKVRNQLKNNAKEIGNGC
FEFYHKCDNTCMESVKNGTYDYPKYSEEAKLNREKIDGVGSGYIPEAPRDGQAYVRKDGEWVLLSTFLG
SGLNDIFEAQKIEWHEGHHHHHH

HA-Ferritin nanoparticles used in HAI assays

>Iowa43-ferritin
MKARLLVLLCALAATDADTICIGYHANNSTDTVDTVLEKNVTVTHSVNLLEDSHNGKLCRLKGIAPLQLGKC
NIAGWILGNPECESLLSERSWSYIVETPNSENGTCYPGDFIDYEELREQLSSVSSFERFEIFSKESSWPKH
TTGGVTAACSHAGKSSFYRNLLWLTEKDGSYPNLNNSYVNKKGKEVLVLWGVHHPSNIKDQQTLYQKEN
AYVSVVSSNYNRRFTPEIAERPKVRGQAGRINYYWTLLKPGDTIMFEANGNLIAPWYAFALSRGFGSGIIT
SNASMHECDTKCQTPQGAINSSLPFQNIHPVTIGECPKYVRSTKLRMVTGLRNIPSIQSRGLFGAIAGFIEG
GWTGMIDGWYGYHHQNEQGSGYAADQKSTQNAINGITNKVNSVIEKMNTQFTAVGKEFNNLEKRMENL
NKKVDDGFLDIWTYNAELLVLLENERTLDFHDSNVKNLYEKVKNQLRNNAKEIGNGCFEFYHKCNNECME
SVKNGTYDYPKYSEESKLNREKIDSGGDIIKLLNEQVNKEMQSSNLYMSMSSWCYTHSLDGAGLFLFDHA
AEEYEHAKKLIIFLNENNVPVQLTSISAPEHKFEGLTQIFQKAYEHEQHISESINNIVDHAIKSKDHATFNFLQ
WYVAEQHEEEVLFKDILDKIELIGNENHGLYLADQYVKGIAKSRKS

>Malaysia54-ferritin
MKARLLILLCALSATDADTICIGYHANNSTDTVDTVLEKNVTVTHSVNLLEDSHNGKLCRLKGIAPLQLGKC
NIAGWILGNPECESLLSNRSWSYIAETPNSENGICYPGDFADYEELREQLSSVSSFERFEIFPKESSWPKH
NITRGVTVACSHAKKSSFYKNLLWLTEANGLYPSLSKSYVNDREKEVLVLWGVHHPSNIEDQRTLYRKENA
YVSVVSSNYNRRFTPEIAERPKVRGQPGRMNYYWTLLEPGDKIIFEANGNLIAPWYAFALSRGPGSGIITS
NASMDECDTKCQTPQGAINSSLPFQNIHPVTIGECPKYVRSTKLRMVTGLRNIPSIQSRGLFGAIAGFIEG
GWTGMVDGWYGYHHQNEQGSGYAADQKSTQNAINGITNKVNSVIEKMNTQFTAVGKEFNKLEKRMENL
NKKVDDGFLDIWTYNAELLVLLENERTLDFHDSNVKNLYEKVKNQLRNNAKEIGNGCFEFYHKCDNECME
SVKNGTYDYPKYSEESKLNRAKIDSGGDIIKLLNEQVNKEMQSSNLYMSMSSWCYTHSLDGAGLFLFDHA
AEEYEHAKKLIIFLNENNVPVQLTSISAPEHKFEGLTQIFQKAYEHEQHISESINNIVDHAIKSKDHATFNFLQ
WYVAEQHEEEVLFKDILDKIELIGNENHGLYLADQYVKGIAKSRKS

>USSR77-ferritin
MKAKLLVLLCALSATDADTICIGYHANNSTDTVDTVLEKNVTVTHSVNLLEDSHNGKLCRLKGIAPLQLGKC
NIAGWILGNPECESLFSKKSWSYIAETPNSENGACYPGYFADYEELREQLSSVSSFERFEIFPKERSWPK
HDVTRGVTASCSHKGKSSFYRNLLWLTEKNGSYPNLSKSYVNNKEKEVLVLWGVHHPSNIEDQKTIYRKE
NAYVSVVSSNYNRRFTPEIAERPKVRGQAGRINYYWTLLEPGDTIIFEANGNLIAPWHAFALNRGFGSGIIT
SNASMDECDTKCQTPQGAINSSLPFQNIHPVTIGECPKYVRSTKLRMVTGLRNIPSIQSRGLFGAIAGFIEG
GWTGMIDGWYGYHHQNEQGSGYAADQKSTQNAINGITNKVNSVIEKMNTQFTAVGKEFNKLEKRMENL
NKKVDDGFLDIWTYNAELLVLLENERTLDFHDSNVKNLYEKVKSQLKNNAKEIGNGCFEFYHKCNNECME
SVKNGTYDYPKYSEESKLNREKIDSGGDIIKLLNEQVNKEMQSSNLYMSMSSWCYTHSLDGAGLFLFDHA
AEEYEHAKKLIIFLNENNVPVQLTSISAPEHKFEGLTQIFQKAYEHEQHISESINNIVDHAIKSKDHATFNFLQ
WYVAEQHEEEVLFKDILDKIELIGNENHGLYLADQYVKGIAKSRKS

>NC99-ferritin
MKAKLLVLLCTFTATYADTICIGYHANNSTDTVDTVLEKNVTVTHSVNLLEDSHNGKLCLLKGIAPLQLGNC
SVAGWILGNPECELLISKESWSYIVETPNPENGTCYPGYFADYEELREQLSSVSSFERFEIFPKESSWPNH
TVTGVSASCSHNGKSSFYRNLLWLTGKNGLYPNLSKSYVNNKEKEVLVLWGVHHPPNIGNQRALYHTEN
AYVSVVSSHYSRRFTPEIAKRPKVRDQEGRINYYWTLLEPGDTIIFEANGNLIAPWYAFALSRGFGSGIITS
NAPMDECDAKCQTPQGAINSSLPFQNVHPVTIGECPKYVRSAKLRMVTGLRNIPQRETRGLFGAIAGFIE
GGWTGMVDGWYGYHHQNEQGSGYAADQKSTQNAINGITNKVNSVIEKMNTQFTAVGKEFNKLERRME
NLNKKVDDGFLDIWTYNAELLVLLENERTLDFHDSNVKNLYEKVKSQLKNNAKEIGNGCFEFYHKCNNEC
MESVKNGTYDYPKYSEESKLNREKISGGDIIKLLNEQVNKEMQSSNLYMSMSSWCYTHSLDGAGLFLFD
HAAEEYEHAKKLIIFLNENNVPVQLTSISAPEHKFEGLTQIFQKAYEHEQHISESINNIVDHAIKSKDHATFNF
LQWYVAEQHEEEVLFKDILDKIELIGNENHGLYLADQYVKGIAKSRKS

>Brisbane07-ferritin
MKVKLLVLLCTFTATYADTICIGYHANNSTDTVDTVLEKNVTVTHSVNLLENSHNGKLCLLKGIAPLQLGNC
SVAGWILGNPECELLISKESWSYIVEKPNPENGTCYPGHFADYEELREQLSSVSSFERFEIFPKESSWPN
HTVTGVSASCSHNGESSFYRNLLWLTGKNGLYPNLSKSYANNKEKEVLVLWGVHHPPNIGIQKALYHTEN
AYVSVVSSHYSRKFTPEIAKRPKVRDQEGRINYYWTLLEPGDTIIFEANGNLIAPRYAFALSRGFGSGIINSN
APMDKCDAKCQTPQGAINSSLPFQNVHPVTIGECPKYVRSAKLRMVTGLRNIPSIQSRGLFGAIAGFIEGG
WTGMVDGWYGYHHQNEQGSGYAADQKSTQNAINGITNKVNSVIEKMNTQFTAVGKEFNKLERRMENLN
KKVDDGFIDIWTYNAELLVLLENERTLDFHDSNVKNLYEKVKSQLKNNAKEIGNGCFEFYHKCNDECMES
VKNGTYDYPKYSEESKLNREKIDSGGDIIKLLNEQVNKEMQSSNLYMSMSSWCYTHSLDGAGLFLFDHAA
EEYEHAKKLIIFLNENNVPVQLTSISAPEHKFEGLTQIFQKAYEHEQHISESINNIVDHAIKSKDHATFNFLQW
YVAEQHEEEVLFKDILDKIELIGNENHGLYLADQYVKGIAKSRKSGS

>MI15-ferritin
MDSKGSSQKGSRLLLLLVVSNLLLPQGVLADTLCIGYHANNSTDTVDTVLEKNVTVTHSVNLLEDKHNGK
LCKLRGVAPLHLGKCNIAGWILGNPECESLSTASSWSYIVETSNSDNGTCYPGDFINYEELREQLSSVSSF
ERFEIFPKTSSWPNHDSNKGVTAACPHAGAKSFYKNLIWLVKKGNSYPKLNQSYINDKGKEVLVLWGIHH
PSTTADQQSLYQNADAYVFVGTSRYSKKFKPEIATRPKVRDQEGRMNYYWTLVEPGDKITFEATGNLVVP
RYAFTMERNAGSGIIISDTPVHDCNTTCQTPEGAINTSLPFQNIHPITIGKCPKYVKSTKLRLATGLRNVPSI
QSRGLFGAIAGFIEGGWTGMVDGWYGYHHQNEQGSGYAADLKSTQNAIDKITNKVNSVIEKMNTQFTAV
GKEFNHLEKRIENLNKKVDDGFLDIWTYNAELLVLLENERTLDYHDSNVKNLYEKVRNQLKNNAKEIGNGC
FEFYHKCDNTCMESVKNGTYDYPKYSEEAKLNREKIDSGGDIIKLLNEQVNKEMQSSNLYMSMSSWCYT
HSLDGAGLFLFDHAAEEYEHAKKLIIFLNENNVPVQLTSISAPEHKFEGLTQIFQKAYEHEQHISESINNIVD
HAIKSKDHATFNFLQWYVAEQHEEEVLFKDILDKIELIGNENHGLYLADQYVKGIAKSRKS

Table S1.2 Glycopeptide sequences and occupancies, related to Figure 1.1

Construct	Glycopeptide sequence	Sequon	Position	Occupancy (%)
TH-NC99	IAPLQLG**NCS**VAGWILGN PE	G.NCS.V	63	86.6
	NGTCFPGYFADYEE	E.NGT.C	94	99
	ESSWP**NHT**VTGVSASCS HNGK	P.NHT.V	129	99.6
	NGLYP**NLS**K	P.NLS.K	163	45.1
TH-NC99-7gly	IAPLQLG**NCS**VAGWILGN PE	G.NCS.V	63	86.2
	LLI**NAS**SWSYIVET	I.NAS.S	81	46.2
	NGTCFPGYFADYEE	E.NGT.C	94	98.8
	NSSWP**NHT**VTGVSASCS HNGK	K.NSS.W	125b	8.4 single, 91.5 double
		P.NHT.V	129	
	NGLYP**NLS**K	P.NLS.K	163	44.3
	SYVN**NK(S)**	N.NKS.K	171	20.1
TH-NC99-9gly	IAPLQLG**NCS**VAGWILGN PE	G.NCS.V	63	70
	NLSI**NAS**SWSYIVE	C.NLS.I	77	63 single, 37 double
		I.NAS.S	81	
	NGTCFPGYFADYEE	E.NGT.C	94	99.6
	NSSWP**NHT**VTGVSASCS HNGK	K.NSS.W	125b	5.0 single, 95.0 double
		P.NHT.V	129	
	NGLYP**NLS**K	P.NLS.K	163	44.2
	NGLYP**NLS**K**NYT**N**NK(S)**	P.NLS.K	163	49.4 single, 40.8 double, 9.8 triple
		K.NYT.N	167	
		N.NKS.K	171	

Table S1.3 Mutations introduced into hypervariable trihead antigens, related to Figure 1.3

Trihead RBS variant	Mutations
TH-SC18-RBS1	A144E/S145N/K157S/S159D/T189A/Q192T/S193D
TH-SC18-RBS2	A144M/S145N/S159N/T189E/Q192K/K222E/A227I
TH-SC18-RBS3	A144E/S145D/S159K/T189A/Q192E/S193D/K222Q/ D225N/A227I
TH-SC18-RBS4	S145A/T189E/Q192K/K222E/D225N/A227K
TH-PR34-RBS1	K144Q/S145D/K189S/Q192K/D225G/A227H
TH-PR34-RBS2	E158Q/K189E/Q192T/N193A/K222E/D225G/A227H
TH-PR34-RBS3	E158K/K189N/Q192I/N193S/A227S
TH-PR34-RBS4	Q192H/N193D
TH-NC99-RBS1	G143S/K144V/G189E/R192H/K222A/E227K
TH-NC99-RBS2	K144E/N158G/G159D/G189Q/R192L/A193N/K222V/ E227Q
TH-NC99-RBS3	K144Q/S145L/N158S/R192K/K222V/D225N/E227Q
TH-NC99-RBS4	K144Q/S145L/G189Q/R192L/A193N/D225N/E227H
TH-MI15-RBS1	A142G/G143N/A144V/A189T/Q192M/S193N
TH-MI15-RBS2	A142G/G143N/A144V/N159D/A189K/Q192A/S193T/ K222T/Q225G/G227Q
TH-MI15-RBS3	A144E/K145N/N159S/A189K/Q192M/S193N/K222T/ Q225G/G227Q
TH-MI15-RBS4	A189K/Q192A/S193T

Chapter 2. Design and characterization of H3 and B Triheads

2.1 Results

2.1.1 Design and characterization of H3 Triheads

Given the success of H1 triheads to induce potent HAI and neutralization responses in both mouse and rabbit animal models, and to match the current influenza seasonal strains, we sought to apply the trihead design strategies used for H1 triheads to create both H3 and type B triheads.

The H1 trihead design strategy was adapted for H3 and type B influenza hemagglutinin strains. Initial design constructs for the H3 trihead were made using the strain A/Hong Kong/1/1968. The same cut-points as the H1 trihead were used for the H3 trihead, encompassing residues 57-264 (H3 numbering). Initial H3 ‘monohead’ designs had a 2-heptad linker and included resurfacing mutations to the hydrophobic scar left at the HA cut-points but lacked any designed disulfide bonds or trimer interface mutations. This initial design showed no expression. Since some mutations to the RBS periphery made during the design of the hypervariable H1 trihead were seen to dramatically increase expression, some of these mutations were applied to improve H3 trihead expression. This design strategy makes sense in the context of influenza virus evolution, wherein the RBD is a highly immunodominant epitope on HA and, though the RBS must conserve key residues in order to maintain receptor sialic acid binding, the RBS periphery has evolved dramatically in order to escape immune pressure (Koel et al. 2013; Zost et al. 2019; Angeletti et al. 2017; Altman, Angeletti, and Yewdell 2018). This evolution is thus a result of immune evasion and does not necessarily correlate with improved structural integrity of HA. Three initial mutations in the RBS periphery, G142N/P143G/G144E, on the H3 monohead showed detectable C05 binding by BLI in a small scale screen (data not shown), as compared to no C05 binding in previous constructs. Further resurfacing mutations were made based on structural observation and natural H3 sequence conservation data, comprising I62E/V78G/L86Q/A106E/S114E/T192K/W234Y/V244T. This design led to a low level of expression by C05 binding, SEC, and SDS-PAGE (data not shown). The same designed disulfide bond between the HA head and the GCN domain was also successfully used in the H3 trihead, between residue 110 and the first residue on the GCN domain. Finally, trimer interface mutations, similar to those in H1 trihead design, were introduced, resulting in a 50-fold enhancement of expression. This is by contrast to H1 trihead design, where the H1 monoheads expressed well and introduction of hydrophobic trimer interface mutations slightly reduced expression. This HK68 trihead design (TH-HK68), which included all aforementioned mutations and S203L/Q210E/T212A/N216V mutations at the trimer interface, showed a large soluble trimer peak by SEC at ~14 mL when purified in a 25 mM Tris, pH 8.0, 150 mM NaCl, 200 mM Arginine, 5% glycerol buffer **(Figure 2.1A)**. This protein was then assembled into trihead-I53_dn5 nanoparticles and purified on SEC. This trihead antigen was fully resolved as displayed on the surface of the nanoparticle in nsEM 2D class averages, indicating rigid, closed trimeric head formation **(Figure 2.1B)**. The TH-HK68 nanoparticle component showed high C05 binding with minimal FluA-20 binding **(Figure 2.1C)**, indicating both RBS antigenic preservation and trimer interface closure.

Similar expression-enhancing and trimer interface mutations used in TH-HK68 design were introduced into the more recent H3 A/Hong Kong/1/2014 strain. Differences between these two strains are notable at the trimer interface, which is slightly wider in HK14, so it has T212V/N216VI instead of T212A/N216V in TH-HK68. This construct, TH-HK14, also expressed very well, eluted mostly as soluble trimer at ~13 mL on SEC in 25 mM Tris, pH 8.0, 150 mM NaCl, 5% glycerol buffer **(Figure 2.1A)**, and bound to C05 but also bound to FluA-20 **(Figure 2.1D)**, so it is not yet a fully closed trihead. This TH-HK14 construct lacked the Q210E mutation that enhanced expression and closure in TH-HK68, so that mutation will be tested in future efforts to improve TH-HK14.

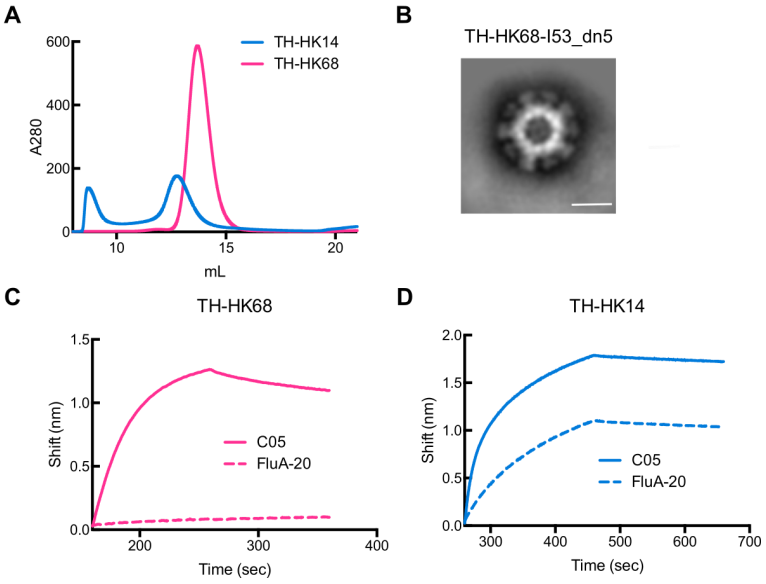

Figure 2.1 Biophysical characterization of H3 triheads
(A) SEC chromatograms of TH-HK68 and TH-HK14 on a Superdex 200 Increase 10/300 GL column.
(B) nsEM 2D class averages of TH-HK68-I53_dn5. Scale bar = 25 nm.
(C) BLI of mAbs C05 and FluA-20 against TH-HK68 and D) TH-HK14.

2.1.2 Design and characterization of type B Triheads

Design of an initial influenza B monohead started with trying several constructs with various HA head cut-points of the Victoria lineage B/Brisbane/60/2008 strain. These included the same cut-point as the type A triheads with residues 49-277 in type B numbering (TB1), inclusion of an additional β-strand at the C-terminus with residues 49-283 (TB2), and one design that included the entire vestigial esterase domain of HA with residues 31-326 fused with a short, flexible linker to I53_dn5B (TB-long). All constructs showed high protein expression by SDS-PAGE, however only TB2 and TB-long showed binding to anti-type B RBS mAb CR8033 (Dreyfus et al. 2012) (data not shown), indicating proper folding. TB2 was chosen to move forward for further trihead design to maximize potent RBD responses with this more minimal RBD construct. The type B head structure was too different from the type A heads to apply the same designed disulfide bond mediating head closure. Thus, a new disulfide bond was designed between residue Q106 in the type B head and at the third position away from the N-terminus of the GCN domain within the flexible linker connecting the heads to the GCN domain (**Figure 2.2A**). This construct, with

an additional S213I hydrophobic mutation at the trimer interface, showed good expression by SDS-PAGE and was antigenically intact as it bound to CR8033 (data not shown). However, nsEM 2D averages showed little resolution of head antigen as displayed on assembled I53_dn5 nanoparticles **(Figure 2.2B)**. Since no anti-trimer interface mAbs have been characterized for influenza B HA, nsEM averaging of nanoparticles was the only assay used to indicate head closure for this type.

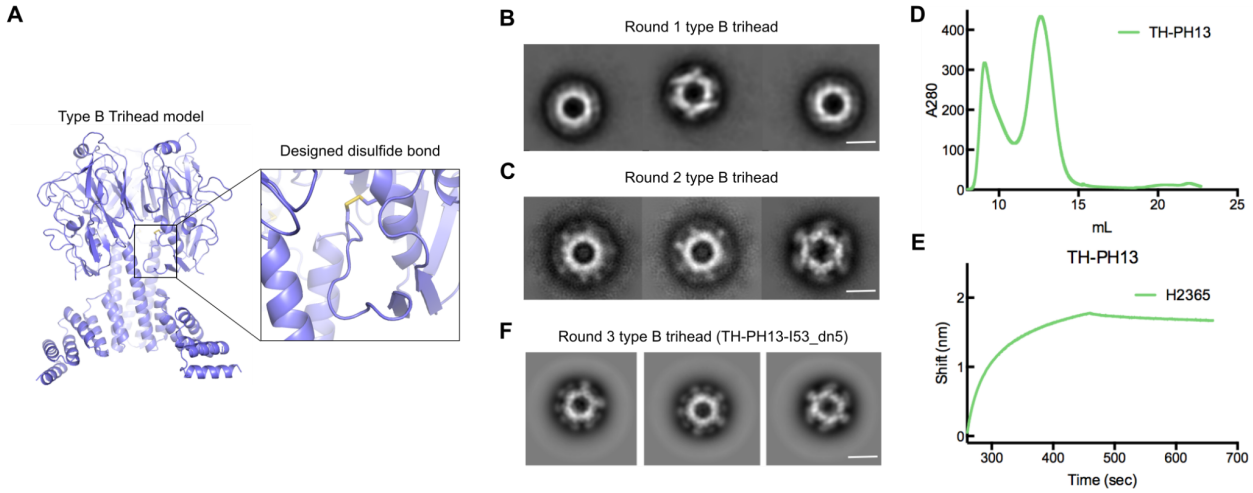

Figure 2.2 Biophysical characterization of type B triheads

(A) Model of type B trihead design and blow up of designed disulfide bond.
(B) nsEM 2D class averages of round 1 and C) round 2 type B trihead design. Scale bar = 25 nm.
(D) SEC chromatogram of TH-PH13 on a Superdex 200 Increase 10/300 GL column.
(E) BLI of mAb H2365 against TH-PH13.
(F) nsEM 2D class averages of round 3 of type B trihead design (TH-PH13-I53_dn5). Scale bar = 25 nm.

In the next round of type B trihead design, the Yamagata lineage strain B/Phuket/3073/2013 was used instead of the BR08 strain because the newly-discovered anti-RBS mAb H2365 (Bajic and Harrison 2021) against the Yamagata lineage showed better BLI signal than CR8033, and the same cut-point, designed disulfide bond, and S213I mutation still showed high expression as a preliminary type B trihead in this strain. The hydrophobic mutations R101L and V259I, along with M98R to maintain an electrostatic contact with E173, at the trimer interface showed a slight improvement in head rigidity on the nanoparticle surface by nsEM averaging as compared to the previous design **(Figure 2.2C).** To further improve head trimer closure, additional trimer interface mutations were introduced that comprised hydrophobic interactions T257I/T171V/Q224A, an electrostatic pair at N168E/N206K, and K209Q at the center of the trimer to relieve positive charge repulsion. All of these 10 total mutations combined resulted in a type B trihead construct, TH-PH13, that showed high expression by SEC **(Figure 2.2D)**, was antigenically intact by mAb H2365 binding measured using BLI **(Figure 2.2E)**, and showed well-resolved trimeric head antigen as displayed on the nanoparticle surface by nsEM **(Figure 2.2F).**

Given that triheads for all four seasonal strains are close to being developed, the goal with this project is to develop them as a potential seasonal influenza vaccine candidate. Given the success of mRNA as a versatile, fast, and highly effective vaccine modality (Corbett et al. 2020; Sahin et al. 2021), we are aiming to create mRNA-based trihead nanoparticles. Currently, only one-component nanoparticles, consisting of a single gene, are able to be used for mRNA vaccines. Thus, active efforts are underway to create new one-component nanoparticles specifically tailored for the trihead antigen.

Chapter 3. Probing effects of antigen spacing to optimally elicit broad HA stem responses

3.1 Introduction

Our lab has previously reported on the display of HA ectodomain trimers on the icosahedral nanoparticle I53_dn5 (Ueda et al. 2020). We showed that a mosaic of the four seasonal HA strains elicited superior breadth in the resulting immune response as compared to both a cocktail version and the QIV, and that this increase in breadth was due to an increase in anti-stem antibodies (Boyoglu-Barnum et al. 2021). This result prompted the exploration of why these mosaic nanoparticles elicited such an increase in HA stem responses. Our hypothesis was that the geometry in which the HA stem was being presented to BCRs as displayed on I53_dn5 was conducive to simultaneously binding of both Fab arms of the BCR to neighboring antigens. This 'bivalent ligation' interaction was posited to engage anti-stem B cells with higher avidity, leading to their increased activation. Here we sought to test this theory using *in silico* modeling, *in vitro* binding, and finally an *in vivo* study to probe HA antigen spacing as displayed on nanoparticles.

3.2 Results

3.2.1 *In silico* modeling of HA nanoparticle bivalent ligation

Modeling of bivalent ligation of anti-HA antibodies to HA-I53_dn5 nanoparticles was done using PyMOL ("PyMOL" n.d.). Crystal structures of HA-C05 (PDB: 4fqr) and HA-CR9114 (PDB: 4fqy) were modeled with HA docked onto the trimeric component I53_dn5B within the context of I53_dn5. Since HA is flexibly attached to I53_dn5, rotation of two neighboring HAs about their own 3-fold axes was sampled in 1° increments, while measuring the distance between Fab C-termini at each increment. This distance is where the hinge region of an IgG would be and is typically around 20-40 Å. Thus, the minimal distance between Fab C-termini modeled as bound to HA-I53_dn5 was found to see if it would fall in the 20-40 Å range that would be expected to accommodate bivalent ligation of an IgG. In addition to the rotational degree of freedom, there are also translational degrees of freedom that we did not model, so this is only a rough approximation of the total motion of HA relative to I53_dn5. Using this method, the minimal distance between Fab C-termini of C05 bound to HA-I53_dn5 was 130.1 Å, but was 51.8 Å for CR9114 **(Figure 3.1A)**. Based on these measurements, bivalent ligation is not likely to be possible for C05, but it may be possible for CR9114 given that it is close to the IgG hinge distance range and given additional translational degrees of freedom.

3.2.2 Biophysical characterization of HA nanoparticle bivalent ligation using BLI and cryoEM

We next sought to determine if these antibodies were able to bivalently ligate to HA-I53_dn5 using BLI to test *in vitro* binding. Previous work on the characterization of C05 showed that binding to the H3 HA strain A/Panama/07/99 has an intermediate affinity of 720 nM (Ekiert et al. 2012). While both the C05 IgG and Fab showed similar association rates to this HA, the IgG showed very little dissociation and the Fab showed complete dissociation. This difference can be attributed to the bivalent ligation of C05 IgG to neighboring HAs on the surface of the biosensor that decreases the apparent dissociation rate. This motivated us to make an

HA-I53_dn5 nanoparticle using a strain that had intermediate affinities to both C05 and CR9114. In that same aforementioned study, the H3 strain A/Hong Kong/1/68 had a similar intermediate affinity for C05 of 430 nM (Ekiert et al. 2012). This same strain with a D19N mutation in the stem epitope also exhibited a high dissociation rate against the CR9114 Fab (Dreyfus et al. 2012). Thus HK68-D19N-I53_dn5 was used to test bivalent ligation of C05 and CR9114. This was accomplished using a sandwich BLI approach by first chemically conjugating the anti-H3 RBS mAb F045-092 (P. S. Lee et al. 2014) to AR2G biosensors. This mAb captured the HA nanoparticle to subsequently test antibody binding. The results from this experiment showed that the C05 IgG and Fabs behaved similarly, both exhibiting binding to the nanoparticles but also a high degree of dissociation **(Figure 3.1B)**. This was by contrast to CR9114, where the Fab bound and dissociated, but the IgG bound with no subsequent dissociation. These results agree with the predictions from our *in silico* modeling and further support that bivalent ligation is occurring with anti-stem antibodies to HA nanoparticles.

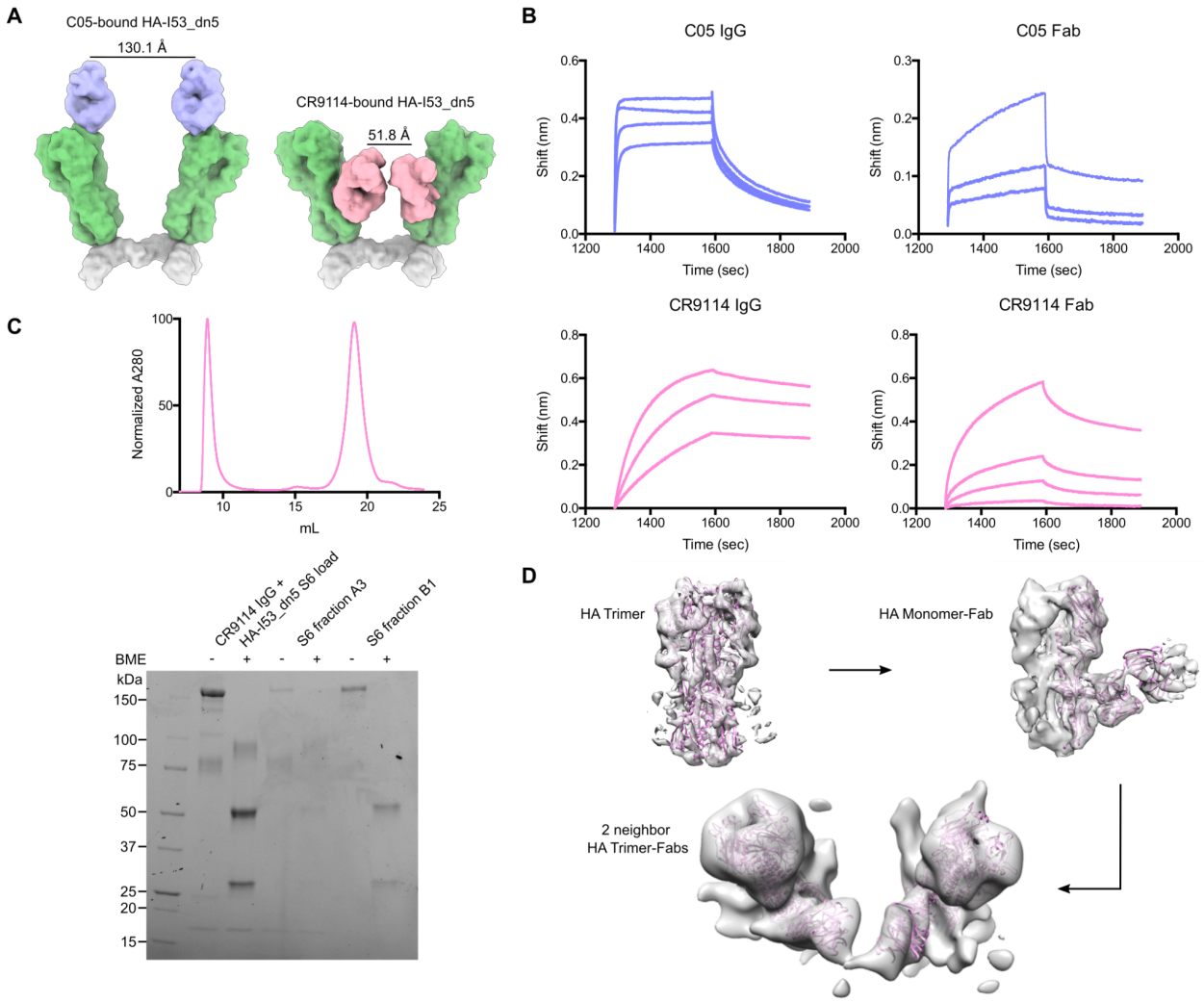

Figure 3.1 Modeling, *in vitro*, and cryoEM data of antibody bivalent ligation to HA-I53_dn5
(A) Modeling of C05 and CR9114 bivalent ligation to the HA-I53_dn5 nanoparticle.

(B) BLI of the HK68-D19N-I53_dn5 nanoparticle against C05 and CR9114 IgGs and Fabs.
(C) SEC chromatogram and SDS-PAGE gel of CR9114 IgG in complex with HK68-D19N-I53_dn5 on a Superose 6 Increase 10/300 GL column.
(D) Localized reconstruction from the CR9114+HK68-D19N-I53_dn5 complex of one HA trimer, one HA monomer in complex with one CR9114 Fab arm, and a final reconstruction of two neighboring HA trimers each in complex with a single CR9114 Fab arm.

In addition to probing for nanoparticle bivalent ligation using BLI, we sought to directly visualize this interaction using cryo-electron microscopy (cryoEM). CR9114 was first mixed at a 20:1 molar ratio with HK68-D19N-I53_dn5. SEC was used to purify this antibody-nanoparticle complex and its formation in an early eluate fraction was confirmed by SDS-PAGE **(Figure 3.1C)**. CryoEM was then used to solve a localized reconstruction of this complex that focused on the interaction of CR9114 with two neighboring HA trimers on the surface of I53_dn5 **(Figure 3.1D)**. This was done by first focusing alignments on one HA trimer to yield a 6.5 Å resolution HA trimer structure, then on a single HA monomer in complex with a single Fab arm of CR9114, yielding a structure at 6.1 Å resolution. Refined particles in this monomeric HA-Fab structure were then subject to a 2D classification without alignment to yield classes that also contained a neighboring HA, that were then selected for a final round of refinement. This resulted in a structure of two neighboring HAs, each in complex with a CR9114 Fab arm. A small amount of density was seen connecting these two Fab arms, and their close proximity suggests that they likely belong to a single IgG. Moreover, the possibility of these Fabs belonging to separate IgGs is low due to the steric hindrance that two IgGs would encounter in such a binding orientation. Rigid-body docking of the HA-CR9114 crystal structure into each of these neighboring densities closely matched the *in silico* modeling, with a very similar hinge distance of 51.6 Å. Taken together, this structural data and the BLI data strongly suggests that bivalent ligation of anti-stem mAbs to HA-I53_dn5 nanoparticles is occurring and encouraged further exploration of its effects *in vivo*.

3.2.3 Design and characterization of a novel icosahedral nanoparticle with I32 symmetry

Observations of the *in silico* modeling and cryoEM structure of CR9114 bound to HA-I53_dn5 showed that antibody Fab arms were bound in a somewhat sterically crowded position relative to each other in order to accommodate bivalent binding. Based on these observations, we hypothesized that increased spacing between HA antigens would be more conducive to bivalent ligation of anti-stem antibodies and thus improve their elicitation *in vivo*. We modeled increased spacing of trimer nanoparticle components using PyMOL, such that bivalent ligation of the CR9114 IgG would be promoted on the 2-fold axis of an ideal HA nanoparticle, without any crowding of its Fab arms. We then calculated that the approximate cage diameter needed to accommodate this ideal anti-stem bivalent ligation would be 35 nm, notably larger than the 25 nm diameter of I53_dn5.

To create a new nanoparticle idealized for anti-HA stem bivalent ligation, Cara Chao, Rob de Haas, and I together worked to design cages with I32 symmetry since this symmetry tends to produce larger cages than an I53 symmetry. An I32 symmetry is composed of trimeric and dimeric building blocks, and thus libraries of both wild-type and *de novo* oligomers with C2

symmetry were compilated for use in initial docking with the I53_dn5B and I53-50A (Bale et al. 2016) (PDB: 1wa3) trimers, since both of these have externally facing N-termini and were validated to display stable, trimeric HA upon genetic fusion. Pairwise docking of each oligomer into an I32 nanoparticle symmetry was done using RPXdock (Sheffler et al. 2022), while keeping the N-terminus of the C3 component facing outward. Filtering was then done to obtain only those nanoparticle docks with diameters between 30 to 40 nm. The resulting nanoparticle docks were then designed using ProteinMPNN (Dauparas et al. 2022), where any residue on one component that was within 8 Å from any residue on the other component was allowed to design. Scoring on the nanoparticle interface was then done using Rosetta in order to filter top designs, which included the following cutoffs: ddG<-50, SASA>1200, and SC>0.6 (Leman et al. 2020). This resulted in 24 I32 nanoparticle designs that were cloned as bicistronic genes and tested for expression and assembly in *E. coli*. Designs were purified using ion-metal affinity chromatography (IMAC) followed by SEC on a Superose 6 Increase 10/300, where nanoparticle elution would be expected between 9-12 mL. One design, I32-18, showed a substantial peak at ~10 mL and this fraction was also seen to form nanoparticle assemblies by nsEM **(Figure 3.2A)**. Despite clear nanoparticle formation in this micrograph, we also saw a large amount of much smaller protein, a lot of which was clearly trimeric and likely corresponds to one of the nanoparticle components. Subjecting this material to SEC again resulted in a peak at 10 mL but also a peak at 17 mL, which was observed in the first SEC chromatogram as well and corresponds to free nanoparticle component. These results indicated that this nanoparticle was forming, but its formation was unstable and prone to disassembly.

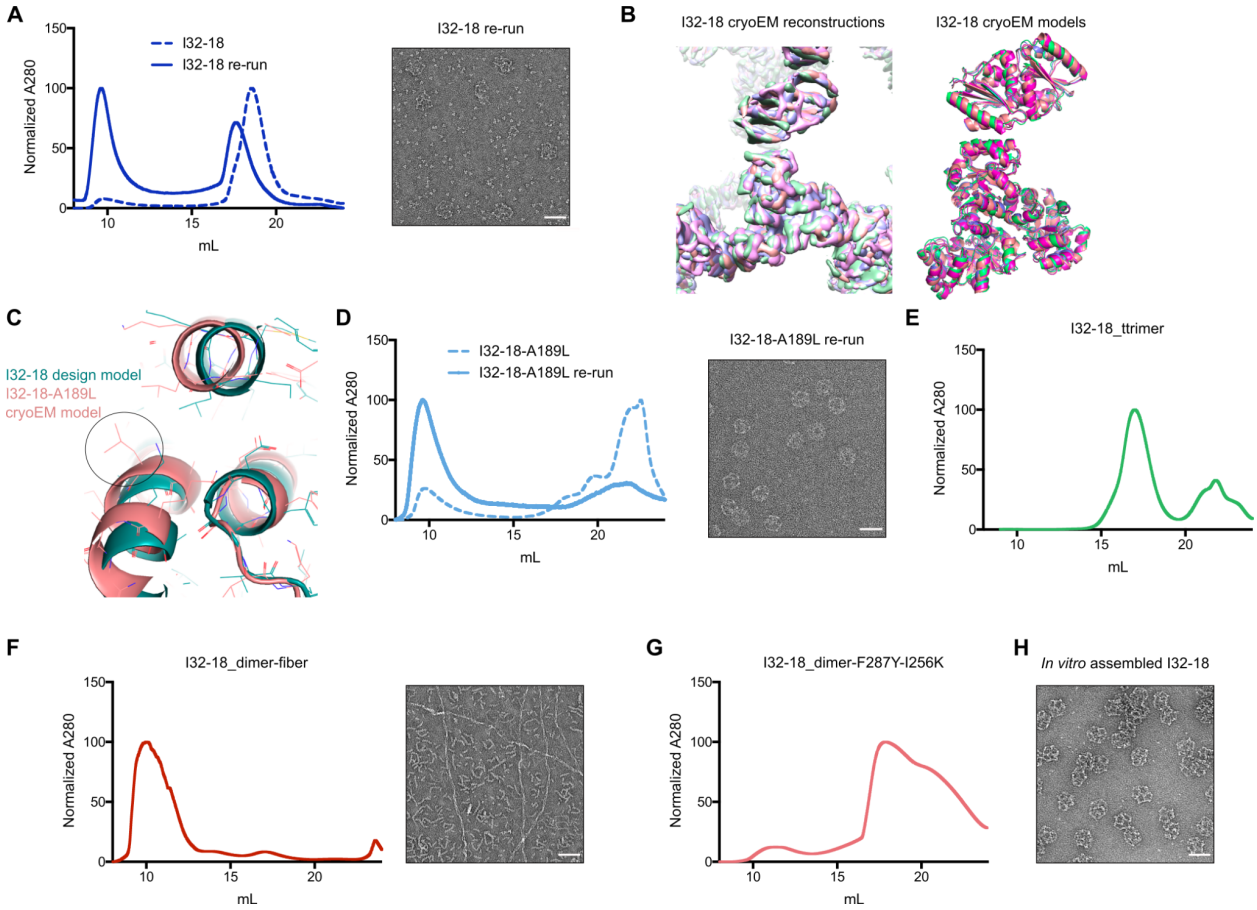

Figure 3.2 Development of I32-18 nanoparticle

(A) SEC chromatogram on a Superose 6 Increase 10/300 GL column of I32-18 run after IMAC (dotted line) and run on SEC for a second time (solid line). nsEM micrograph of ~10 mL peak of the I32-18 SEC re-run. Scale bar = 50 nm.

(B) I32-18 cryoEM reconstructions and fitted models.

(C) I32-18 original design model in green and I32-18 cryoEM model in pink with A189L mutation circled.

(D) SEC chromatogram on a Superose 6 Increase 10/300 GL column of I32-18-A189L run after IMAC (dotted line) and run on SEC for a second time (solid line). nsEM micrograph of ~10 mL peak of the I32-18-A189L SEC re-run. Scale bar = 50 nm.

(E) SEC chromatogram of I32-18_trimer on a Superdex 200 Increase 10/300 GL column.

(F) SEC chromatogram on a Superdex 200 Increase 10/300 GL column and nsEM micrograph of I32-18_dimer-fiber from ~10 mL fraction. Scale bar = 50 nm.

(G) SEC chromatogram on a Superdex 200 Increase 10/300 GL column of I32-18_dimer-F287Y-I256K.

(H) nsEM micrograph of *in vitro* assembled I32-18 using I32-18_trimer and I32-18_dimer-F287Y-I256K components. Scale bar = 50 nm.

To understand how this nanoparticle interface was being formed and if we could improve its stability, we next used cryoEM for structural determination. 3D variability analysis in Cryosparc (Punjani et al. 2017) identified four different clusters of particles. Refinement of each of these particle clusters resulted in four different reconstructions, each with a final resolution of ~8 Å **(Figure 3.2B)**. Since this nanoparticle formed multiple states that each only resolved to ~8 Å,

we concluded that there was a high degree of flexibility within this nanoparticle structure. Even though we could not accurately model side chains in these densities, we were able to fit backbone structure using Isolde (lab of Randy Read n.d.). This resulted in four models that all deviated between 0.8 Å-1.6 Å **(Figure 3.2B)**. Next, we used these models to run ProteinMPNN again on their cage interfaces to see if new and improved interactions could be made. This resulted in another four designs, each only differing from the original design by 1-2 point mutations. Testing these designs in the same manner as the first round resulted in one construct with a A189L mutation that was observed to predominantly form the intended nanoparticle structure by nsEM and also did not show free component upon a second run of SEC **(Figures 3.2C and 3.2D)**.

Given the successful, stable formation of I32-18 expressed from a bicistronic gene, we next tested separate expression of each nanoparticle component in *E. coli*. Both the trimer and dimer components showed expression by SDS-PAGE upon IMAC purification. The trimer component also showed subsequent elution at the predicted volume (~17 mL) upon SEC purification **(Figure 3.2E)**, however the dimer component eluted much earlier than expected, at ~10 mL **(Figure 3.2F)**. nsEM showed that this dimer was forming both short (~25 nm) and long (~500 nm) fiber formations on its own **(Figure 3.2F)**. To discourage this fiber formation while maintaining nanoparticle assembly, dimer resurfacing mutations F287Y and I256K were introduced, which are positions located proximal but not within the nanoparticle interface. The dimer with these mutations was purified in 50 mM Tris pH 8.0, 500 mM NaCl, and 200 mM Arginine (50 mM Tris pH 8.0, 150 mM NaCl was used previously for the initial dimer purification) on SEC, which resulted in a large, broad peak around ~18 mL as expected for the soluble dimer **(Figure 3.2G)**. This material was then mixed at a 1:1 molar ratio with the purified trimer nanoparticle component, which resulted in fully assembled, homogeneous I32 nanoparticles by nsEM **(Figure 3.2H)**.

3.2.4 HA icosahedral series biophysical characterization and immunogenicity in mice

Recently, a much smaller, 1 component, *de novo* icosahedral nanoparticle called RC_I_1 was developed in the Baker Lab using a reinforcement learning algorithm (Lutz et al. 2023). We were able to genetically fuse HA to the N-terminus of this nanoparticle **(Figure 3.3A)** using a relatively long 12 residue Gly-Ser linker and demonstrate both its secretion out of HEK293F cells and formation using SDS-PAGE, SEC, and nsEM. Antibodies 5J8 and CR9114 both demonstrated binding to the MI15 strain of HA-RC_I_1, albeit with lower binding than to MI15-I53_dn5 **(Figure 3.3B)**, likely due to the very close spacing of HA on RC_I_1. We tested the immunogenicity of MI15-RC_I_1 compared to MI15-I53_dn5 in a preliminary mouse study **(Figure 3.3C)**. Mice were immunized at weeks 0 and 4 with 1.5 ug total protein. Of note, since the total protein was the same in both groups, there was 21% more HA in the MI15-RC_I_1 group. ELISA binding titers in week 6 serum were similarly high for both nanoparticles against MI15 HA ectodomain **(Figure 3.3C)**. Minimal pre-existing HA titers were present in these animals, as no MI15 titers were detected in RC_I_1 serum. By contrast to MI15 ectodomain HA, titers were ~2 log higher in the MI15-RC_I_1 group compared to the MI15-I53_dn5 group against the HA stabilized-stem MI15 (ssMI15). Binding titers against the RC_I_1 nanoparticle were similarly low between the

MI15-RC_I_1 and RC_I_1 groups, suggesting that the close packing of displayed HA did not impact scaffold immunogenicity.

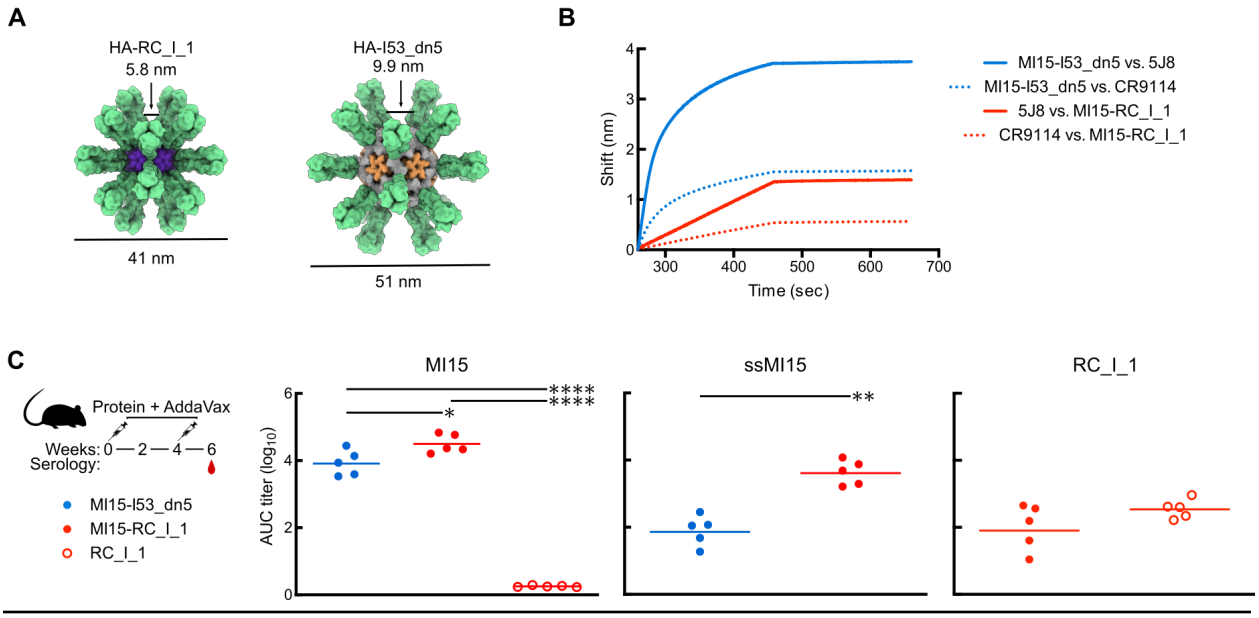

Figure 3.3 Immunogenicity study comparing HA-RC_I_1 and HA-I53_dn5
(A) Models of the HA-RC_I_1 and HA-I53_dn5.
(B) BLI of 5J8 and CR9114 against HA-RC_I_1 and HA-I53_dn5.
(C) ELISA binding titers elicited in mice immunized with HA-RC_I_1, HA-I53_dn5, or RC_I_1.
Statistical significance for MI15 was determined using one-way ANOVA with Tukey's multiple comparisons test; ∗p < 0.05; ∗∗∗∗p < 0.0001.
Statistical significance for ssMI15 was determined using two-tailed Mann-Whitney test; ∗∗p < 0.01.

In parallel to the MI15-RC_I_1 and MI15-I53_dn5 mouse study, we also incorporated these groups into a larger study using H3 (A/Hong Kong/1/2014) HA on several icosahedral nanoparticles of varying sizes to test the effects of antigen spacing while keeping valency constant, with the hypothesis that spacing out HA to promote bivalent ligation would increase anti-stem responses **(Figure 3.4A)**. HA had been previously established in our lab to secrete as a stable trimer when genetically fused to the I53-50A trimer nanoparticle component (data not shown). Since the I32-18 trimer is based on the same structure as I53-50A (PDB: 1wa3), the same genetic fusion was used to make HA fused to the I32-18 trimer. This construct was expressed in HEK293F cells and purified by SEC before subsequent nanoparticle assembly. This resulted in H3-I32 nanoparticle formation as demonstrated by nsEM **(Figure 3.4B)**. We also included H3-I53-50, which has the same spacing as H3-I53_dn5 but are completely different scaffolds. Finally, we created an extension series of H3-I53_dn5 by incorporating 3heptad and 6heptad coiled-coil GCN4-based extension domains in between the I53_dn5 nanoparticle and the H3 antigen. This spaced out HA such that the 6heptad has similar size and spacing to the H3-I32 nanoparticle. Importantly, T cell epitopes between these three I53_dn5 nanoparticles are the same, whereas T cell help from the underlying scaffold is another variable

amongst the rest of the groups. All H3 icosahedra formed monodisperse, homogeneous nanoparticles following SEC purification as seen in nsEM micrographs **(Figure 3.4B)**. We tested this nanoparticle series in an immunogenicity study in mice. In this study, a 1.5 ug total dose was used for each group, normalizing the total protein in the entire immunogen. This resulted in a varying amount of H3 amongst groups, with the H3-RC_I_1 having the biggest increase (~20-25% more) in total H3 as compared to more similar amounts in the other groups. ELISA binding titers in week 10 serum were relatively high against respective scaffolds for each group except H3-RC_I_1 and H3-I53-50 groups, which both had relatively low anti-scaffold responses **(Figure 3.4C)**. Titers against vaccine-matched H3 were comparably high amongst all groups. By contrast, H3 stabilized-stem (ssH3) titers were ~2 log higher in the H3-RC_I_1 group as compared to all other groups. Higher titers in the H3-RC_I_1 group compared to all other groups were also consistently seen against divergent group 2 vaccine-mismatched strains H7, H10, and ssH10.

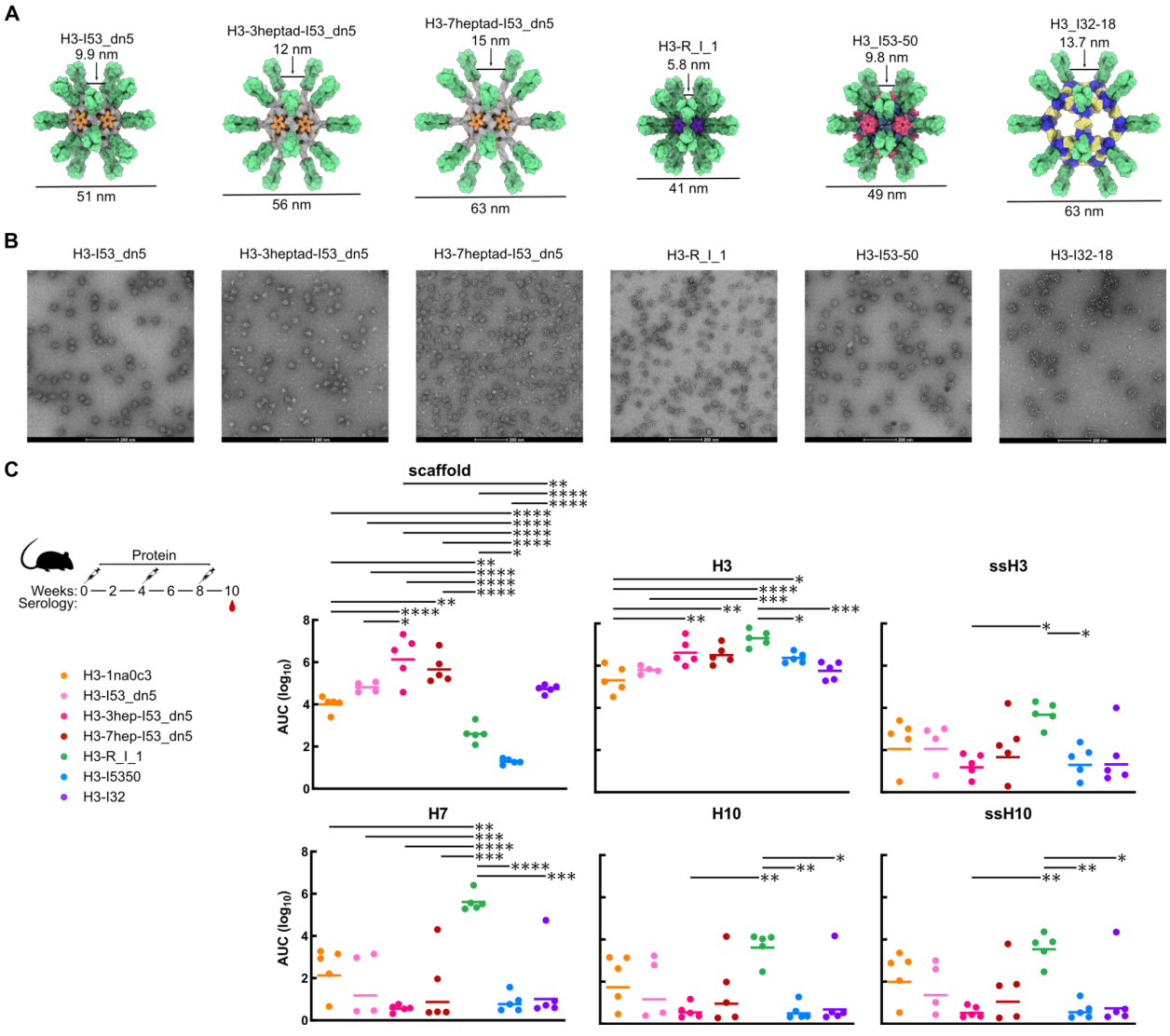

Figure 3.4 Vaccine-elicited Antibody Responses in Mice Immunized with HA Icosahedral Series
(A) Models of all nanoparticles in HA icosahedral series.
(B) nsEM micrographs of all nanoparticles in HA icosahedral series.
(C) ELISA binding titers elicited in mice immunized with HA icosahedral series.
Statistical significance was determined using one-way ANOVA with Tukey's multiple comparisons test; ∗p < 0.05; ∗∗p < 0.01; ∗∗∗p < 0.001; ∗∗∗∗p < 0.0001.

3.3 Discussion

Here we showed that the H3-RC_I_1 nanoparticle elicited dramatically higher, group 2 cross-reactive titers than all other H3 nanoparticles in this HA icosahedral study, and that this was largely due to an increase in anti-stem responses. One caveat to this study is the discrepancy in the amount of H3 between groups, with the H3-RC_I_1 group containing ~20-25% more H3 than all other groups. Thus, this study should be repeated with H3 gram-equivalence between groups to normalize the total HA content. Despite this, there are a multitude of reasons as to why the H3-RC_I_1 group elicited this increase in broad anti-stem responses. These include T cell help differences amongst the various scaffolds (Woodruff et al. 2018), potential variation in lymph node trafficking due to nanoparticle size and/or variation in glycosylation patterns (Read et al. 2022; Tokatlian et al. 2019; Aung et al. 2023; Bachmann and Jennings 2010), nanoparticle stability within the lymph node and antigen susceptibility to protease degradation (Read et al. 2022; Cirelli et al. 2019; Martin et al. 2020), and differences in BCR binding and thus B cell activation (Veneziano et al. 2020; Shaw et al. 2019). Since anti-scaffold responses were low against both H3-RC_I_1 and H3-I53-50, but anti-stem responses were not increased in the latter, competition of anti-scaffold responses does not appear to be a significant factor in these immune responses. All of these potential factors will need to be explored in order to understand their weight in shaping humoral responses and to be able to design improved nanoparticle-based vaccines.

Our *in vitro* results suggest that bivalent ligation is only happening with anti-stem and not anti-RBS antibodies against HA-I53_dn5. However, our hypothesis that increased spacing of HA on a larger nanoparticle to further optimize bivalent ligation of anti-stem B cells did not result in an increase in anti-stem antibodies. One possibility to explain this is that this HA icosahedral series did not effectively probe for bivalent ligation and another or multiple of the factors previously mentioned are spurring these differences in immunogenicity. Probing for bivalent ligation of these HA nanoparticles using anti-stem B cell activation assays or structurally using cryo-electron tomography may be more effective measures of its effect. Additionally, improvements to a series of immunogens that have only one variable influencing immunogenicity at a time while controlling for all other known variables may yield a clearer understanding of the effect that bivalent ligation has on the immune system.

References

Abbott, Robert K., Jeong Hyun Lee, Sergey Menis, Patrick Skog, Meghan Rossi, Takayuki Ota, Daniel W. Kulp, et al. 2018. “Precursor Frequency and Affinity Determine B Cell Competitive Fitness in Germinal Centers, Tested with Germline-Targeting HIV Vaccine Immunogens.” *Immunity* 48 (1): 133–46.e6.

Adolf-Bryfogle, Jared, Jason W. Labonte, John C. Kraft, Maxim Shapovalov, Sebastian Raemisch, Thomas Lütteke, Frank DiMaio, et al. 2021. “Growing Glycans in Rosetta: Accurate de Novo Glycan Modeling, Density Fitting, and Rational Sequon Design.” *bioRxiv*. https://doi.org/10.1101/2021.09.27.462000.

Altman, Meghan O., Davide Angeletti, and Jonathan W. Yewdell. 2018. “Antibody Immunodominance: The Key to Understanding Influenza Virus Antigenic Drift.” *Viral Immunology* 31 (2): 142–49.

Altman, Meghan O., Jack R. Bennink, Jonathan W. Yewdell, and Brantley R. Herrin. 2015. “Lamprey VLRB Response to Influenza Virus Supports Universal Rules of Immunogenicity and Antigenicity.” *eLife* 4 (August). https://doi.org/10.7554/eLife.07467.

Angeletti, Davide, James S. Gibbs, Matthew Angel, Ivan Kosik, Heather D. Hickman, Gregory M. Frank, Suman R. Das, et al. 2017. “Defining B Cell Immunodominance to Viruses.” *Nature Immunology* 18 (4): 456–63.

Aung, Aereas, Ang Cui, Laura Maiorino, Ava P. Amini, Justin R. Gregory, Maurice Bukenya, Yiming Zhang, et al. 2023. “Low Protease Activity in B Cell Follicles Promotes Retention of Intact Antigens after Immunization.” *Science* 379 (6630): eabn8934.

Bachmann, Martin F., and Gary T. Jennings. 2010. “Vaccine Delivery: A Matter of Size, Geometry, Kinetics and Molecular Patterns.” *Nature Reviews. Immunology* 10 (11): 787–96.

Baden, Lindsey R., Hana M. El Sahly, Brandon Essink, Karen Kotloff, Sharon Frey, Rick Novak, David Diemert, et al. 2021. “Efficacy and Safety of the mRNA-1273 SARS-CoV-2 Vaccine.” *The New England Journal of Medicine* 384 (5): 403–16.

Bajic, Goran, and Stephen C. Harrison. 2021. “Antibodies That Engage the Hemagglutinin Receptor-Binding Site of Influenza B Viruses.” *ACS Infectious Diseases* 7 (1): 1–5.

Bajic, Goran, Max J. Maron, Yu Adachi, Taishi Onodera, Kevin R. McCarthy, Charles E. McGee, Gregory D. Sempowski, et al. 2019. “Influenza Antigen Engineering Focuses Immune Responses to a Subdominant but Broadly Protective Viral Epitope.” *Cell Host & Microbe* 25 (6): 827–35.e6.

Bale, Jacob B., Shane Gonen, Yuxi Liu, William Sheffler, Daniel Ellis, Chantz Thomas, Duilio Cascio, et al. 2016. “Accurate Design of Megadalton-Scale Two-Component Icosahedral Protein Complexes.” *Science* 353 (6297): 389–94.

Bangaru, Sandhya, Shanshan Lang, Michael Schotsaert, Hillary A. Vanderven, Xueyong Zhu, Nurgun Kose, Robin Bombardi, et al. 2019. “A Site of Vulnerability on the Influenza Virus Hemagglutinin Head Domain Trimer Interface.” *Cell* 177 (5): 1136–52.e18.

Bedford, Trevor, Steven Riley, Ian G. Barr, Shobha Broor, Mandeep Chadha, Nancy J. Cox, Rodney S. Daniels, et al. 2015. “Global Circulation Patterns of Seasonal Influenza Viruses Vary with Antigenic Drift.” *Nature* 523 (7559): 217–20.

Bedford, Trevor, Marc A. Suchard, Philippe Lemey, Gytis Dudas, Victoria Gregory, Alan J. Hay, John W. McCauley, Colin A. Russell, Derek J. Smith, and Andrew Rambaut. 2014. “Integrating Influenza Antigenic Dynamics with Molecular Evolution.” *eLife* 3 (February): e01914.

Bianchi, Matteo, Hannah L. Turner, Bartek Nogal, Christopher A. Cottrell, David Oyen, Matthias Pauthner, Raiza Bastidas, et al. 2018. “Electron-Microscopy-Based Epitope Mapping Defines Specificities of Polyclonal Antibodies Elicited during HIV-1 BG505 Envelope Trimer Immunization.” *Immunity* 49 (2): 288–300.e8.

Boyoglu-Barnum, Seyhan, Daniel Ellis, Rebecca A. Gillespie, Geoffrey B. Hutchinson, Young-Jun Park, Syed M. Moin, Oliver J. Acton, et al. 2021. “Quadrivalent Influenza Nanoparticle Vaccines Induce Broad Protection.” *Nature* 592 (7855): 623–28.

Brinkkemper, Mitch, Tim S. Veth, Philip J. M. Brouwer, Hannah Turner, Meliawati Poniman, Judith A. Burger, Joey H. Bouhuijs, et al. 2022. “Co-Display of Diverse Spike Proteins on Nanoparticles Broadens Sarbecovirus Neutralizing Antibody Responses.” *iScience* 25 (12): 105649.

Carrat, F., and A. Flahault. 2007. “Influenza Vaccine: The Challenge of Antigenic Drift.” *Vaccine* 25 (39-40): 6852–62.

Cirelli, Kimberly M., Diane G. Carnathan, Bartek Nogal, Jacob T. Martin, Oscar L. Rodriguez, Amit A. Upadhyay, Chiamaka A. Enemuo, et al. 2019. “Slow Delivery Immunization Enhances HIV Neutralizing Antibody and Germinal Center Responses via Modulation of Immunodominance.” *Cell* 177 (5): 1153–71.e28.

Cohen, Alexander A., Neeltje van Doremalen, Allison J. Greaney, Hanne Andersen, Ankur Sharma, Tyler N. Starr, Jennifer R. Keeffe, et al. 2022. “Mosaic RBD Nanoparticles Protect against Challenge by Diverse Sarbecoviruses in Animal Models.” *Science* 377 (6606): eabq0839.

Cohen, Alexander A., Priyanthi N. P. Gnanapragasam, Yu E. Lee, Pauline R. Hoffman, Susan Ou, Leesa M. Kakutani, Jennifer R. Keeffe, et al. 2021. “Mosaic Nanoparticles Elicit Cross-Reactive Immune Responses to Zoonotic Coronaviruses in Mice.” *Science* 371 (6530): 735–41.

Corbett, Kizzmekia S., Darin K. Edwards, Sarah R. Leist, Olubukola M. Abiona, Seyhan Boyoglu-Barnum, Rebecca A. Gillespie, Sunny Himansu, et al. 2020. “SARS-CoV-2 mRNA Vaccine Design Enabled by Prototype Pathogen Preparedness.” *Nature* 586 (7830): 567–71.

Corbett, Kizzmekia S., Syed M. Moin, Hadi M. Yassine, Alberto Cagigi, Masaru Kanekiyo, Seyhan Boyoglu-Barnum, Sky I. Myers, et al. 2019. “Design of Nanoparticulate Group 2 Influenza Virus Hemagglutinin Stem Antigens That Activate Unmutated Ancestor B Cell Receptors of Broadly Neutralizing Antibody Lineages.” *mBio* 10 (1). https://doi.org/10.1128/mBio.02810-18.

Creanga, Adrian, Rebecca A. Gillespie, Brian E. Fisher, Sarah F. Andrews, Julia Lederhofer, Christina Yap, Liam Hatch, et al. 2021. “A Comprehensive Influenza Reporter Virus Panel for High-Throughput Deep Profiling of Neutralizing Antibodies.” *Nature Communications* 12 (1): 1722.

Dauparas, J., I. Anishchenko, N. Bennett, H. Bai, R. J. Ragotte, L. F. Milles, B. I. M. Wicky, et al. 2022. “Robust Deep Learning-Based Protein Sequence Design Using ProteinMPNN.” *Science* 378 (6615): 49–56.

Doud, Michael B., and Jesse D. Bloom. 2016. “Accurate Measurement of the Effects of All Amino-Acid Mutations on Influenza Hemagglutinin.” *Viruses* 8 (6). https://doi.org/10.3390/v8060155.

Dreyfus, Cyrille, Nick S. Laursen, Ted Kwaks, David Zuijdgeest, Reza Khayat, Damian C. Ekiert, Jeong Hyun Lee, et al. 2012. “Highly Conserved Protective Epitopes on Influenza B Viruses.” *Science* 337 (6100): 1343–48.

Duan, Hongying, Xuejun Chen, Jeffrey C. Boyington, Cheng Cheng, Yi Zhang, Alexander J. Jafari, Tyler Stephens, et al. 2018. “Glycan Masking Focuses Immune Responses to the HIV-1 CD4-Binding Site and Enhances Elicitation of VRC01-Class Precursor Antibodies.” *Immunity* 49 (2): 301–11.e5.

Eggink, Dirk, Peter H. Goff, and Peter Palese. 2014. “Guiding the Immune Response against Influenza Virus Hemagglutinin toward the Conserved Stalk Domain by Hyperglycosylation of the Globular Head Domain.” *Journal of Virology* 88 (1): 699–704.

Ekiert, Damian C., Arun K. Kashyap, John Steel, Adam Rubrum, Gira Bhabha, Reza Khayat,

Jeong Hyun Lee, et al. 2012. “Cross-Neutralization of Influenza A Viruses Mediated by a Single Antibody Loop.” *Nature* 489 (7417): 526–32.
Ellis, Daniel, Annie Dosey, Seyhan Boyoglu-Barnum, Young-Jun Park, Rebecca Gillespie, Hubza Syeda, Yaroslav Tsybovsky, et al. n.d. “Antigen-Antigen Spacing on Protein Nanoparticles Influences Antibody Responses to Vaccination.”
Ellis, Daniel, Julia Lederhofer, Oliver J. Acton, Yaroslav Tsybovsky, Sally Kephart, Christina Yap, Rebecca A. Gillespie, et al. 2022. “Structure-Based Design of Stabilized Recombinant Influenza Neuraminidase Tetramers.” *Nature Communications* 13 (1): 1825.
Flannery, Brendan, Rebecca J. Garten Kondor, Jessie R. Chung, Manjusha Gaglani, Michael Reis, Richard K. Zimmerman, Mary Patricia Nowalk, et al. 2020. “Spread of Antigenically Drifted Influenza A(H3N2) Viruses and Vaccine Effectiveness in the United States During the 2018-2019 Season.” *The Journal of Infectious Diseases* 221 (1): 8–15.
Guthmiller, Jenna J., Julianna Han, Henry A. Utset, Lei Li, Linda Yu-Ling Lan, Carole Henry, Christopher T. Stamper, et al. 2022. “Broadly Neutralizing Antibodies Target a Haemagglutinin Anchor Epitope.” *Nature* 602 (7896): 314–20.
Han, Julianna, Aaron J. Schmitz, Sara T. Richey, Ya-Nan Dai, Hannah L. Turner, Bassem M. Mohammed, Daved H. Fremont, Ali H. Ellebedy, and Andrew B. Ward. 2021. “Polyclonal Epitope Mapping Reveals Temporal Dynamics and Diversity of Human Antibody Responses to H5N1 Vaccination.” *Cell Reports* 34 (4): 108682.
Hsieh, Ching-Lin, Jory A. Goldsmith, Jeffrey M. Schaub, Andrea M. DiVenere, Hung-Che Kuo, Kamyab Javanmardi, Kevin C. Le, et al. 2020. “Structure-Based Design of Prefusion-Stabilized SARS-CoV-2 Spikes.” *Science* 369 (6510): 1501–5.
Jardine, Joseph G., Takayuki Ota, Devin Sok, Matthias Pauthner, Daniel W. Kulp, Oleksandr Kalyuzhniy, Patrick D. Skog, et al. 2015. “HIV-1 VACCINES. Priming a Broadly Neutralizing Antibody Response to HIV-1 Using a Germline-Targeting Immunogen.” *Science* 349 (6244): 156–61.
Kallewaard, Nicole L., Davide Corti, Patrick J. Collins, Ursula Neu, Josephine M. McAuliffe, Ebony Benjamin, Leslie Wachter-Rosati, et al. 2016. “Structure and Function Analysis of an Antibody Recognizing All Influenza A Subtypes.” *Cell* 166 (3): 596–608.
Kanekiyo, Masaru, M. Gordon Joyce, Rebecca A. Gillespie, John R. Gallagher, Sarah F. Andrews, Hadi M. Yassine, Adam K. Wheatley, et al. 2019. “Mosaic Nanoparticle Display of Diverse Influenza Virus Hemagglutinins Elicits Broad B Cell Responses.” *Nature Immunology* 20 (3): 362–72.
Kanekiyo, Masaru, Chih-Jen Wei, Hadi M. Yassine, Patrick M. McTamney, Jeffrey C. Boyington, James R. R. Whittle, Srinivas S. Rao, Wing-Pui Kong, Lingshu Wang, and Gary J. Nabel. 2013. “Self-Assembling Influenza Nanoparticle Vaccines Elicit Broadly Neutralizing H1N1 Antibodies.” *Nature* 499 (7456): 102–6.
Kato, Yu, Robert K. Abbott, Brian L. Freeman, Sonya Haupt, Bettina Groschel, Murillo Silva, Sergey Menis, Darrell J. Irvine, William R. Schief, and Shane Crotty. 2020. “Multifaceted Effects of Antigen Valency on B Cell Response Composition and Differentiation In Vivo.” *Immunity* 53 (3): 548–63.e8.
Kobayashi, Yuki, and Yoshiyuki Suzuki. 2012. “Evidence for N-Glycan Shielding of Antigenic Sites during Evolution of Human Influenza A Virus Hemagglutinin.” *Journal of Virology* 86 (7): 3446–51.
Koel, Björn F., David F. Burke, Theo M. Bestebroer, Stefan van der Vliet, Gerben C. M. Zondag, Gaby Vervaet, Eugene Skepner, et al. 2013. “Substitutions near the Receptor Binding Site Determine Major Antigenic Change during Influenza Virus Evolution.” *Science* 342 (6161): 976–79.
Krarup, Anders, Daphné Truan, Polina Furmanova-Hollenstein, Lies Bogaert, Pascale Bouchier, Ilona J. M. Bisschop, Myra N. Widjojoatmodjo, et al. 2015. “A Highly Stable Prefusion RSV F Vaccine Derived from Structural Analysis of the Fusion Mechanism.” *Nature*

Communications 6 (September): 8143.
Krause, Jens C., Tshidi Tsibane, Terrence M. Tumpey, Chelsey J. Huffman, Christopher F. Basler, and James E. Crowe Jr. 2011. “A Broadly Neutralizing Human Monoclonal Antibody That Recognizes a Conserved, Novel Epitope on the Globular Head of the Influenza H1N1 Virus Hemagglutinin.” *Journal of Virology* 85 (20): 10905–8.
lab of Randy Read. n.d. “ISOLDE: Bringing Structural Biology to Life.” Accessed April 3, 2023. https://isolde.cimr.cam.ac.uk/what-isolde/.
Lee, Jiwon, Daniel R. Boutz, Veronika Chromikova, M. Gordon Joyce, Christopher Vollmers, Kwanyee Leung, Andrew P. Horton, et al. 2016. “Molecular-Level Analysis of the Serum Antibody Repertoire in Young Adults before and after Seasonal Influenza Vaccination.” *Nature Medicine* 22 (12): 1456–64.
Lee, Peter S., Nobuko Ohshima, Robyn L. Stanfield, Wenli Yu, Yoshitaka Iba, Yoshinobu Okuno, Yoshikazu Kurosawa, and Ian A. Wilson. 2014. “Receptor Mimicry by Antibody F045-092 Facilitates Universal Binding to the H3 Subtype of Influenza Virus.” *Nature Communications* 5 (April): 3614.
Lee, Peter S., Reiko Yoshida, Damian C. Ekiert, Naoki Sakai, Yasuhiko Suzuki, Ayato Takada, and Ian A. Wilson. 2012. “Heterosubtypic Antibody Recognition of the Influenza Virus Hemagglutinin Receptor Binding Site Enhanced by Avidity.” *Proceedings of the National Academy of Sciences of the United States of America* 109 (42): 17040–45.
Leman, Julia Koehler, Brian D. Weitzner, Steven M. Lewis, Jared Adolf-Bryfogle, Nawsad Alam, Rebecca F. Alford, Melanie Aprahamian, et al. 2020. “Macromolecular Modeling and Design in Rosetta: Recent Methods and Frameworks.” *Nature Methods* 17 (7): 665–80.
Li, Tingting, Junyu Chen, Qingbing Zheng, Wenhui Xue, Limin Zhang, Rui Rong, Sibo Zhang, et al. 2022. “Identification of a Cross-Neutralizing Antibody That Targets the Receptor Binding Site of H1N1 and H5N1 Influenza Viruses.” *Nature Communications* 13 (1): 5182.
López-Sagaseta, Jacinto, Enrico Malito, Rino Rappuoli, and Matthew J. Bottomley. 2016. “Self-Assembling Protein Nanoparticles in the Design of Vaccines.” *Computational and Structural Biotechnology Journal* 14: 58–68.
Lutz, Isaac D., Shunzhi Wang, Christoffer Norn, Alexis Courbet, Andrew J. Borst, Yan Ting Zhao, Annie Dosey, et al. 2023. “Top-down Design of Protein Architectures with Reinforcement Learning.” *Science* 380 (6642): 266–73.
Magro, Margarita, Vicente Mas, Keith Chappell, Mónica Vázquez, Olga Cano, Daniel Luque, María C. Terrón, José A. Melero, and Concepción Palomo. 2012. “Neutralizing Antibodies against the Preactive Form of Respiratory Syncytial Virus Fusion Protein Offer Unique Possibilities for Clinical Intervention.” *Proceedings of the National Academy of Sciences* 109 (8): 3089–94.
Marcandalli, Jessica, Brooke Fiala, Sebastian Ols, Michela Perotti, Willem de van der Schueren, Joost Snijder, Edgar Hodge, et al. 2019. “Induction of Potent Neutralizing Antibody Responses by a Designed Protein Nanoparticle Vaccine for Respiratory Syncytial Virus.” *Cell* 176 (6): 1420–31.e17.
Martin, Jacob T., Christopher A. Cottrell, Aleksandar Antanasijevic, Diane G. Carnathan, Benjamin J. Cossette, Chiamaka A. Enemuo, Etse H. Gebru, et al. 2020. “Targeting HIV Env Immunogens to B Cell Follicles in Nonhuman Primates through Immune Complex or Protein Nanoparticle Formulations.” *NPJ Vaccines* 5 (1): 72.
McCarthy, Kevin R., Akiko Watanabe, Masayuki Kuraoka, Khoi T. Do, Charles E. McGee, Gregory D. Sempowski, Thomas B. Kepler, Aaron G. Schmidt, Garnett Kelsoe, and Stephen C. Harrison. 2018. “Memory B Cells That Cross-React with Group 1 and Group 2 Influenza A Viruses Are Abundant in Adult Human Repertoires.” *Immunity* 48 (1): 174–84.e9.
McLellan, Jason S., Man Chen, M. Gordon Joyce, Mallika Sastry, Guillaume B. E. Stewart-Jones, Yongping Yang, Baoshan Zhang, et al. 2013. “Structure-Based Design of a

Fusion Glycoprotein Vaccine for Respiratory Syncytial Virus." *Science* 342 (6158): 592–98.
Moin, Syed M., Jeffrey C. Boyington, Seyhan Boyoglu-Barnum, Rebecca A. Gillespie, Gabriele Cerutti, Crystal Sao-Fong Cheung, Alberto Cagigi, et al. 2022. "Co-Immunization with Hemagglutinin Stem Immunogens Elicits Cross-Group Neutralizing Antibodies and Broad Protection against Influenza A Viruses." *Immunity*, November. https://doi.org/10.1016/j.immuni.2022.10.015.
Pallesen, Jesper, Nianshuang Wang, Kizzmekia S. Corbett, Daniel Wrapp, Robert N. Kirchdoerfer, Hannah L. Turner, Christopher A. Cottrell, et al. 2017. "Immunogenicity and Structures of a Rationally Designed Prefusion MERS-CoV Spike Antigen." *Proceedings of the National Academy of Sciences of the United States of America* 114 (35): E7348–57.
Petrova, Velislava N., and Colin A. Russell. 2018. "The Evolution of Seasonal Influenza Viruses." *Nature Reviews. Microbiology* 16 (1): 47–60.
Pino, Lindsay K., Brian C. Searle, James G. Bollinger, Brook Nunn, Brendan MacLean, and Michael J. MacCoss. 2020. "The Skyline Ecosystem: Informatics for Quantitative Mass Spectrometry Proteomics." *Mass Spectrometry Reviews* 39 (3): 229–44.
Plotkin, Stanley. 2014. "History of Vaccination." *Proceedings of the National Academy of Sciences of the United States of America* 111 (34): 12283–87.
Polack, Fernando P., Stephen J. Thomas, Nicholas Kitchin, Judith Absalon, Alejandra Gurtman, Stephen Lockhart, John L. Perez, et al. 2020. "Safety and Efficacy of the BNT162b2 mRNA Covid-19 Vaccine." *The New England Journal of Medicine* 383 (27): 2603–15.
Punjani, Ali, John L. Rubinstein, David J. Fleet, and Marcus A. Brubaker. 2017. "cryoSPARC: Algorithms for Rapid Unsupervised Cryo-EM Structure Determination." *Nature Methods* 14 (3): 290–96.
"PyMOL." n.d. Accessed March 31, 2023. https://pymol.org/2.
Raymond, Donald D., Goran Bajic, Jack Ferdman, Pirada Suphaphiphat, Ethan C. Settembre, M. Anthony Moody, Aaron G. Schmidt, and Stephen C. Harrison. 2018. "Conserved Epitope on Influenza-Virus Hemagglutinin Head Defined by a Vaccine-Induced Antibody." *Proceedings of the National Academy of Sciences of the United States of America* 115 (1): 168–73.
Raymond, Donald D., Shaun M. Stewart, Jiwon Lee, Jack Ferdman, Goran Bajic, Khoi T. Do, Michael J. Ernandes, et al. 2016. "Influenza Immunization Elicits Antibodies Specific for an Egg-Adapted Vaccine Strain." *Nature Medicine* 22 (12): 1465–69.
Read, Benjamin J., Lori Won, John C. Kraft, Isaac Sappington, Aereas Aung, Shengwei Wu, Julia Bals, et al. 2022. "Mannose-Binding Lectin and Complement Mediate Follicular Localization and Enhanced Immunogenicity of Diverse Protein Nanoparticle Immunogens." *Cell Reports* 38 (2): 110217.
Rejmanek, Daniel, Parviez R. Hosseini, Jonna A. K. Mazet, Peter Daszak, and Tracey Goldstein. 2015. "Evolutionary Dynamics and Global Diversity of Influenza A Virus." *Journal of Virology* 89 (21): 10993–1.
Sabbaghi, Ailar, Seyed Mohammad Miri, Mohsen Keshavarz, Mohsen Zargar, and Amir Ghaemi. 2019. "Inactivation Methods for Whole Influenza Vaccine Production." *Reviews in Medical Virology* 29 (6): e2074.
Sahin, Ugur, Alexander Muik, Isabel Vogler, Evelyna Derhovanessian, Lena M. Kranz, Mathias Vormehr, Jasmin Quandt, et al. 2021. "BNT162b2 Vaccine Induces Neutralizing Antibodies and Poly-Specific T Cells in Humans." *Nature* 595 (7868): 572–77.
Sanders, Rogier W., Ronald Derking, Albert Cupo, Jean-Philippe Julien, Anila Yasmeen, Natalia de Val, Helen J. Kim, et al. 2013. "A next-Generation Cleaved, Soluble HIV-1 Env Trimer, BG505 SOSIP.664 gp140, Expresses Multiple Epitopes for Broadly Neutralizing but Not Non-Neutralizing Antibodies." *PLoS Pathogens* 9 (9): e1003618.
Sanders, Rogier W., Marit J. van Gils, Ronald Derking, Devin Sok, Thomas J. Ketas, Judith A. Burger, Gabriel Ozorowski, et al. 2015. "HIV-1 VACCINES. HIV-1 Neutralizing Antibodies

Induced by Native-like Envelope Trimers." *Science* 349 (6244): aac4223.
Sanders, Rogier W., and John P. Moore. 2021. "Virus Vaccines: Proteins Prefer Prolines." *Cell Host & Microbe* 29 (3): 327–33.
Sanders, Rogier W., Mika Vesanen, Norbert Schuelke, Aditi Master, Linnea Schiffner, Roopa Kalyanaraman, Maciej Paluch, et al. 2002. "Stabilization of the Soluble, Cleaved, Trimeric Form of the Envelope Glycoprotein Complex of Human Immunodeficiency Virus Type 1." *Journal of Virology* 76 (17): 8875–89.
Shaw, Alan, Ian T. Hoffecker, Ioanna Smyrlaki, Joao Rosa, Algirdas Grevys, Diane Bratlie, Inger Sandlie, Terje Einar Michaelsen, Jan Terje Andersen, and Björn Högberg. 2019. "Binding to Nanopatterned Antigens Is Dominated by the Spatial Tolerance of Antibodies." *Nature Nanotechnology* 14 (2): 184–90.
Sheffler, William, Erin C. Yang, Quinton Dowling, Yang Hsia, Chelsea N. Fries, Jenna Stanislaw, Mark Langowski, et al. 2022. "Fast and Versatile Sequence-Independent Protein Docking for Nanomaterials Design Using RPXDock." *bioRxiv*. https://doi.org/10.1101/2022.10.25.513641.
Sliepen, Kwinten, Laura Radić, Joan Capella-Pujol, Yasunori Watanabe, Ian Zon, Ana Chumbe, Wen-Hsin Lee, et al. 2022. "Induction of Cross-Neutralizing Antibodies by a Permuted Hepatitis C Virus Glycoprotein Nanoparticle Vaccine Candidate." *Nature Communications* 13 (1): 7271.
Spits, Hergen, and Tim Beaumont. 2013. RSV-specific binding molecules and means for producing them. USPTO 8562996. *US Patent*, filed May 30, 2008, and issued October 22, 2013. https://patentimages.storage.googleapis.com/48/33/71/cf99561c2bd5c9/US8562996.pdf.
Stavenhagen, Kathrin, Hannes Hinneburg, Morten Thaysen-Andersen, Laura Hartmann, Daniel Varón Silva, Jens Fuchser, Stephanie Kaspar, Erdmann Rapp, Peter H. Seeberger, and Daniel Kolarich. 2013. "Quantitative Mapping of Glycoprotein Micro-Heterogeneity and Macro-Heterogeneity: An Evaluation of Mass Spectrometry Signal Strengths Using Synthetic Peptides and Glycopeptides." *Journal of Mass Spectrometry: JMS* 48 (6): 627–39.
Struwe, Weston B., Alexandra Stuckmann, Anna-Janina Behrens, Kevin Pagel, and Max Crispin. 2017. "Global N-Glycan Site Occupancy of HIV-1 gp120 by Metabolic Engineering and High-Resolution Intact Mass Spectrometry." *ACS Chemical Biology* 12 (2): 357–61.
Thornlow, Dana N., Andrew N. Macintyre, Thomas H. Oguin, Amelia B. Karlsson, Erica L. Stover, Heather E. Lynch, Gregory D. Sempowski, and Aaron G. Schmidt. 2021. "Altering the Immunogenicity of Hemagglutinin Immunogens by Hyperglycosylation and Disulfide Stabilization." *Frontiers in Immunology* 12 (October): 737973.
Tokatlian, Talar, Benjamin J. Read, Christopher A. Jones, Daniel W. Kulp, Sergey Menis, Jason Y. H. Chang, Jon M. Steichen, et al. 2019. "Innate Immune Recognition of Glycans Targets HIV Nanoparticle Immunogens to Germinal Centers." *Science* 363 (6427): 649–54.
Ueda, George, Aleksandar Antanasijevic, Jorge A. Fallas, William Sheffler, Jeffrey Copps, Daniel Ellis, Geoffrey B. Hutchinson, et al. 2020. "Tailored Design of Protein Nanoparticle Scaffolds for Multivalent Presentation of Viral Glycoprotein Antigens." *eLife* 9 (August). https://doi.org/10.7554/eLife.57659.
Veneziano, Rémi, Tyson J. Moyer, Matthew B. Stone, Eike-Christian Wamhoff, Benjamin J. Read, Sayak Mukherjee, Tyson R. Shepherd, et al. 2020. "Role of Nanoscale Antigen Organization on B-Cell Activation Probed Using DNA Origami." *Nature Nanotechnology* 15 (8): 716–23.
Verkerke, Hans P., James A. Williams, Miklos Guttman, Cassandra A. Simonich, Yu Liang, Modestas Filipavicius, Shiu-Lok Hu, Julie Overbaugh, and Kelly K. Lee. 2016. "Epitope-Independent Purification of Native-Like Envelope Trimers from Diverse HIV-1 Isolates." *Journal of Virology* 90 (20): 9471–82.

Walls, Alexandra C., Brooke Fiala, Alexandra Schäfer, Samuel Wrenn, Minh N. Pham, Michael Murphy, Longping V. Tse, et al. 2020. “Elicitation of Potent Neutralizing Antibody Responses by Designed Protein Nanoparticle Vaccines for SARS-CoV-2.” *Cell* 183 (5): 1367–82.e17.

Walls, Alexandra C., Marcos C. Miranda, Alexandra Schäfer, Minh N. Pham, Allison Greaney, Prabhu S. Arunachalam, Mary-Jane Navarro, et al. 2021. “Elicitation of Broadly Protective Sarbecovirus Immunity by Receptor-Binding Domain Nanoparticle Vaccines.” *Cell* 184 (21): 5432–47.e16.

Watanabe, Akiko, Kevin R. McCarthy, Masayuki Kuraoka, Aaron G. Schmidt, Yu Adachi, Taishi Onodera, Keisuke Tonouchi, et al. 2019. “Antibodies to a Conserved Influenza Head Interface Epitope Protect by an IgG Subtype-Dependent Mechanism.” *Cell* 177 (5): 1124–35.e16.

Watson, Michael J., Rick Harkewicz, Edgar A. Hodge, Clint Vorauer, Jonathan Palmer, Kelly K. Lee, and Miklos Guttman. 2021. “Simple Platform for Automating Decoupled LC-MS Analysis of Hydrogen/Deuterium Exchange Samples.” *Journal of the American Society for Mass Spectrometry* 32 (2): 597–600.

Wei, Chih-Jen, Jeffrey C. Boyington, Kaifan Dai, Katherine V. Houser, Melissa B. Pearce, Wing-Pui Kong, Zhi-Yong Yang, Terrence M. Tumpey, and Gary J. Nabel. 2010. “Cross-Neutralization of 1918 and 2009 Influenza Viruses: Role of Glycans in Viral Evolution and Vaccine Design.” *Science Translational Medicine* 2 (24): 24ra21.

Weidenbacher, Payton A., and Peter S. Kim. 2019. “Protect, Modify, Deprotect (PMD): A Strategy for Creating Vaccines to Elicit Antibodies Targeting a Specific Epitope.” *Proceedings of the National Academy of Sciences* 116 (20): 9947–52.

Whittle, James R. R., Adam K. Wheatley, Lan Wu, Daniel Lingwood, Masaru Kanekiyo, Steven S. Ma, Sandeep R. Narpala, et al. 2014. “Flow Cytometry Reveals That H5N1 Vaccination Elicits Cross-Reactive Stem-Directed Antibodies from Multiple Ig Heavy-Chain Lineages.” *Journal of Virology* 88 (8): 4047–57.

Whittle, James R. R., Ruijun Zhang, Surender Khurana, Lisa R. King, Jody Manischewitz, Hana Golding, Philip R. Dormitzer, et al. 2011. “Broadly Neutralizing Human Antibody That Recognizes the Receptor-Binding Pocket of Influenza Virus Hemagglutinin.” *Proceedings of the National Academy of Sciences of the United States of America* 108 (34): 14216–21.

Woodruff, Matthew Charles, Eui Ho Kim, Wei Luo, and Bali Pulendran. 2018. “B Cell Competition for Restricted T Cell Help Suppresses Rare-Epitope Responses.” *Cell Reports* 25 (2): 321–27.e3.

Wrapp, Daniel, Nianshuang Wang, Kizzmekia S. Corbett, Jory A. Goldsmith, Ching-Lin Hsieh, Olubukola Abiona, Barney S. Graham, and Jason S. McLellan. 2020. “Cryo-EM Structure of the 2019-nCoV Spike in the Prefusion Conformation.” *Science* 367 (6483): 1260–63.

Wu, Nicholas C., and Ian A. Wilson. 2017. “A Perspective on the Structural and Functional Constraints for Immune Evasion: Insights from Influenza Virus.” *Journal of Molecular Biology* 429 (17): 2694–2709.

Wu, Nicholas C., Jia Xie, Tianqing Zheng, Corwin M. Nycholat, Geramie Grande, James C. Paulson, Richard A. Lerner, and Ian A. Wilson. 2017. “Diversity of Functionally Permissive Sequences in the Receptor-Binding Site of Influenza Hemagglutinin.” *Cell Host & Microbe* 21 (6): 742–53.e8.

Yassine, Hadi M., Jeffrey C. Boyington, Patrick M. McTamney, Chih-Jen Wei, Masaru Kanekiyo, Wing-Pui Kong, John R. Gallagher, et al. 2015. “Hemagglutinin-Stem Nanoparticles Generate Heterosubtypic Influenza Protection.” *Nature Medicine* 21 (9): 1065–70.

Zost, Seth J., Juhye Lee, Megan E. Gumina, Kaela Parkhouse, Carole Henry, Nicholas C. Wu, Chang-Chun D. Lee, et al. 2019. “Identification of Antibodies Targeting the H3N2 Hemagglutinin Receptor Binding Site Following Vaccination of Humans.” *Cell Reports* 29 (13): 4460–70.e8.